An Over-Height Collision Protection System of Sandwich Polymer Composites Integrated with Remote Monitoring for Concrete Bridge Girders

Pizhong Qiao, Ph.D., P.E., F.ASCE
The University of Akron

Mijia Yang, Ph.D., P.E.
The University of Akron

Ayman Mosallam, Ph.D., P.E.
University of California at Irvine

Gangbing Song, Ph.D.
University of Houston

for the
Ohio Department of Transportation
Office of Research and Development

and the
Federal Highway Administration

State Job Number 134142

June 30, 2008

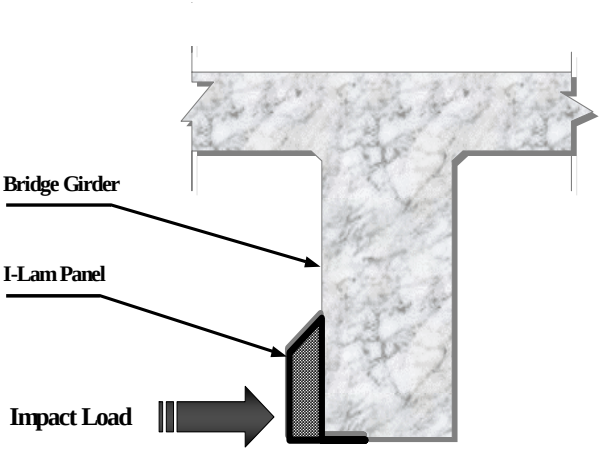

RESEARCH & DEVELOPMENT

1. Report No.	2. Government Accession No.	3. Recipient's Catalog No.
FHWA/OH-2008/6		

4. Title and subtitle	5. Report Date
An Over-Height Collision Protection System of Sandwich Polymer Composites Integrated with Remote Monitoring for Concrete Bridge Girders	**June 2008**
	6. Performing Organization Code
7. Author(s)	8. Performing Organization Report No.
Pizhong Qiao, Mijia Yang, Ayman Mosallam, and Gangbing Song	10. Work Unit No. (TRAIS)
9. Performing Organization Name and Address **The University of Akron** **Department of Civil Engineering** **Akron, OH 44325**	11. Contract or Grant No. **134142**
	13. Type of Report and Period Covered
12. Sponsoring Agency Name and Address **Ohio Department of Transportation** **1980 West Broad Street** **Columbus, OH 43223**	14. Sponsoring Agency Code

15. Supplementary Notes

16. Abstract

One of the common damages in existing highway bridges is the damage at the bottom corners or edges of the reinforced concrete beams or box girders induced by an impact of trucks exceeding the allowable height clearance of the bridges. In this study, a collision protection and scarifying system is developed, and it utilizes advanced materials/structures to protect highway bridge girders. The proposed collision protection and scarifying system is in a new "I-Lam" (Impact Laminate) configuration and bolted and/or bonded to the bottom portions or edges of concrete girders. The I-Lam panels are made of a composite sandwich construction with multi-layer aluminum honeycomb core and top and bottom thin face sheets, and they are developed/designed specifically for impact damage protection of bridge girders (e.g., concrete girders). Design criteria and guideline for I-Lam are developed, and the analysis, optimal design, and quality control tests of the collision protection system are conducted. Smart piezoelectric sensors are integrated with the I-Lam panels for monitoring the performance of the collision protection system. The collision protection system is implemented in an identified bridge. The developed smart bi-layer honeycomb I-Lam sandwich is capable of reducing the transferred contact force dramatically, absorbing/mitigating impact energy, protecting the underneath concrete structures by system scarifying and core crushing, and monitoring the impact incident with smart piezoelectric sensors, and it is applicable to protecting other structures (e.g., steel girders, columns) from accidental vehicle impact in the highways.

17. Key Words	18. Distribution Statement
Over-height truck impact; Collision protection; High energy absorbing materials; Aluminum honeycomb Cores; Sandwich panels; Bridge girders; Smart Piezoelectric Sensors.	**No restrictions. This document is available to the public through the National Technical Information Service, Springfield, Virginia 22161**

19. Security Classif. (of this report)	20. Security Classif. (of this page)	21. No. of Pages	22. Price
Unclassified	**Unclassified**	**128**	

Form DOT F 1700.7 (8-72) **Reproduction of completed pages authorized**

An Over-Height Collision Protection System of Sandwich Polymer Composites Integrated with Remote Monitoring for Concrete Bridge Girders

A 2002 Innovative Bridge Research and Construction (IBRC) Project

Revised Draft Final Report to Sponsor:
Federal Highway Administration and The Ohio Department of Transportation
State Job No. 134142

By

Pizhong Qiao*, Ph.D., P.E., F.ASCE
The University of Akron

Mijia Yang, Ph.D., P.E.
The University of Akron

Ayman Mosallam, Ph.D., P.E.
University of California, Irvine

Gangbing Song, Ph.D.
University of Houston

June 30, 2008

Department of Civil Engineering
The University of Akron
Akron, OH 44325-3905

*Contact Information for Principal Investigator:
Department of Civil and Environmental Engineering
Washington State University
Sloan 101, Spokane Street
Pullman, WA 99164-2910
Phone: 509-335-5183; Fax: 509-335-7632; Email: Qiao@wsu.edu

Prepared in cooperation with the Ohio Department of Transportation and the U.S. Department of Transportation, Federal Highway Administration

Table of Contents

List of Figures

Appendix A

Appendix B

Appendix C

Appendix D

List of Tables

1. INTRODUCTION

With about one-third of the nation's 600,000 highway bridges in need of repair or replacement, applications of innovative bridge concepts and construction methods are important to maintain the traffic concerns. Increased traffic volumes in recent years have placed enormous and ever increasing burdens on the roadway infrastructure of the country. The demands placed on the transportation network because of the high traffic volumes have necessitated the need to further improve the existing facilities and to develop new construction, replacement, rehabilitation, or repair techniques.

One of the common damages in existing highway bridges is the damage at the bottom corners or edges of the reinforced concrete beams or box girders induced by an impact of trucks exceeding the allowable height clearance of the bridges. Due to collision impact of the trucks, the bottom or outer layers of concrete girders are usually peeled off (see Figure 1) so that the steel reinforcements are exposed to the surrounding environment and subjected to corrosion, leading to the reduced load carrying capacity. An over-height collision protection or scarifying system can be used to protect the concrete girders from such impact damage, thus ensuring the integrity of the bridge structures. A collision protection and scarifying system shown in Figure 2 is developed in this study, and it utilizes advanced materials/structures to protect highway bridge girders. The proposed collision protection and scarifying system is in a new "I-Lam" (**I**mpact **Lam**inate) panel configuration and bolted and/or bonded to the bottom portions or edges of concrete girders. The proposed I-Lam panels are made of a composite sandwich construction with multi-layer aluminum honeycomb core and top and bottom thin face sheets, and they are developed/designed specifically for impact damage protection of bridge girders (e.g., concrete girders).

Figure 1 Impact damages in the concrete bridge girders by over-height trucks

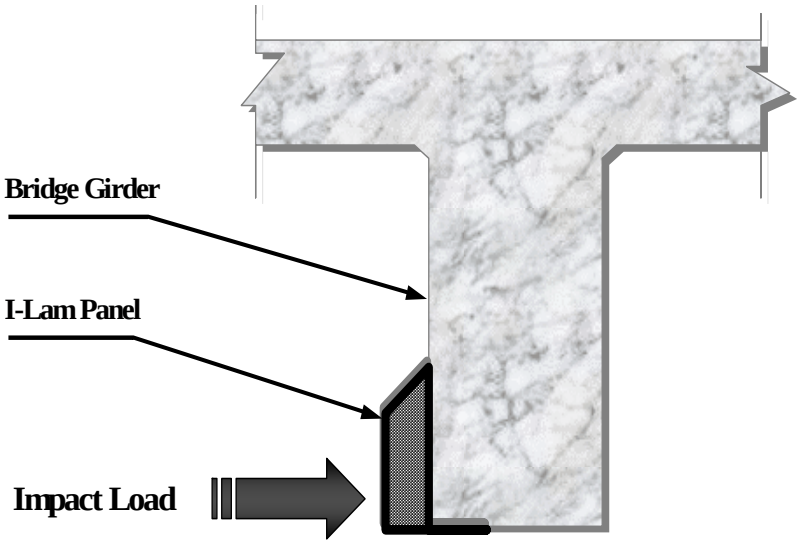

Figure 2 Over-height collision protection (scarifying) system for concrete girders

2. OBJECTIVES OF THE STUDY

Due to the relatively new design of I-Lam systems bonded to concrete, there are not many studies available to design and analyze the energy absorption behavior of such a protection system under the impact of over-height trucks. A need exists to develop practical solutions and design guidelines for such a unique collision protection system using the I-Lam panels.

This study aims to develop a new collision protection/scarifying I-Lam system for concrete bridge girders using composite sandwich with crushable core, to integrate the system with smart sensors and actuators for remote sensing, triggering and monitoring, and to demonstrate the benefits of using the scarifying elements for protecting the bridge girders from the expected localized damages. Further, this technology can also be implemented to other bridge and highway structures (e.g., columns, concrete barriers, guardrails, and sign structures) for mitigation and protection of any possible impact loads.

The major objectives of the study include: (1) To develop general design for the collision protection system based on the specified site conditions and construction requirements, (2) To conduct the analysis, optimal design, and quality control tests of the collision protection system and to develop design criteria and guideline for I-Lam, (3) To implement the developed collision protection system in identified damaged bridges or new constructed bridges, and to re-deploy the system if damage occurs over the duration of the project, and (4) To monitor the short- and long-term performance of the collision protection system using smart sensors and actuators and remote sensing technology.

The fourth objective is not fully carried out, due to the following reasons: (1) The original attachment design of I-Lam panel to the bridge using high performance adhesive is modified, and a mechanical attachment mechanism is considered to more conveniently install the I-Lam to the bridge. Thus, there is really no need to monitor the short- and long-term performance of the collision protection system in term of its bond line and longevity. (2) Since the I-Lam protection design is considered as a replaceable and scarifying system and

any damage after impact event can be obviously observed, a visual inspection is considered to evaluate the performance of the collision protection system. And (3) An effort was made by the research team and ODOT to consider installing an on-site impact monitoring and remote sensing system to evaluate the impact event and performance of the system. However, due to the difficulty of identifying a suitable bridge for implementing the I-Lam and change of the originally-identified bridge site, the plan does not eventually go through. A smart triggering and monitoring system for the collision protection system using piezoelectric sensors and actuators is instead developed and tested in the lab, and it is ready for field implementation.

3. RESEARCH BACKGROUND

The collision impact of the truck to the highway structures usually belongs to the range of low to medium velocity impact since the regular velocity of a running truck is less than 30 m/s (100 miles/hour). Through shear-off of the overheight material and crushing of the aluminum honeycomb core of the sandwich, the transfer force into the concrete girder may be considerably reduced, thus potentially protecting the underneath concrete girders from damage.

There have been very limited studies on the protection of concrete bridge girders damaged by vehicular impact. The lateral impact over prestressed concrete girders in bridges was studied by Abendroth and Fanous (2003). In their study, responses of the bridge girders under two chosen impact pulses were simulated using ANSYS, from which the deflection histories of the bridge girders were plotted. However, in a real impact/crash scenario, the impact force in their study was undetermined, and the impact damage was not included in the impact process. On the other hand, considerable research has been conducted on impact over laminate composites as well as sandwiches in aerospace engineering. The research about sandwich impact responses was first initiated by Goldsmith (1992), and a series of impact experiments were conducted on aluminum honeycomb sandwiches. Later, Lee et al. (1993) investigated the dynamic response of composite sandwich plates impacted by a rigid ball, in which a linearized compressibility of core was simulated. Tsai et al. (1998) conducted the forward and inverse analysis of impact on sandwich panels, in which an anti-plane sandwich theory was used. Caprino and Teti (1994) investigated impact and post-impact behaviors of foam core sandwich structures. Turk and Hoo Fatt (1999) developed a theoretical model using energy method to analyze the impact damage of sandwich plates, and the indentation and transient responses of sandwich plates using the assumed deflection functions were studied. Olsson (2002) derived a semi-empirical equation for impact response and damage of sandwich structures. In most of the theoretical models in the impact analysis of sandwiches, the core compressibility was not captured accurately, and the permanent deformations were usually not included. However, the inclusion of core compression and permanent deformations may be important for modeling the energy absorption and impact behavior of sandwich structures with relatively low transverse stiffness of core materials.

The impact damage and impact resistance of laminates and sandwich structures have also been extensively investigated. Dobyns and Porter (1981) first proposed the prediction of the overall damage size of a sandwich plate subjected to a low-velocity impact. Matemilola and Strong (1995) later conducted an analytical study dealing with impact-induced delamination of carbon fiber reinforced polymer (CFRP) composites. Davies et al. (1995) also developed a simple mode-II fracture analysis for single circular delamination by treating glass fiber

reinforced polymer (GFRP) composite as an isotropic material and showed that a threshold force P_c could be used to find the initiation of delamination. Reid and Zhou (2000) performed several experiments on the initiation of delamination and damage size from the impact process. Slenk et al. (2003) recently conducted an experimental investigation on assessment of residual tensile strength of graphite epoxy woven laminates after impact. Their study demonstrated that the impact damage caused a significant reduction in strength of woven cross-ply laminates; while the damage of the angle-ply ($\pm 45^o$) was less severe as compared to the $0^o/90^o$ laminates. Shipsha et al. (2003) studied the failure mechanism and modeling of impact damage in sandwich beams. Lim et al. (2004) studied failure modes of foam core sandwich beams under static and impact loads. In their study, different failure modes of sandwiches with various core density and face sheet combinations under different impact velocity were characterized.

For the present project, one of the major applications of I-Lam sandwich structures in overheight collision protection is for impact mitigation and energy absorption. In this type of application, the core materials in the I-Lam are severely crushed to thus absorb more energy. Thus, the crushing is an important failure mode, in particular for the core made of honeycomb configuration. In this project, we develop, analyze, design, test, and implement the I-Lam sandwich structures for protecting the concrete bridge girders from overheight truck impact.

4. ENGINEERING DESIGN AND ANALYSIS

Based on the fact that the use of the I-Lam panels in structural rehabilitation and protection is new, an engineering analysis to design the required I-Lam sandwich construction and geometry is first performed, with technical input from the material suppliers.

In particular, the protection system made of composite sandwich panel with aluminum honeycomb core is designed, analyzed, and further optimized, based on the potential truck impact loading range. From the selected materials for face sheet and honeycomb core materials, the construction and geometry of the sandwich panels are designed, and the contact force, deflection and absorbed energy are subsequently computed. Then, the sandwich protection system is analyzed using the finite element software (i.e., ABAQUS and LS-DYNA) for both static and dynamic loadings. Once the system is designed and analyzed, a parametric study is performed regarding the key (critical) performance factors (e.g., failure modes and impact energy absorption), and an optimal design is provided from the parametric study. The preliminary design, analysis, and optimal design provide technical input for implementing a properly designed over-height impact collision protection system in the field, from which design criteria and recommendations are correspondingly established.

4.1 Simplified Engineering Design Analysis

The I-Lam system is designed to work as a barrier system to protect the underneath concrete girders. In this arrangement, the top face sheet of the I-Lam sandwich system is in contact with the overheight materials; while the bottom face sheet of the I-Lam system is fully anchored/bonded to concrete substrate. Thus, the I-Lam collision protection system is in a fully-backed configuration (in which the bottom of I-Lam sandwich is fully restrained) under overheight material impact. When the running truck hits the I-Lam system, the overheight portion of the material is sheared-off or crushed, and the hardening effect due to

the shear-off of the overheight material should be included in the preliminary analysis and design of I-Lam system. To simulate the I-Lam collision protection system and truck over-height shear-off mechanism, three simplified design analysis models with different loading conditions are considered, and they provide explicit formulas to predict the contact force and duration during the collision events. First, a discrete model of I-Lam sandwich system (Model I) is established, followed by the inclusion of the shear-off effect. The cases of I-Lam sandwich system under concentrated (Model II) and distributed (Model III) loading conditions are next studied. The aim of the analytical study is to develop relatively simple and approximate equations for impact responses, which are used later in design and energy absorption optimization of the I-Lam system.

4.1.1 Discrete model of I-Lam sandwich system under impact (Model I)

First, a general case of I-Lam sandwich panel impacted by a subject (e.g., a moving truck) is considered. The entire system is modeled as a two-degree-of-freedom discrete spring model (Model I) (Figure 3), and the bottom face sheet of the sandwich is assumed perfectly bonded to a rigid substrate. If a damaged substrate is considered, repairing of the substrate should be first conducted to ensure the perfect bond between the protecting sandwich and protected substrate material.

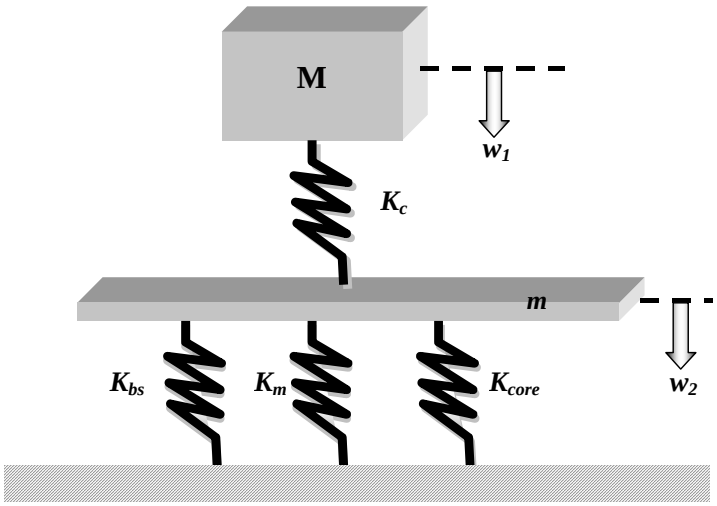

Figure 3 Discrete model of I-Lam sandwich beam under impact

The governing equations of the discrete model are given as

$$\begin{gathered} M\ddot{w}_1 - P_c = 0 \\ m\ddot{w}_2 + (K_{bs} + K_{core})w_2 + K_m {w_2}^3 - P_c = 0 \\ P_c = K_c (w_1 - w_2)^{3/2} \end{gathered} \tag{1}$$

and with the initial conditions at $t = 0$:

$$\dot{w}_1(0) = V_0, w_1(0) = w_2(0) = 0, \dot{w}_2(0) = 0 \tag{2}$$

where M is the mass of the subject (e.g., the mass of over-height portion of a truck); m is

the mass of the top face sheet in I-Lam sandwich beam; P_c is the contact force between the projector and the I-Lam sandwich system; w_1 and w_2 are the displacements of the over-height material of the truck and the top face sheet of the sandwich, respectively; K_c is the contact stiffness; K_{bs} is the combined bending and shear stiffness of the top face sheet of the sandwich; K_{core} is the through-the-thickness stiffness of the core; K_m is the stiffness contributed by the membrane effect of the face sheet; and V_0 is the initial velocity of the subject at the moment of impact. Since the mass of top face sheet (m) is relatively small, its inertial effect is neglected in analysis (Qiao et al. 2004).

Let $w = w_1$, the governing equations in Eq. (1) reduce to

$$M\ddot{w} + \frac{(K_{bs} + K_{core})K_c}{K_{bs} + K_{core} + K_c} w = 0 \tag{3}$$

The deformation shape function is expressed as

$$w(t) = A\sin\omega t + B\cos\omega t \tag{4}$$

where $\omega^2 = \frac{K_{eq}}{M}, K_{eq} = \frac{(K_{bs} + K_{core})K_c}{(K_{bs} + K_{core} + K_c)}$. Considering the initial conditions described in Eq. (2), the constants in Eq. (4) are obtained as $A = \frac{V_0}{\omega}$ and $B = 0$. Now, the contact force in Eq. (1) can be obtained using the following expression,

$$P_c = V_0\sqrt{K_{eq}M}\,\sin\sqrt{\frac{K_{eq}}{M}}t \tag{5}$$

The contact duration is defined as,

$$T_c = \frac{\pi}{\omega} = \pi\sqrt{\frac{M}{K_{eq}}} \tag{6}$$

when $t < T_c$ indicates that the projectile and I-Lam sandwich are in contact; otherwise, the two objects are separated.

Since only the over-height portion of the truck hits the I-Lam system, it is sheared off as the truck is traveling through (refer to Figure 4). Therefore, the initial impact force acting on the I-Lam beam should be considered as

$$P_c = M_s\ddot{w} + \tau_w A_s \tag{7}$$

where A_s is the area of the shear-off portion of the truck; M_s is the mass of the shear-off portion; and τ_w is the shear strength of the over-height materials (e.g., over-packed snow or other materials). In this part of study, the over-height materials are considered as

over-packed snow, accumulated ice, excessively-piled trash with plastic cans, or other over-packed materials (such as wood materials) on the top of truck, thus making the truck higher than the original height (so called the "over-height"). Then, the equilibrium equation considering the shear-off mechanism becomes

$$M_s \ddot{w} + \tau_w A_s + K_{eq} w = 0 \tag{8}$$

The general solution of Eq. (8) is

$$w(t) = A\sin\omega t + B\cos\omega t + D \tag{9}$$

where $\omega^2 = \frac{K_{eq}}{M_s}$. By considering the initial conditions given in Eq. (2), $A = \frac{V_0}{\omega}; B = -\frac{\tau_w A_s}{K_{eq}}; D = \frac{\tau_w A_s}{K_{eq}}$ are obtained. Similarly, the contact force considering the shear-off effect is expressed as,

$$P_c = K_{eq}\left(\frac{V_0}{\sqrt{\frac{K_{eq}}{M_s}}}\sin\sqrt{\frac{K_{eq}}{M_s}}t - \frac{\tau_w A_s}{K_{eq}}\cos\sqrt{\frac{K_{eq}}{M_s}}t + \frac{\tau_w A_s}{K_{eq}}\right) \tag{10}$$

Again, the contact duration is defined as

$$T_c = \sqrt{\frac{M}{K_{eq}}}Cos\left(\frac{1-c^2}{1+c^2}\right) \tag{11}$$

In which, due to the shear force generated through shearing the projectile (i.e., the shear-off portion of the overheight material), the contact force is increased through the new items derived in comparison to the standard mass spring solution without shear-off effect. The contact duration is shortened due to the shear-off effect and $c = \frac{V_0\sqrt{K_{eq}M_s}}{\tau_w A_s}$.

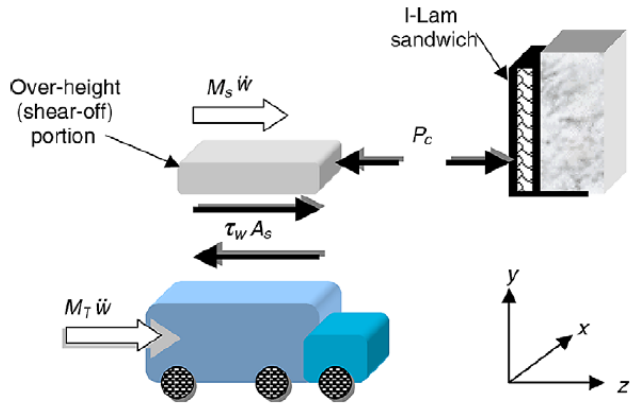

Figure 4 Free-body diagram of shear-off mechanism of truck impact

4.1.2 I-Lam sandwich beams impacted by a concentrated load (Model II)

Considering a case when the fully-backed sandwich beam (i.e., the I-Lam), of which the bottom face sheet is rigidly bonded to a rigid substrate, is being hit by a concentrated load (P) at the mid-span and the low velocity of the impact (Figure 5), the analysis is considered as a sandwich beam under a static concentrated load (Model II), from which the contact force, deflection and duration are obtained. Following the procedures given in Qiao et al. (2004), the contact force without and with the inclusion of shear-off effect of overheight material is obtained, respectively, as

$$P = k_1 w(0,t) = 8\left(\frac{E_c b}{h_c}\right)^{3/4}(EI)^{1/4}\frac{V_0}{\sqrt{\frac{k_1}{M}}}\sin\sqrt{\frac{k_1}{M}}t \tag{12}$$

$$P = k_1 w(0,t) = 8\left(\frac{E_c b}{h_c}\right)^{3/4}(EI)^{1/4}\left[\frac{V_0}{\sqrt{\frac{k_1}{M}}}\sin\sqrt{\frac{k_1}{M}}t - \frac{\tau A_s}{k_1}\cos\sqrt{\frac{k_1}{M}}t + \frac{\tau A_s}{k_1}\right] \tag{13}$$

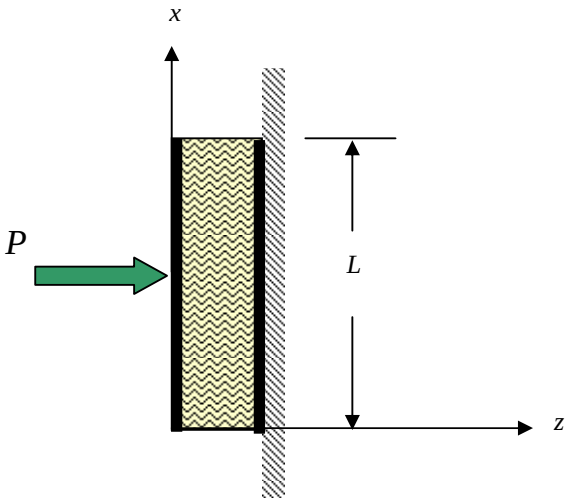

Figure 5 Impact analysis of I-Lam sandwich beam under concentrated loading

4.1.3 I-Lam sandwich beam impacted by a distributed load (Model III)

In a similar fashion to the I-Lam sandwich impacted by a concentrated load (Model II) in Section 4.1.2, the I-Lam sandwich beam under uniform impact loading condition (Model III) (Figure 6) is analyzed. Considering the shear-off effect of the over-height portion, the deflection in the I-Lam sandwich beam is obtained (Qiao et al. 2004) as

$$w(y,t) = \frac{V_0}{\sqrt{\frac{k}{M}}} Sin\left(\sqrt{\frac{k}{M}}t\right) - \frac{\tau_w A}{k} Cos\left(\sqrt{\frac{k}{M}}t\right) + \frac{\tau_w A}{k} \tag{14}$$

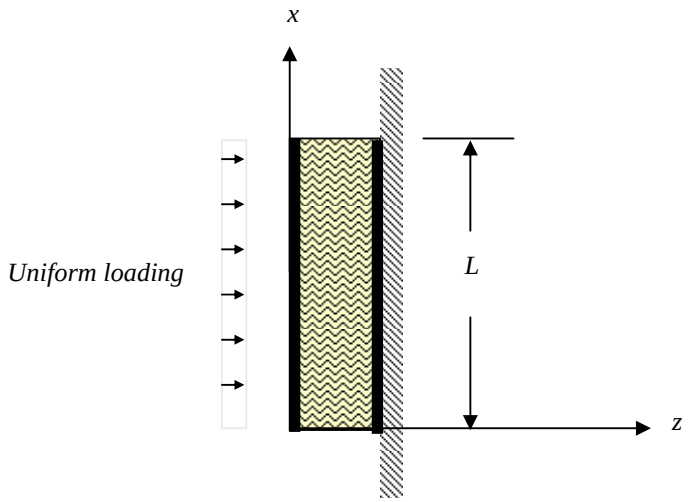

Figure 6 Impact analysis of I-Lam sandwich beam under uniform distributed loading

4.1.4 Analytical results and discussions

Based on the above three simplified analytical models developed, a case study is performed. In this example, the impact of an I-Lam sandwich system hit by an over-height portion of a truck is simulated. The over-height material is assumed to be a moderately hard material (e.g., wood) with density (ρ) of 81.16 pcf ($1.3\times10^3\, kg/m^3$). The shear-off area (A_s) was assumed to be 10.75 sq. ft. (1.0 m^2), and the mass of shear-off portion (M_s) taken as 0.08 lbs (0.0361 kg). The dimensions of I-Lam are length L = 3.28 ft. (1.0 m), height b = 0.33 ft. (0.1 m), and thickness $2h + 2t$ = 0.66 ft. (0.2 m) (where h = 0.30 ft. (0.09 m) and t = 0.033 ft. (0.01 m) are the half thickness of core and face sheet thickness, respectively). Other related parameters needed in the modeling are given in Table 1. Based on the specified parameters and using the proposed theoretical procedures, the contact force history for the above three models is presented in Figure 7. The maximum displacement history for the three analytical models is plotted in Figure 8. From these figures, one can observe that for a rigidly supported I-Lam sandwich beam condition, the impact response of the discrete model (Model I) are lower than the corresponding values of the models with concentrated (Model II) and distributed (Model III) impact forces. Also, it is interesting to observe that both the concentrated and distributed impact load cases (Models II and III) generate the largest contact force response (refer to Figure 7); but the concentrated impact load case produces the smallest maximum displacement (refer to Figure 8). Thus, one can conclude that the model

with a concentrated impact force (Model II) gives an overestimated peak contact force and a relatively conservative maximum deflection.

Table 1 Parameters used in the analytical case study

K_c, lbs/in (N/m)	K_{core}, lbs/in (N/m)	K_{bs}, lbs/in (N/m)	τ_w, psi (Pa)	M_s, lbs (kg)	A_s, ft^2 (m^2)	V, miles/h (m/s)
0.86×10^8 (1.54×10^{10})	0.56×10^6 (1.00×10^8)	0.48×10^6 (3.84×10^6)	1.45 (1.0×10^4)	0.080 (0.0361)	10.76 (1.0)	67.11 (30.0)

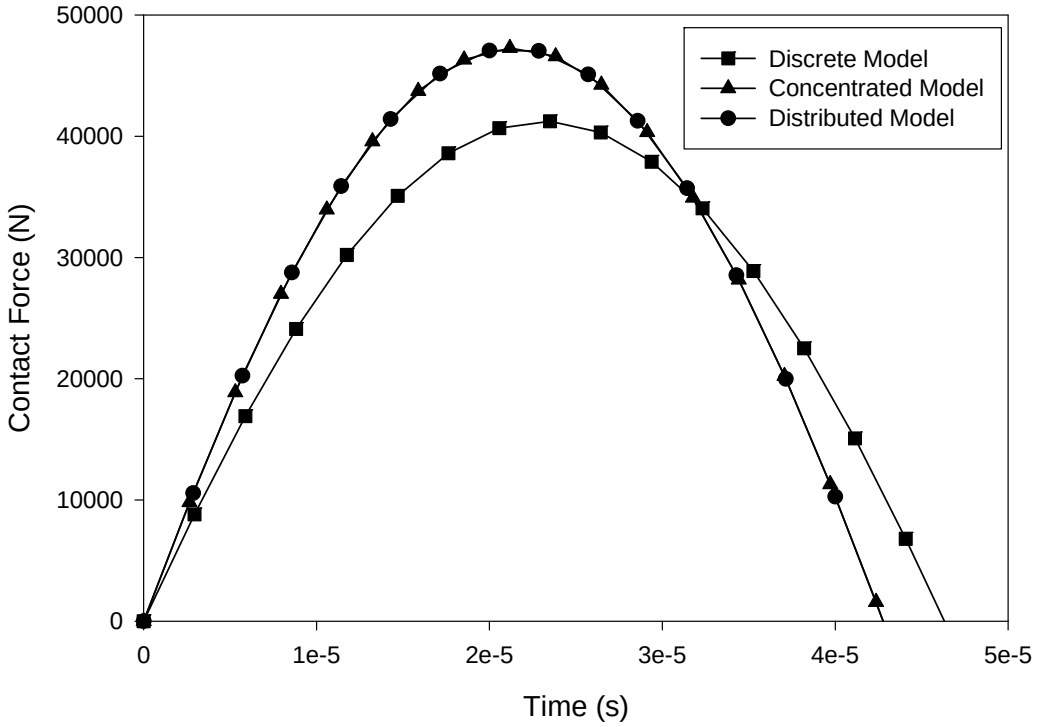

Figure 7 Contact force history of analytical models (1 N = 0.22 lbs)

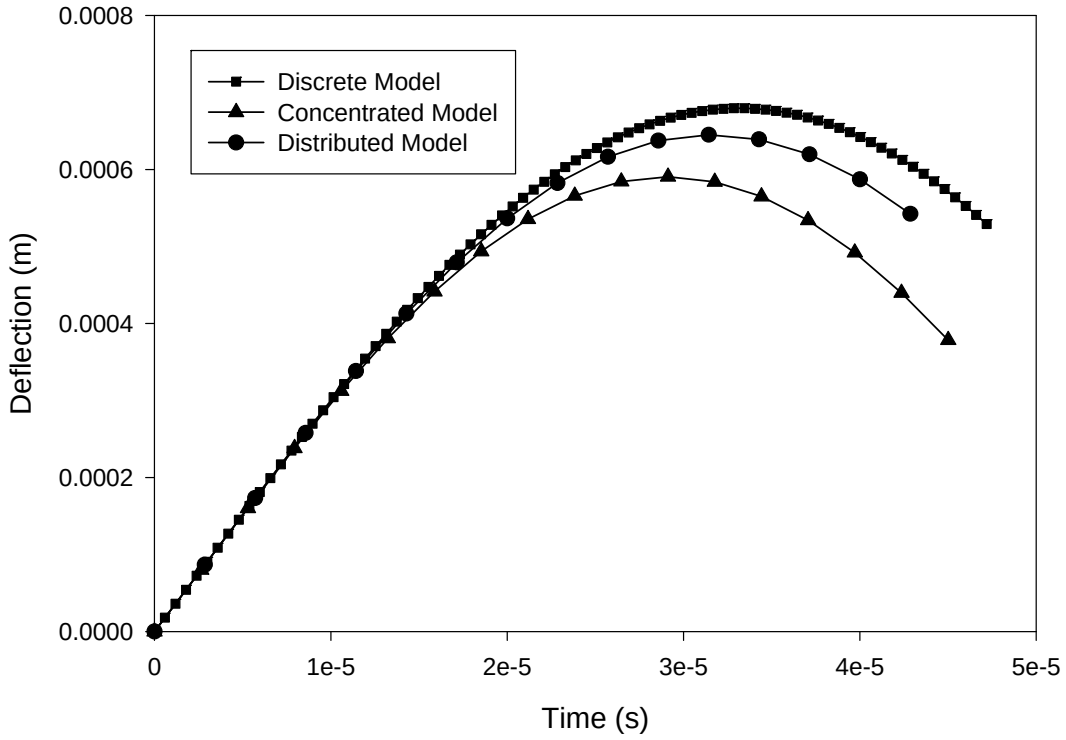

Figure 8 Maximum deflection history of the top face in the I-Lam sandwich beam (1 m = 39.4 in.)

The analytical model results also predict that the resultant contact force is influenced by the relative stiffness of the face sheet and core material. For example, the analytical results of the concentrated load model with an over-height mass of M_s = 79.59 lbs (0.0361 x 10^3 kg) (Figure 9) indicate that the resulting contact force is proportional to the relative stiffness (R) of the core material (K_{core}) with respect to the face sheet combined stiffness (K_{bs}),

$$R = \frac{K_{core}}{K_{bs}} \tag{15}$$

where $K_{bs} = 48E_f\left(\frac{bt^3}{12} + bth^2\right)/L^3$ and $K_{core} = E_{core}b$. In Figure 9, K_{bs} is kept as a constant, K_{core} changes as the ratio R increases. This proportionality between the relative core stiffness and the resulting peak force demonstrated in Figure 9 indicates that the stiffer the core material, the larger the contact force, and the core material plays a vital role in the impact response.

The influence of the shear-off effect (i.e., the shear strength of the over-height material) on the resulting peak contact force is also investigated. This is accomplished by performing the analytical procedure and the same parameters described earlier. The analytical results indicate that the resulting contact force is directly proportional to the shear strength of the over-height (shear-off) material as shown in Figure 10.

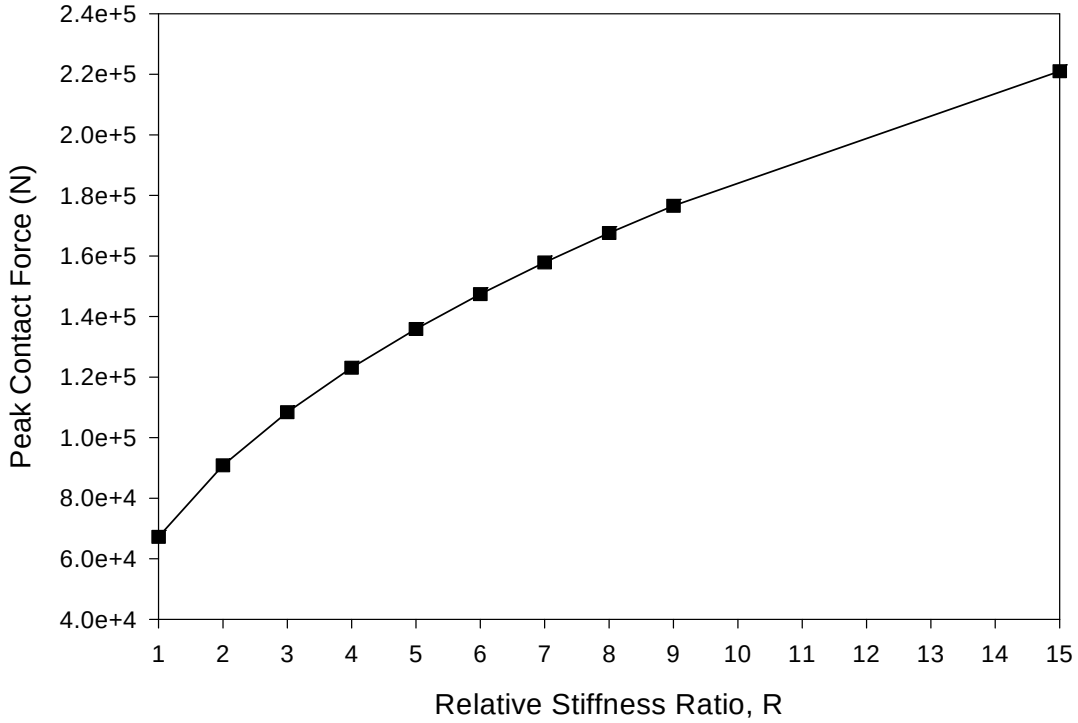

Figure 9 Effect of relative stiffness ratios (*R*) on peak contact force (1 N = 0.22 lbs)

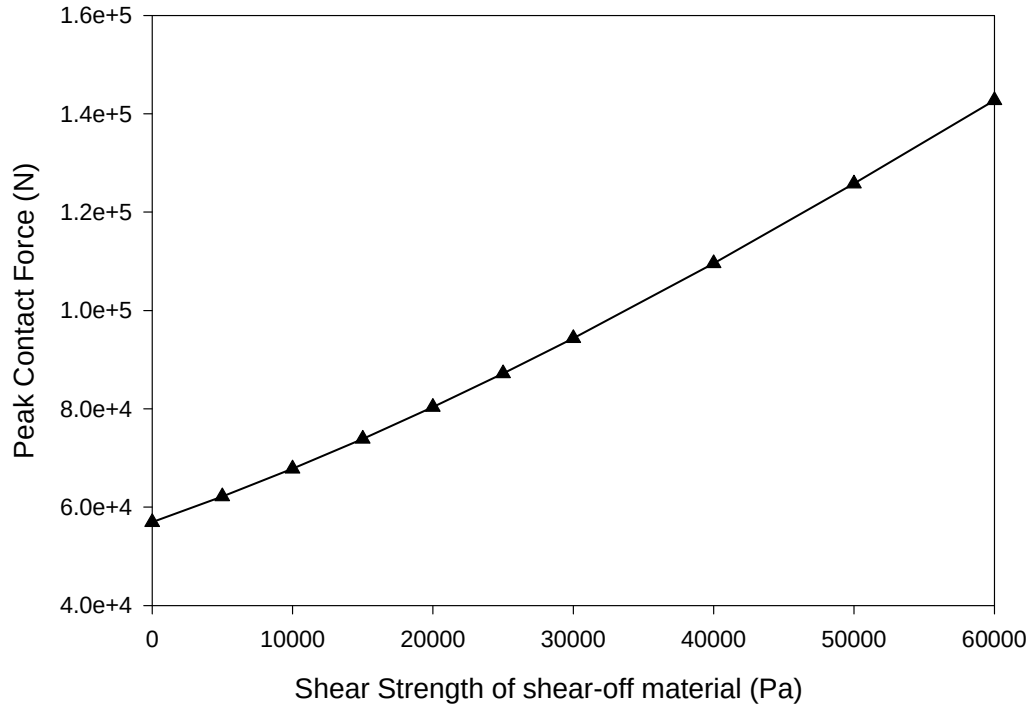

Figure 10 Effect of shear strength of the over-height material on peak contact force (1 N = 0.22 lbs)

4.2 Design Criteria

In Section 4.1, preliminary design analysis models considering shearing-off effect is

developed. In this section, a refined analysis is conducted, and design criteria are developed, which are useful for the practical design and analysis of I-Lam system.

Aluminum honeycomb materials are often used as a high efficient energy absorption structures, even though other types of candidate materials are available as well, like porous steel. Due to different application purposes, some materials can be used as impact resistant structures for low velocity impact protection (such as barrier or collision protection system for running vehicles), of which their yielding stresses are relatively small. Other types of applications (e.g., ballistic armor) produce the yielding stresses of the materials much higher in order to defect bullet projectiles.

The essence of protective structural design is its capacity to absorb energy, decelerate the projectile (i.e., the overheight material), and reduced the transferred force in the protected structures, so that the peak contact force on the protected structures (i.e., the concrete girders) is kept below the limits that will cause damage to the protected structures. Even though energy absorption of the proposed honeycomb I-Lam sandwich structure is mainly due to the crushing of honeycomb, the elastic impact analysis introduced in Section 4.1 can still provide an approximate and upper bound estimation about the peak contact force. With consideration of core crushing, the elastic-plastic impact analysis (Yang 2006) is used to refine the elastic impact design and provide accurate estimations about energy absorption of the protective sandwich structures as well as the peak contact force of the protective sandwich structures.

Based on the above considerations, the following three design criteria are proposed, and they provide the general guidelines for designing protective I-Lam sandwich structures:

(1) **Contact Force Limit Design**: The contact force (impact load) generated by the shear-off material should be small enough to keep the intact of the protected concrete girder:

$$P_c \le f_c^{'} A \tag{16}$$

where P_c is the contact force; $f_c^{'}$ is the compressive strength of concrete material; A is the contact area. It is noted that only a pure compressive failure is considered here. However, other types of failure of the concrete could be counted as well for further analysis.

(2) **Deflection Limit Design**: Similarly, the maximum deflection produced by impact of the shear-off material over the protective sandwich structure should be less than the densification displacement of the honeycomb sandwich structure:

$$\Delta_{\max} \le \Delta_{densify} \tag{17}$$

where $\Delta_{\max}$ is the maximum history displacement; $\Delta_{densification}$ is the densification displacement of the honeycomb core material.

(3) **Energy Absorption Limit Design**: The kinetic energy generated by the shear-off material consists of three parts: (a) Energy absorbed by the honeycomb core material, (b) Residual kinetic energy of the over-height material; and (c) Energy dissipated by deformation

and failure of the shear-off material itself. The energy portion absorbed by the honeycomb core material should be less than the maximum crushing energy of the core.

$$U_{core} = U_{kinetic} + W_{shear-hardening} - U_{residual} - U_{material} \le U_{crushing} \quad (18)$$

where U_{core} is the energy absorbed by the core material, $U_{kinetic}$ is the initial kinetic energy of the projectile; $W_{shear\text{-}hardening}$ is the work done by the shear hardening introduced by the vehicles; $U_{residual}$ is the residual kinetic energy of the shear-off material; $U_{material}$ is the energy dissipated by the failure of the projectile (i.e., the shear-off portion of overheight material) itself.

Based on the above three limit design criteria, three design methods are correspondingly developed to design the protective sandwich structures, i.e., contact force-based design, deflection-based design, and energy-based design. The tools used in the above design methods are elastic (Qiao et al. 2004) and elastic-plastic (Yang 2006) impact analysis as well as energy analysis.

4.3 Impact Velocity and Loading Conditions

For the real condition of the application, different types of shear-off materials, velocities of over-height materials and impact areas are considered. A parametric study is conducted to provide useful information for loading and impact requirements in design and material selection of the protective sandwiches for the case of over-height truck impact.

The vertical height of the sandwich structures is assumed about 12 in. (0.3048 m). The height of impact contact area is taken 20% ~ 100% of the height of the sandwich structures. Several candidate over-height materials (e.g., ice, wood, snow, etc.) are originally considered in the preliminary analysis, and the wood is chosen as the over-height (shear-off) material in the design analysis. The van trailer of 36 ton (36,000.0 kg) (NCHRP 350) is selected as the potential running truck, of which the over-height material hits the protective I-Lam sandwich structures (Figure 4). The following velocities of Van Trailer are considered in the parametric study: (1) 40 km/h (11.11 m/s; 24.85 miles/hour), (2) 60 km/h (16.67 m/s; 37.28 miles/hour), (3) 80 km/h (22.22 m/s; 49.71 miles/hour), and (4) 100 km/h (27.78 m/s; 62.14 miles/hour).

Based on the size of the van trailer and the height of impact contact area, the mass of over-height portion, which is sheared-off from the trailer, is estimated in Table 2.

Table 2 Mass of the overheight wood material with overheight of 12 in. (0.3048 m)

Vehicle type	36 ton (36,000.0 kg) Van Trailer
Over height shear-off area (L, length × W, width)	L (1.64~50.03 ft. (0.5~15.25 m) × W (5.41 ft. (1.65 m))
Mass (m (kg) of shear-off wood) (ρ = 37.46 pcf (0.6 ×10^3 kg/m^3))	m = 0.0666~10,141.26 lbs (0.0302~4.60×10^3 kg)

For the protective sandwich structures, the through-the-thickness stiffness coefficient of the core material is taken as 6,886.24 psi ($\frac{E_c b}{h_c} = 4.748 \times 10^7 N/m^2$) or from the crushing experimental results (Yang 2006). The shear strength of the wood material is chosen as a regular value of 725.68 psi (5.0 MPa). Here we need to mention that the shear-off will happen as soon as the projectile makes contact with the I-Lam protective structures.

4.4 Design of Collision Protection System

The empirical elastic-plastic impact analysis model considering shear-off effect and flat crushing impact (Yang 2006) is presented as follows. The design analysis procedures based on three-stage processes are first given, followed by a design flow chart. The energy absorption analysis and the results based on the proposed design analysis procedures are then presented.

4.4.1 Design analysis procedures

The design of I-Lam protective sandwiches is realized through three different processes involved in the impact: elastic impact, elastic-plastic impact, and impact loading after densification, and they are coupled with the shear-off process of the over-height material.

The speed of shearing-off the over height material takes place as the shear wave velocity,

$$C_s = \sqrt{\frac{G}{\rho}} \tag{19}$$

where G and ρ are the shear modulus and density of shearing-off materials, respectively;

The time for the shear-off to be completed is

$$t_{shear} = \frac{L}{C_s} \tag{20}$$

where L is the length of the shear off material; t_{shear} is the time to completely shear off the over-height material.

The elastic-plastic impact considering the progressive shear-off effects can be divided into the following three stages (Yang 2006):

(1) **Elastic impact**: The governing equation for elastic impact with shear-off effect is expressed as,

$$m\ddot{\delta} + \tau b(L - C_s t) = -P \qquad 0 < t < t_{yield} < t_{shear} \tag{21}$$

$$P = K_h \delta \tag{22}$$

where δ is the displacement of the projectile; K_h is the contact stiffness of the projectile and the sandwich; b is the width of the projectile; t is the time; m is the shear-off mass; P is the resultant contact force.

Differentiating Eq. (21) with respect to t results in

$$m\dddot{\delta} + K_h\ddot{\delta} - \tau bC_s = 0 \tag{23}$$

The Initial conditions for this case are

$$\delta(0) = 0\,,\ \ \dot{\delta}(0) = v_0\,,\ \ \ddot{\delta}(0) = 0 \tag{24}$$

Otherwise

$$m\ddot{\delta} + \tau b(L - C_s t) = -P \quad 0 < t < t_{shear} < t_{yield} \tag{25}$$

$$m\ddot{\delta} = -P \quad t_{shear} < t < t_{yield} \tag{26}$$

$$m\ddot{\delta} = -P_Y \quad t_{yield} < t \tag{27}$$

where P_y is the crushing resultant force of the protective sandwich; t_{yield} is the time of the protective sandwich at the verge of yielding (in this study, a 1-D maximum strain yield criterion is applied, and the maximum yield strain is set as 0.075).

(2) **Elastic-plastic impact**: The governing equation for elastic-plastic loading with shear-off effect is,

$$m\dddot{\delta} - \tau bC_s = 0 \quad t_{yield} < t < t_{shear} < t_{densification} \tag{28}$$

The governing equation for elastic-plastic loading without shear-off effect is,

$$m\ddot{\delta} = -P_y \quad t_{yield} < t_{shear} < t < t_{densification} \tag{29}$$

with the displacement, velocity as well as the acceleration continuous at $t = t_{yield}$.

While for the elastic unloading in the plastic region,

$$m\ddot{\delta} + K_u(\delta - \delta_r) = 0 \tag{30}$$

where K_u is the unloading contact stiffness of the projectile and the sandwich; δ_r is the residual deformation of the protective sandwich.

(3) **Densification loading**: Once the I-Lam structure goes through the elastic and elastic-plastic loading, it then finally reaches the densification stage, in which the I-Lam honeycomb material is consolidated and no further crushing deformation of I-Lam is allowed. The governing equation for densification loading process considering the shear-off effect is given as,

$$m\ddot{\delta} + K_D(\delta - \delta_D) + P_y + \tau b(L - C_s t) = 0 \qquad t_{densification} < t < t_{shear} \tag{31}$$

where K_D is the densification loading contact stiffness of the projectile and the sandwich; δ_D is the densification deformation of the protective sandwich.

Differentiating Eq. (31) with respect to t lead to,

$$m\dddot{\delta} + K_D\dot{\delta} - \tau b C_s = 0 \qquad t_{densification} < t < t_{shear} \tag{32}$$

with the displacement, velocity as well as the acceleration continuous at $t = t_D$.

The governing equation for densification loading without the shear-off effect is given as,

$$m\ddot{\delta} + K_D(\delta - \delta_D) + P_y = 0 \qquad t_{densification} < t_{shear} < t \tag{33}$$

The elastic unloading after densification is given as,

$$m\ddot{\delta} + K_u(\delta - \delta_r) = 0 \qquad t_{densification} < t_{shear} < t \tag{34}$$

Subjected to the conditions that the displacement, velocity as well as acceleration are continuous at $t = t_{densification}$ and $t = t_{shear}$, the above equations (Eqs. (33) to (34)) can be analytically solved.

4.4.2 Design flow chart

Based on the above three stages of impact analysis, a detailed design method can be followed through the flow chart shown in Figure 11.

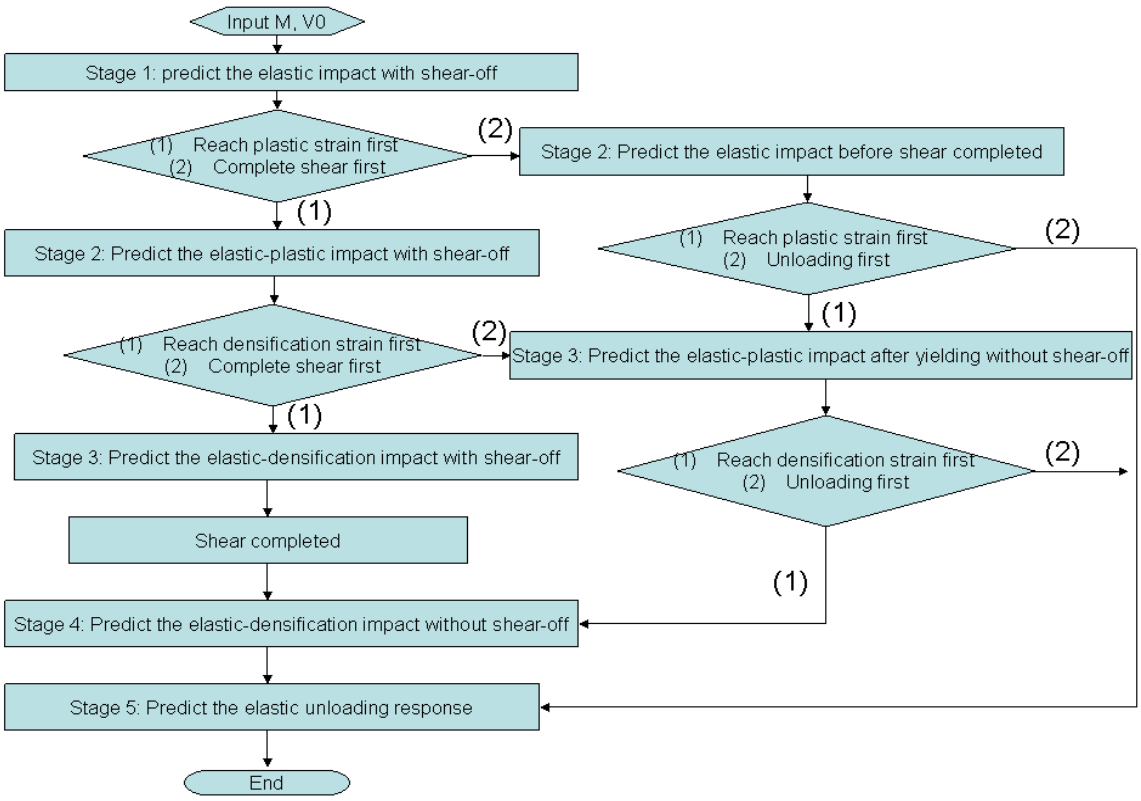

Figure 11 Flowchart for design of an I-Lam sandwich system with shear-off effect

4.4.3 I-Lam final design

Based on the design requirements (Section 4.3) and design protocol (Sections 4.4.1 and 4.4.2), a double-layer aluminum honeycomb I-Lam sandwich system is designed for the overheight collision protection. The double-layer I-Lam system (Figure 12) consists of two thin face sheets (top and bottom) and two 4" thick honeycomb layers with crushing strength of 90 psi and 210 psi, respectively. The lower crushing strength honeycomb layer is designed for the impact/collision of lighter overheight materials and low speed; while the higher crushing strength honeycomb layer is intended for the case of heavier overheight sheared-off materials and high speed. The purpose of using the two-layer honeycomb configuration is to improve structural efficiency. The final product of I-Lam system is shown in Figure 13, and it was manufactured and supplied by Plascore, Inc., Zeeland, MI.

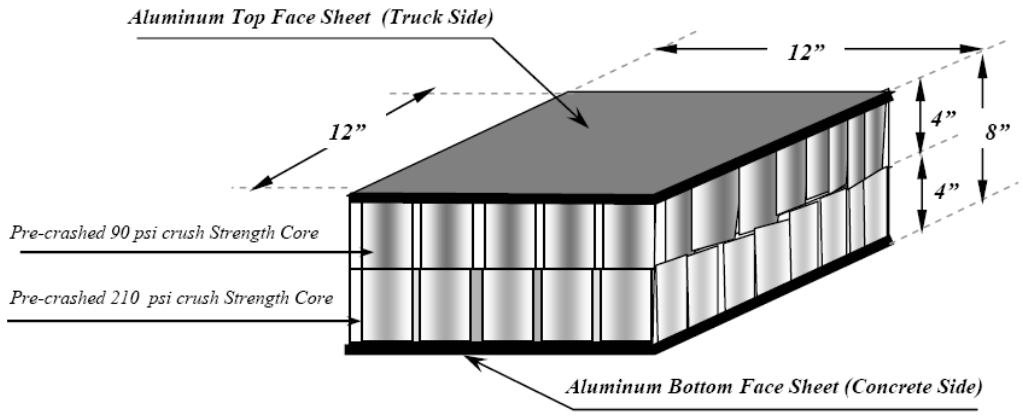

Figure 12 Final design of double-layer aluminum honeycomb sandwich for collision protection (I-Lam system)

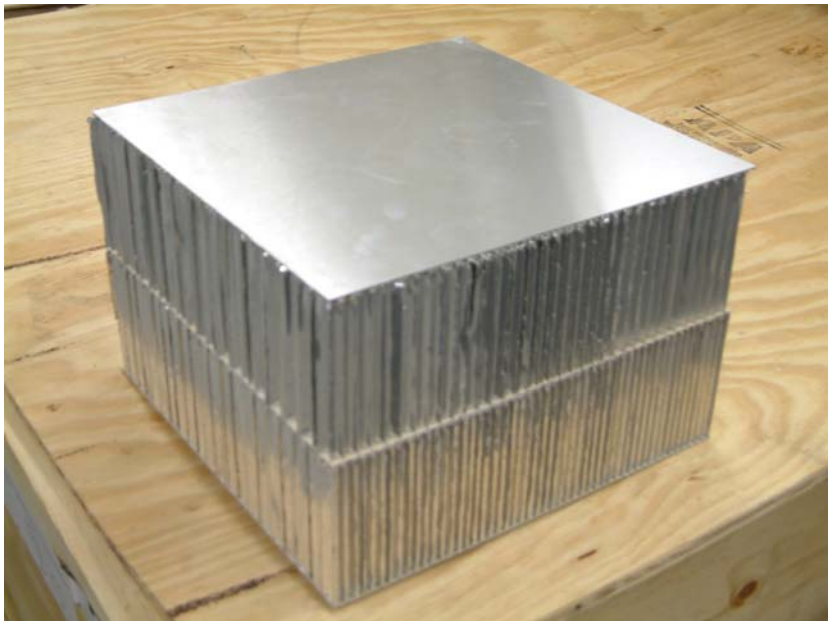

Figure 13 Double-layer I-Lam sandwich sample (12 x 12 x 8 in.)

4.4.4 Design results

An analysis of the finalized I-Lam is conducted using the above design analysis procedures. The yield strain of 0.075 and the densification strain of 0.90 for the aluminum honeycomb core materials in I-Lam are used in the analysis. The simulations have been conducted for two different mass and initial velocity combinations of the projectile (i.e., the sheared-off overheight material; also see the impact velocity and loading condition in Table 2). The contact force histories and the displacement histories are plotted in Figures 14 and 15, respectively.

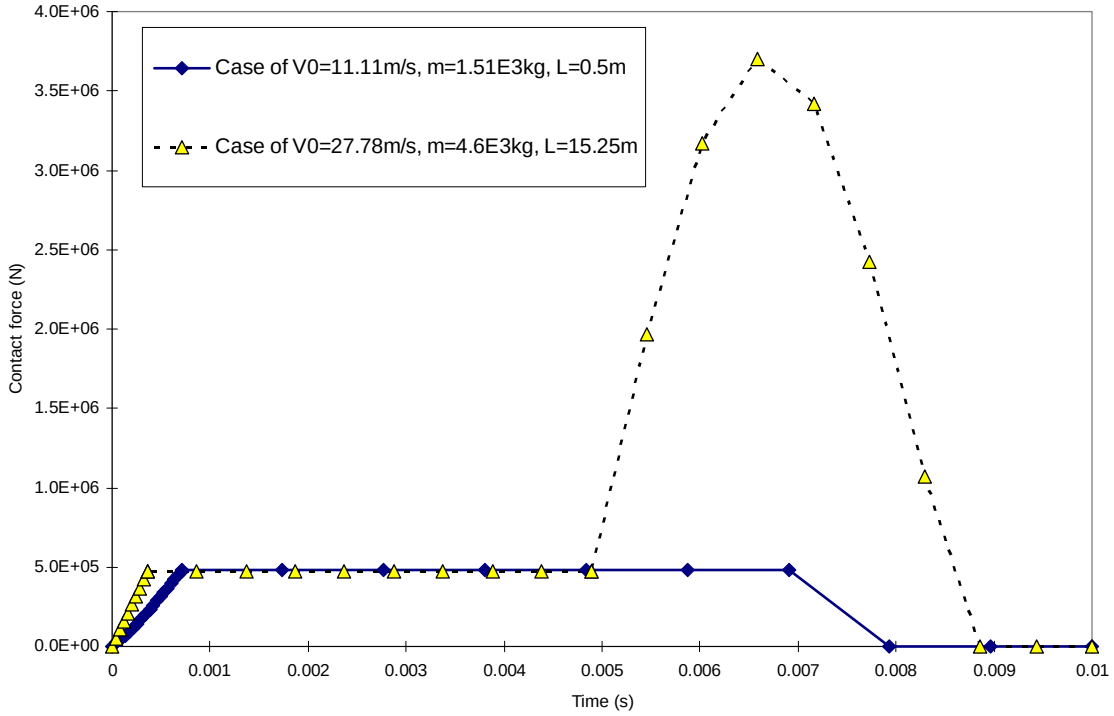

Figure 14 Contact force history of a 72 x 12 x 8 in. aluminum sandwich I-Lam (Note: 1 N = 0.225 lbs)

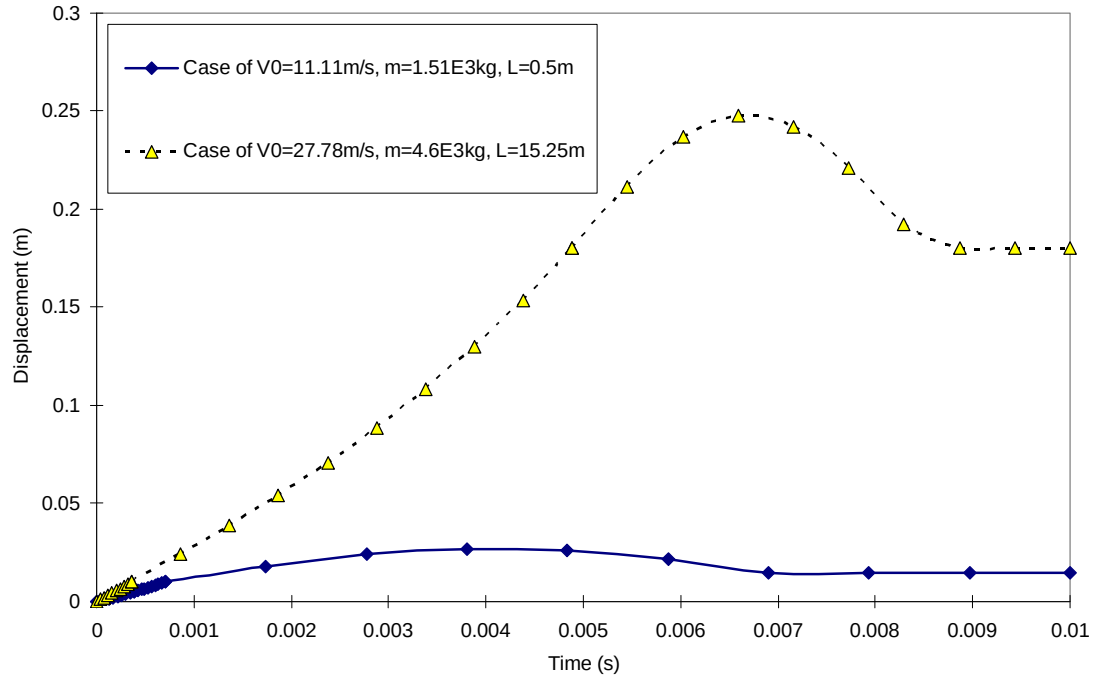

Figure 15 Displacement history of a 72 x 12 x 8 in. aluminum sandwich I-Lam (Note: 1 m = 39.37 in.)

The maximum contact forces and the maximum deflections of the 72 x 12 x 8 in. (183 x 30.5 x 20.3 cm) I-Lam sandwich panel impacted under different impact velocity and loading cases (Table 2) are computed and given in Table 3. From Table 3, it is noted that for the cases of large projectile (the shear-off portion of overheight material) masses, the shear-off effect is dominant, which leads to the densification of the honeycomb core. For the cases of small projectile (overheight material) masses, the I-Lam well behaves and absorbs all the kinetic energy of the projectile.

Table 3 Contact force and deflection for a 72 x 12 x 8 in. aluminum sandwich under different impact velocity and loading conditions

H (0.3048m)	L (m)	m (10^3 kg)	Velocity (m/s)	L/C_s (s)	Start time to crushing (s)	Maximum Contact Force (N)	Max Deflection (m)
0.2	0.5	0.0302	11.11	0.000385	0.00045	480000	0.019
1.0	0.5	0.151	11.11	0.000385	0.00064	480000	0.028
0.2	15.25	0.92	11.11	0.011731	0.00081	3.16E6	0.238
1.0	15.25	4.6	11.11	0.011731	0.00088	4.16E6	0.258
0.2	0.5	0.0302	16.67	0.000385	0.00040	480000	0.034
1.0	0.5	0.151	16.67	0.000385	0.00052	480000	0.058
0.2	15.25	0.92	16.67	0.011731	0.00058	3.09E6	0.240
1.0	15.25	4.6	16.67	0.011731	0.00060	3.96E6	0.255
0.2	0.5	0.0302	22.22	0.000385	0.00035	480000	0.048
1.0	0.5	0.151	22.22	0.000385	0.00042	480000	0.102
0.2	15.25	0.92	22.22	0.011731	0.00044	3.02E6	0.235
1.0	15.25	4.6	22.22	0.011731	0.00045	3.73E6	0.250
0.2	0.5	0.0302	27.78	0.000385	0.00031	480000	0.054
1.0	0.5	0.151	27.78	0.000385	0.00034	480000	0.067
0.2	15.25	0.92	27.78	0.011731	0.00036	2.95E6	0.233
1.0	15.25	4.6	27.78	0.011731	0.00036	3.70E6	0.252

Note: US unit. 1 m = 39.4 in., 1 N = 0.224 lb and 1 kg = 2.22 lb.

4.4.5 Energy analysis

Analysis based on energy provides the insight for functions of different components in the impact process of I-Lam system. Based on whether the projectile will fail or not, a simple energy analysis is proposed.

If the projectile (i.e., the shear-off portion of the overheight material) does not fail, the energy conservation equation is

$$\frac{1}{2} m_{shear-off} (1-e)^2 v^2 + \tau \gamma_{failure} bLt_{shear} - E_{absorbed} - E_{indentation} = 0 \qquad (35)$$

where $m_{shear\text{-}off}$ is the shear-off mass; e is the restitute coefficient of the projectile; L is length of the over-height material; t_{shear} is the thickness of the shear layer, which is taken as 1.18 in (0.030 m) for wood material; b is the width of the projectile; τ is the shear strength of the overheight material; γ_{failure} is the maximum failure shear strain; $E_{absorbed}$ is the energy absorbed by the honeycomb; $E_{indentation}$ is the energy dissipated by the impact indentation process.

If the projectile fails (the damage in the shear-off portion of the overheight material is included), the energy conservation equation becomes

$$\frac{1}{2} m_{shear-off} v^2 + \tau \gamma_{failure} bLt_{shear} - E_{absorbed} - E_{indentation} - \sigma_f bh\varepsilon_f \beta L = 0 \qquad (36)$$

where σ_f is the compressive strength of the overheight material; ε_f is the maximum compressive strain; β is the percentage of the projectile volume failed due to the impact contact, which is chosen as 0.8 for wood materials.

From the energy equation and assuming the indentation energy is zero, different energy partitions of different components of the sandwich I-Lam system are calculated (Tables 4 and 5) for the cases of projectiles with and without failure of the projectile. In this study, the wooden material is used as projectile to simulate the effect of the shear-off portion of overheight material. In Table 4, the restitute coefficient is chosen as 0.5. In Table 5, σ_f is chosen as 1,451.36 psi (10 MPa) and E_f as 3.628×10^6 psi (2.5 GPa).

Table 4 Energy partition for the case of the projectile bounced back

H (0.3048 m)	*L* (m)	*m* (10^3 kg)	Velocity (m/s)	Lost kinetic energy (kJ)	Lost shear energy (kJ)	Energy need to be absorbed (kJ)
0.2	0.5	0.0302	11.11	0.47	0.62	1.08
1.0	0.5	0.151	11.11	2.33	0.62	2.95
0.2	15.25	0.92	11.11	14.19	18.87	33.07
1.0	15.25	4.6	11.11	70.97	18.87	89.85
0.2	0.5	0.0302	16.67	1.05	0.62	1.67
1.0	0.5	0.151	16.67	5.25	0.62	5.86
0.2	15.25	0.92	16.67	31.96	18.87	50.83
1.0	**15.25**	**4.6**	**16.67**	**159.79**	**18.87**	**178.66**
0.2	0.5	0.0302	22.22	1.86	0.62	2.48
1.0	0.5	0.151	22.22	9.32	0.62	9.94
0.2	15.25	0.92	22.22	56.78	18.87	75.65
1.0	**15.25**	**4.6**	**22.22**	**283.89**	**18.87**	**302.77**
0.2	0.5	0.0302	27.78	2.91	0.62	3.53
1.0	0.5	0.151	27.78	14.57	0.62	15.19
0.2	15.25	0.92	27.78	88.75	18.87	107.62
1.0	**15.25**	**4.6**	**27.78**	**443.74**	**18.87**	**462.62**

Note: Energy absorption capacity of the given honeycomb is 30,000 x 4 x 6 x 0.2 J = 144 KJ; Note: US unit. 1 m = 39.4 in., 1 N = 0.224 lb and 1 kg = 2.22 lb

Table 5 Energy partition for the case of the projectile totally failed (crushed)

H (0.3048m)	*L* (m)	*m* (10^3 kg)	Velocity (m/s)	Lost kinetic energy (KJ)	Lost shear energy (KJ)	Energy consumed by failure of projectile (KJ)	Energy need to be absorbed (KJ)
0.2	0.5	0.0302	11.11	1.86	0.62	1.61	0.87
1.0	0.5	0.151	11.11	9.32	0.62	8.05	1.89
0.2	15.25	0.92	11.11	56.78	18.87	49.08	26.57
1.0	15.25	4.6	11.11	283.89	18.87	245.42	57.34
0.2	0.5	0.0302	16.67	4.20	0.62	1.61	3.21
1.0	0.5	0.151	16.67	20.98	0.62	8.05	13.55
0.2	15.25	0.92	16.67	127.83	18.87	49.08	97.62
1.0	**15.25**	**4.6**	**16.67**	**639.14**	**18.87**	**245.42**	**412.59**
0.2	0.5	0.0302	22.22	7.46	0.62	1.61	6.46
1.0	0.5	0.151	22.22	37.28	0.62	8.05	29.85
0.2	**15.25**	**0.92**	**22.22**	**227.12**	**18.87**	**49.08**	**196.90**
1.0	**15.25**	**4.6**	**22.22**	**1135.58**	**18.87**	**245.42**	**909.02**
0.2	0.5	0.0302	27.78	11.65	0.62	1.61	10.66
1.0	0.5	0.151	27.78	58.27	0.62	8.05	50.84
0.2	**15.25**	**0.92**	**27.78**	**355.00**	**18.87**	**49.08**	**324.78**
1.0	**15.25**	**4.6**	**27.78**	**1774.98**	**18.87**	**245.42**	**1548.42**

Note: US unit. 1 m = 39.4 in., 1 N = 0.224 lb and 1 kg = 2.22 lb.

4.5 Simulation of Collision Protection System

In this section, two sets of numerical finite element simulations are conducted: (1) plain concrete beams with and without I-Lam protection, and (2) reinforced concrete beams with and without I-Lam protection. The analysis is carried out using the commercial finite element software LS-DYNA, a primer software for dynamic and impact analysis.

4.5.1 Analysis of plain concrete beams with and without I-lam protection

Two types of concrete beams are selected: plain concrete and reinforced concrete beams. The impact/crash process is simulated using the commercial finite element software, LS-DYNA. The material model chosen for concrete is *MAT_BRITTLE_DAMAGE_TITLE with its density as 140.27 pcf (2.247 x 10^3 kg/m^3), Young's modulus E as 3.727 x 10^6 psi (25.7 GPa), v as 0.19, tensile strength as 43.51 psi (0.30 MPa), shear strength as 3,045.80 psi (21.0 MPa) and compressive strength as 5,975.55 psi (41.2 MPa) with 8% steel reinforcement. The steel properties are chosen as E = 3.336 x 10^7 psi (230 GPa) with its tensile strength as 54,099.05 psi (373 MPa).

The material model chosen for the wooden projectile is *MAT_BRITTLE_DAMAGE_TITLE with density as 34.38 pcf (550.0 kg/m^3), E as 1.17 x 10^6 psi (8.05 GPa), v as 0.35, tensile strength as 217.55 psi (1.5 MPa), and shear strength as 754.20 psi (5.2 MPa). The aluminum honeycomb core in I-Lam is treated as an equivalent homogenous material, and its material properties are derived from the experiments (Yang 2006). The following is a list of input for the material parameters in LS-DYNA:

```
*MAT_BRITTLE_DAMAGE_TITLE
M-1
$       MID            RO             E           PR      TLIMIT      SLIMIT      FTOUGH      SRETEN
          12.2470E-09     25700.0         0.19         0.30         21.0
$      VISC      FRA_RF        E_RF       YS_RF       EH_RF       FS_RF        SIGY
                 0.080    230000.0       373.0                                  41.2
*MAT_BRITTLE_DAMAGE_TITLE
M-2
$       MID            RO             E           PR      TLIMIT      SLIMIT      FTOUGH      SRETEN
          25.5000E-10      8050.0         0.35         1.5          5.2
$      VISC      FRA_RF        E_RF       YS_RF       EH_RF       FS_RF        SIGY

*MAT_FINITE_ELASTIC_STRAIN_PLASTICITY_TITLE
M-4
$       MID            RO             E           PR        SIGY        ETAN
          46.2100E-11       109.0         0.25         0.86          0.0
$         C              P          LCSS         LCSR
        0.0            0.0       9045.0          0.0
$      EPS1         EPS2         EPS3         EPS4         EPS5         EPS6         EPS7         EPS8
        0.0          0.0          0.0          0.0          0.0          0.0          0.0          0.0
$       ES1          ES2          ES3          ES4          ES5          ES6          ES7          ES8
        0.0          0.0          0.0          0.0          0.0          0.0          0.0          0.0
```

In Figure 16, the "bare-concrete" case represents that the concrete beam is not protected by the I-Lam, and it is impacted with the 20 in. (0.5 m) long and 12 x12 in. cross-section wooden projectile. The "protected-concrete-1" case indicates that the concrete beam is protected by the I-Lam sandwich, and the concrete beam is deformable; while the "protected-concrete-2" case represents that the concrete beam is protected by the I-Lam sandwich, and the concrete beam sets infinitely rigid so that a rigidly- and fully-backed condition is simulated. The simulation results in term of contact force history are shown in Figure 16.

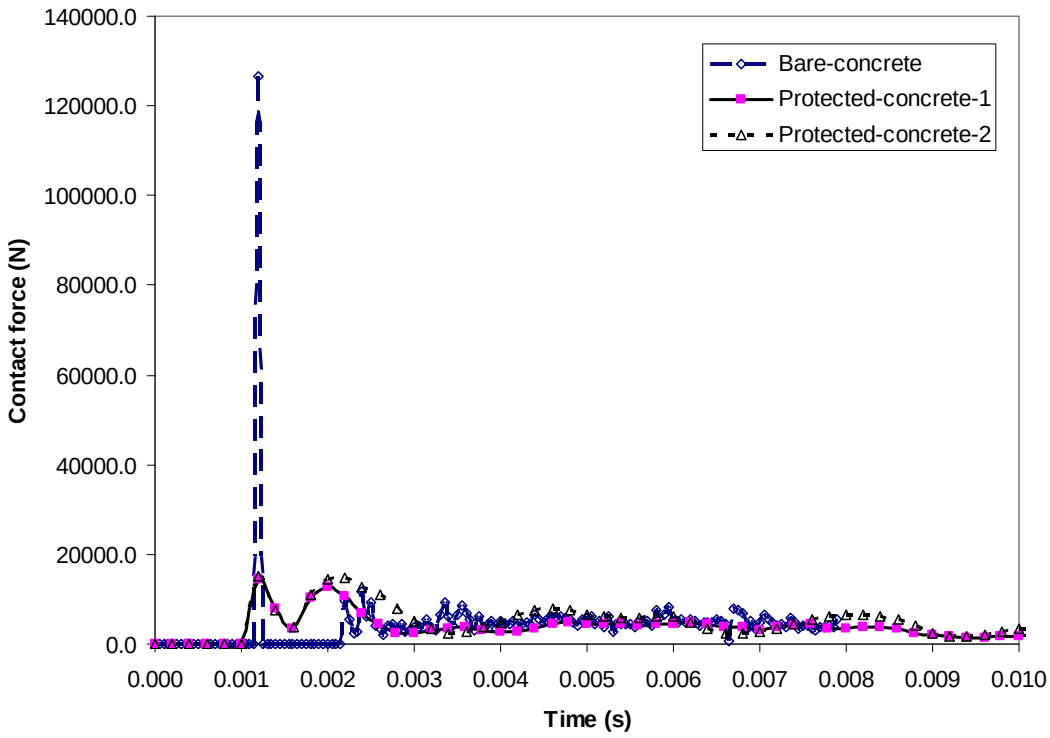

Figure 16 Comparison of contact force history for three different cases of plain concrete beam (with steel reinforcement) (1 N = 0.225 lbs)

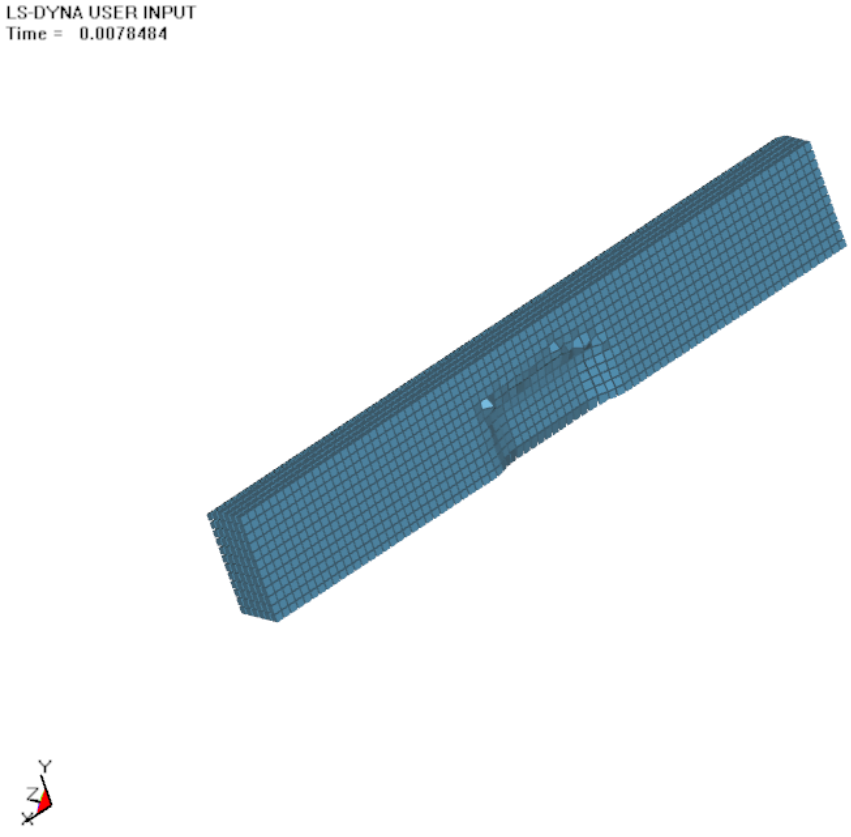

Figure 17 Eroded concrete surface

The resultant eroded surface of the concrete by the wooden projectile is shown in Figure 17. Because the concrete material is assumed to be stronger than the wood material of the projectile, the wooden projectile is crushed at the contact location and sheared off in the middle; however, at the same time, the concrete surface is eroded by the impact of the wooden projectile. From the contact force history (Figure 16), we could observe that the bare concrete beam is greatly damaged due to the high velocity involved in the impact process. The overheight wooden projectile is split off in the middle due to the shear-off mechanism. The wooden projectile makes the contact with the concrete beam first, and the contact force reaches to about 26,977 lbs (120,000 N) for the 12 x 12 x 20 in. wooden projectile.

From the contact force history (Figure 16) of the impact process with the protective I-Lam, it is noted that the concrete beam deforms globally due to the contact force produced during the contact between the I-Lam and the wood projectile. Also the overheight wooden projectile is split off in the middle due to the shear-off mechanism. In this case with I-Lam protection, the contact force is significantly reduced to 3,597 lbs (16,000 N) for the 12 x 12 x 20 in. wooden projectile, which is even less than the quasi-static crushing force for a 6 x 6 x 8 in. aluminum bi-layer honeycomb I-Lam (see Figures 12 and 13) (Yang 2006).

From the contact force history (Figure 16) of the impact process for the rigid concrete beam with the I-Lam protection, the overheight wooden projectile is again split off in the middle due to the shear-off mechanism, and the contact force is about 3,710 lbs (16,500 N) for the 12 x 12 x 20 in. wooden projectile, which is also less than the quasi-static crushing force (Yang 2006) for a 6 x 6 x 8 in. aluminum bi-layer honeycomb.

4.5.2 Analysis of reinforced concrete beams with and without I-Lam protection

For the concrete beams reinforced with steel rebars, two simulations (with and without I-Lam protection) are also conducted, and the finite element simulation results are shown in Figures 18 and 19 for the cases of bare and I-Lam protected reinforced concrete beams, respectively. The resultant contact forces for the reinforced concrete beams are shown in Figure 20, and the contact force generated by the contact of bare concrete beam with the wooden projectile is much higher than that generated by the contact with aluminum honeycomb I-Lam. Physically, due to the higher stiffness in the thickness direction associated with the concrete beam, the contact stiffness between the bare reinforced concrete beam and the wooden projectile is much higher than the one between the aluminum I-Lam and the wooden projectile, leading to a higher contact force and a short pulse type contact force time history (Figure 20). However, for the protected beam case, due to the sacrificing effect of the honeycomb aluminum, the contact force shows a stable contact force with longer contact duration, thus meeting the objective of reducing the transferred contact force to the underneath protected structures, i.e., the concrete beams. In terms of energy absorption, the I-Lam absorbs more energy than the bare concrete beam from the contact force time history (Figure 20). Also from the finite element simulation, it is observed that the upper surface of the unprotected concrete beam (Figure 18) is spalled, while that of the I-Lam protected concrete beam (Figure 19) is still intact.

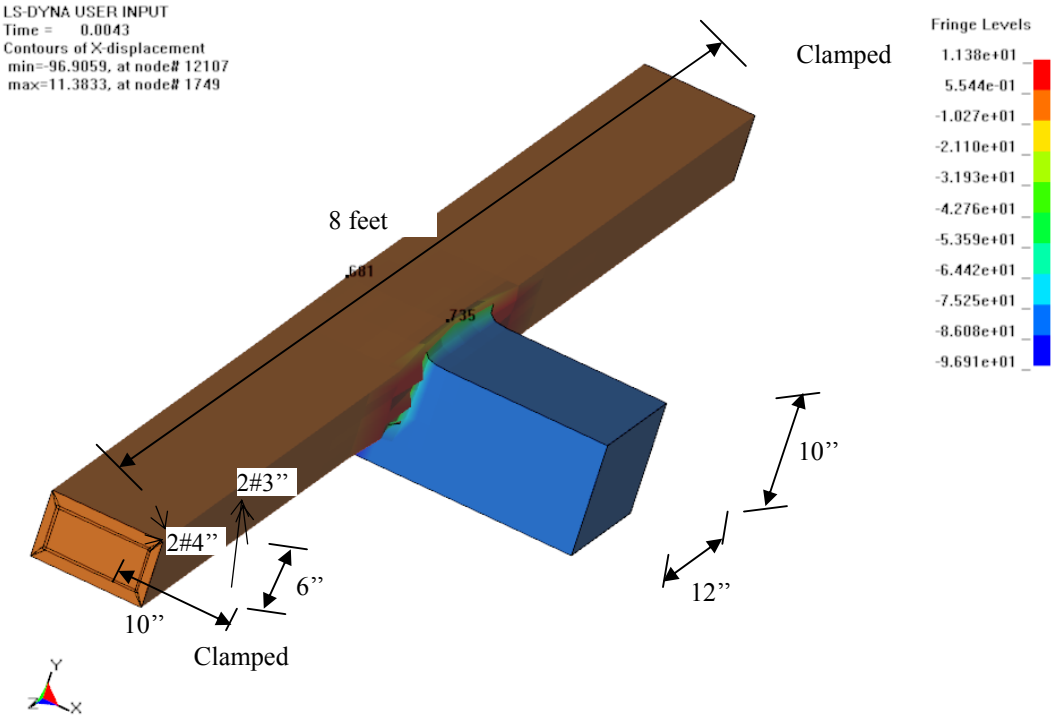

Figure 18 Finite element simulation of bare reinforced concrete beam

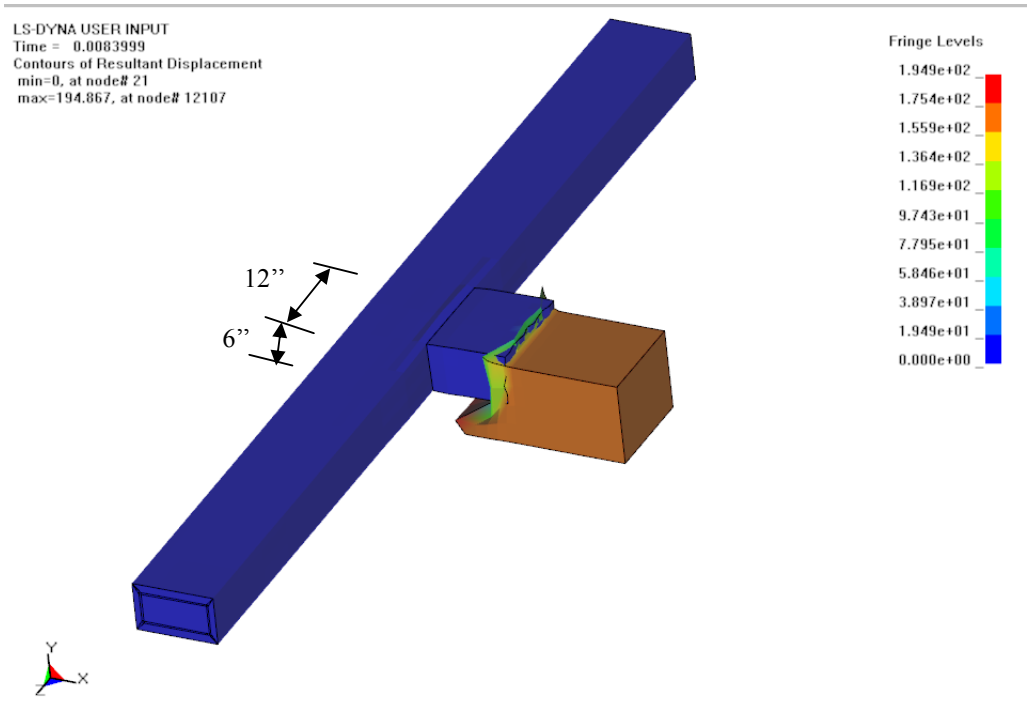

Figure 19 Finite element simulation of I-Lam protected reinforced concrete beam

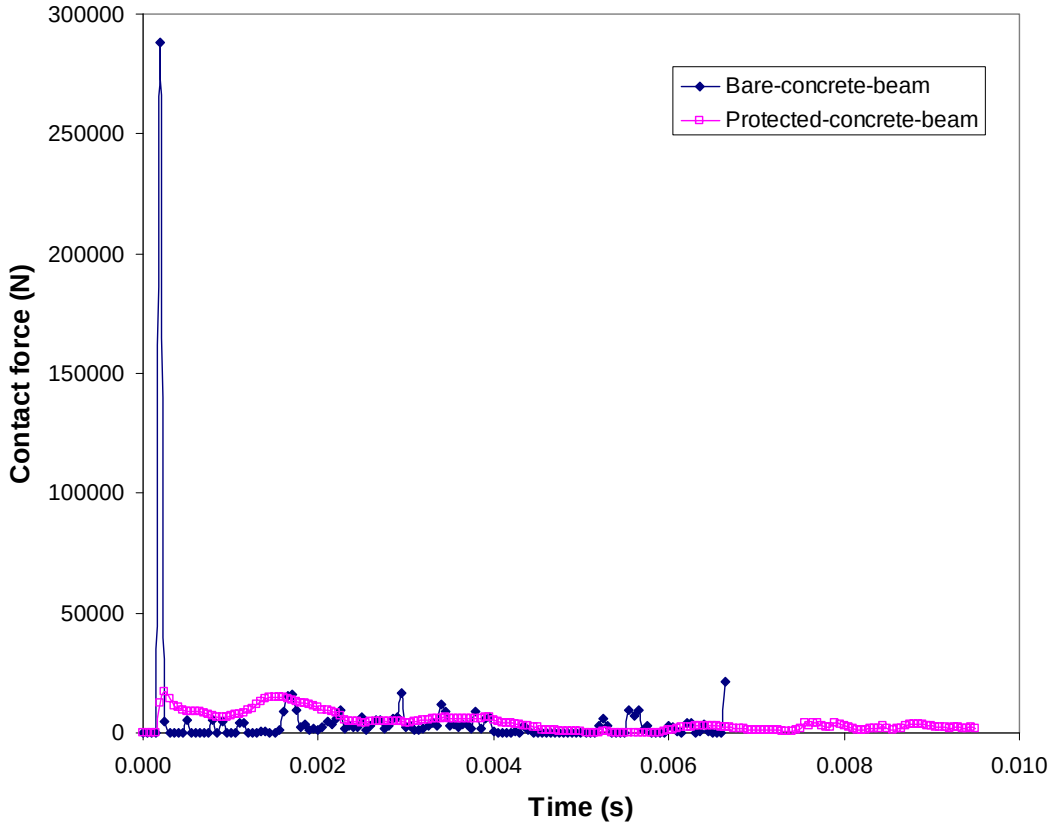

Figure 20 Comparison of contact forces of reinforced concrete beams (1 N = 0.225 lbs)

Deflection histories of two different nodes (i.e., at the central front (node #735) and back (node #681) of the concrete beams, see Figure 18) but at the same locations in the bare and protected concrete beam are also shown in Figures 21 and 22. It indicates that the bare concrete beam undergoes larger deflection compared to the I-Lam protected reinforced concrete beam. The large difference between the two cases and the small deformation in the I-Lam protected concrete beam are primarily due to small contact force generated in the contact between the I-Lam and the wooden projectile and the absorbed energy in the crushed core of I-Lam.

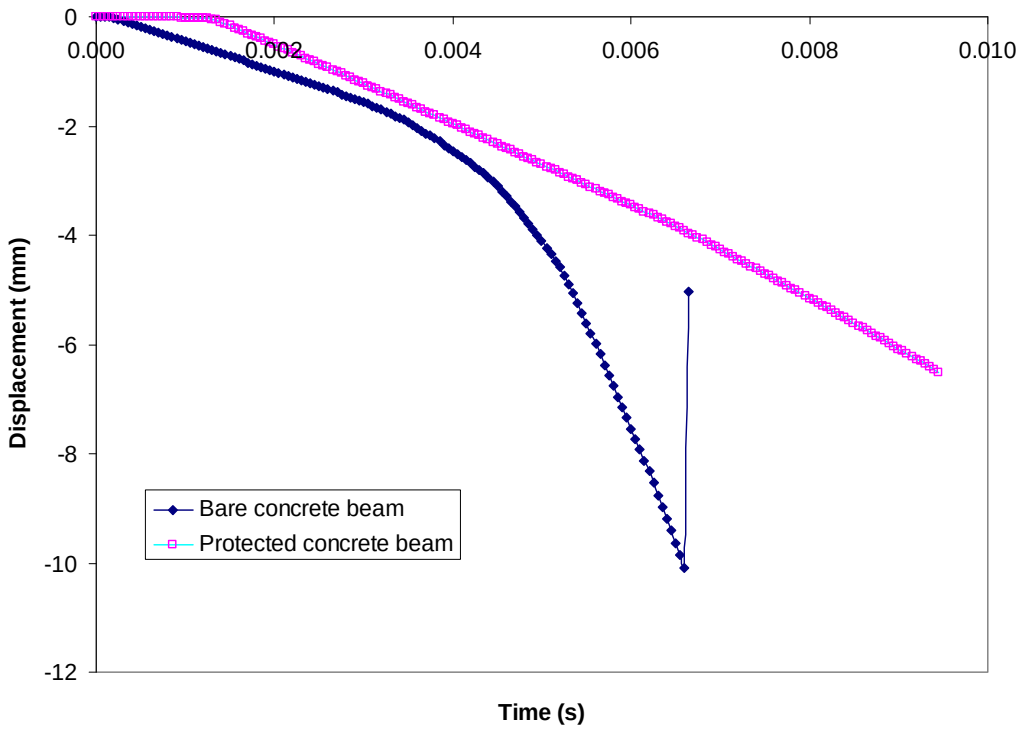

Figure 21 Comparison displacement at the impact contact location (contact front, Node #735, see Figure 18) (1 mm = 0.039 in)

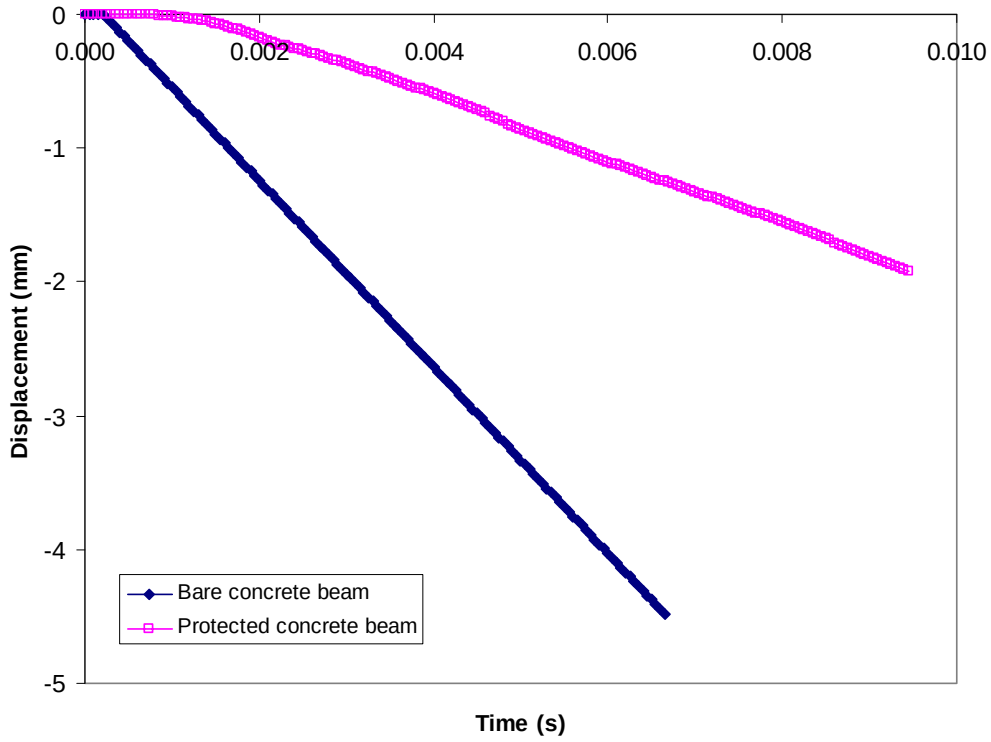

Figure 22 Comparison displacement at the impact contact location (beam back, Node #681, see Figure 18) (1 mm = 0.039 in)

Also it indicates that the contact surface of the unprotected concrete beam begins to spall at the time of 0.006 s from the reversed displacement (Figure 21); while the I-Lam protected concrete is still in the safe side. Also the displacement history of the unprotected beam rises rapidly as soon as the wooden projectile makes the contact with the concrete beam; while the displacement of I-Lam protected beam rises steadily.

Compared to the cases of plain concrete beams, the contact force history of the I-Lam protected beams is very similar (Figures 16 and 20). However, the contact force history of the unprotected "reinforced" concrete beam is two times higher than the previous case of "plain" concrete beam due to the increased beam stiffness by changing the impact direction and steel reinforcement, leading to a large contact force.

4.6 Design Recommendations for Implementation

From the above analytical solution and numerical simulations, the I-Lam design under different impact velocity, mass, and shear-off area are summarized in Table 6. The width of I-Lam is considered as 72", and it consists of 6 pieces of side-by-side of 12"-wide I-Lam panels. Be aware that the design can be scaled up to any width in practice, consisting of multiple side-by-side 12"-wide I-Lam panels. But the impact concentration area is considered as over the 72" wide protection of six side-by-side 12"-wide I-Lam panels when the truck impact takes place.

Table 6 Final design recommendation for different implementation cases

H ft. (m)	*L* ft. (m)	*m* lbs (10^3 kg)	Velocity mile/h (m/s)	The maximum force transferred, kips (x 10^3 N)	The maximum displacement transferred, in. (m)	Energy need to be absorbed (KJ)	Design recommendations
0.2 (0.061)	1.64 (0.5)	66.58 (0.0302)	24.85 (11.11)	108 (480)	0.748 (0.019)	0.87	72”X12”X8”
1.0 (0.305)	1.64 (0.5)	332.90 (0.151)	24.85 (11.11)	108 (480)	1.102 (0.028)	1.89	72”X12”X8”
0.2 (0.061)	50.03 (15.25)	2,028.25 (0.92)	24.85 (11.11)	710 (3.16E3)	9.370 (0.238)	26.57	72”X12”X10”
1.0 (0.305)	50.03 (15.25)	10,141.26 (4.6)	24.85 (11.11)	935 (4.16E3)	10.158 (0.258)	57.34	72”X12”X10”
0.2 (0.061)	1.64 (0.5)	66.58 (0.0302)	37.29 (16.67)	108 (480)	1.339 (0.034)	3.21	72”X12”X8”
1.0 (0.305)	1.64 (0.5)	332.90 (0.151)	37.29 (16.67)	108 (480)	2.283 (0.058)	13.55	72”X12”X8”
0.2 (0.061)	50.03 (15.25)	2,028.25 (0.92)	37.29 (16.67)	695 (3.09E3)	9.449 (0.240)	97.62	72”X12”X10”
1.0 (0.305)	**50.03 (15.25)**	**10,141.26 (4.6)**	**37.29 (16.67)**	890 (3.96E3)	10.039 (0.255)	**412.59**	72”X12”X24”
0.2 (0.061)	1.64 (0.5)	66.58 (0.0302)	49.70 (22.22)	108 (480)	1.890 (0.048)	6.46	72”X12”X8”
1.0 (0.305)	1.64 (0.5)	332.90 (0.151)	49.70 (22.22)	108 (480)	4.016 (0.102)	29.85	72”X12”X8”
0.2 (0.061)	**50.03 (15.25)**	**2,028.25 (0.92)**	**49.70 (22.22)**	679 (3.02E3)	9.252 (0.235)	**196.90**	72”X12”X10”
1.0 (0.305)	**50.03 (15.25)**	**10,141.26 (4.6)**	**49.70 (22.22)**	839 (3.73E3)	9.843 (0.250)	**909.02**	72”X12”X48”
0.2 (0.061)	1.64 (0.5)	66.58 (0.0302)	62.14 (27.78)	108 (480)	2.126 (0.054)	10.66	72”X12”X8”
1.0 (0.305)	1.64 (0.5)	332.90 (0.151)	62.14 (27.78)	108 (480)	2.638 (0.067)	50.84	72”X12”X8”
0.2 (0.061)	**50.03 (15.25)**	**2,028.25 (0.92)**	**62.14 (27.78)**	663 (2.95E3)	9.173 (0.233)	**324.78**	72”X12”X10”
1.0 (0.305)	**50.03 (15.25)**	**10,141.26 (4.6)**	**62.14 (27.78)**	832 (3.70E3)	9.921 (0.252)	**1548.42**	72”X12”X72”

From the given design listed in Table 6, the design capacity of the I-Lam with six pieces of 12 x 12 x 8 in. I-Lam (see Figures 12 and 13) can satisfy most of the crashing protection requirements, and it is chosen in this study as the final design dimension and shown in Figure 23. The I-Lam panels can be either adhesively bonded or bolted to the concrete girders. For additional safety precautions, two loose cables are attached to each I-Lam panel and concrete substrate (see Figure 23). In case the I-Lam is impacted off from the concrete girder, the loose cables can hold the I-Lam on the girder, thus avoiding that the I-Lam panels drop down to the beneath traffic lanes. The detailed design refers to Section 4.4.3. The original installation design details are given in Appendix A. The field installation and implementation of the I-Lam panels on a slab concrete bridge (DEL-23-12.99) in Delaware, Ohio are given later in Section 8. Based on the site condition requirements, the field installation details in Section 8 are slightly modified from the original installation design in Appendix A, in which the adhesive bonding is not involved in the field installation of I-Lam panels on the DEL-23-12.99 bridge.

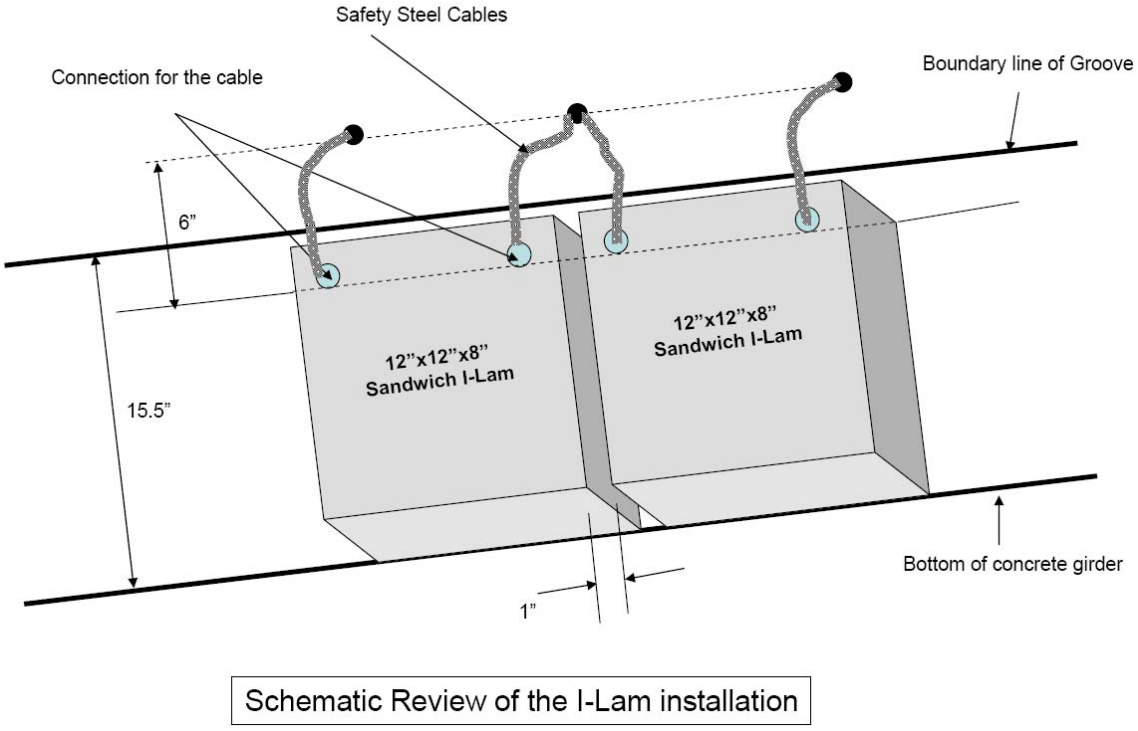

Figure 23 Final design of I-Lam systems for field implementation

4.7 Summary

Engineering design and analysis of the new I-Lam system is presented. First, a simplified linear elastic impact analysis of fully-backed I-Lam is provided, and three models (Models I to III for discrete system, under concentrated load and distributed load,

respectively) are presented to predict the contact force, displacement, and duration. The engineering equations for contact force, displacement and duration predictions are given, of which the shear-off mechanism of the overheight material is included (Section 4.1). Second, the three engineering design criteria (i.e., contact force limit design, contact deflection limit design, and energy absorption limit design) are proposed (Section 4.2). Third, to properly design the I-Lam protection system for overheight truck impact, the impact velocity and loading conditions are defined, and the suitable range for realistic overheight impact and shear-off are given (Section 4.3). Fourth, three design stages (i.e., elastic to elastic-plastic to densification) is provided to more accurately analyze and design the I-Lam protection system, and a final design (see Figures 12 and 13) based on the above criteria and procedures is given (Section 4.4). Then, the impact process of the plain and reinforced concrete beams with and without I-Lam protection is simulated using the commercial finite element software LS-DYNA, and it indicates that the concrete beams with I-Lam significantly reduce the magnitude of contact force, thus reducing the resulting deformation and damage in the concrete beams (Section 4.5). Finally, the design recommendations for the I-Lam system suitable for field implementation are summarized (Section 4.6). In summary, a thorough engineering design and analysis for I-Lam protection system is provided, and the analysis methodologies and design procedures could be used to design collision protection systems for highway structures.

5. EXPERIMENTAL PROGRAM

In this section, the experimental characterization of I-Lam/concrete interface, I-Lam core crushing, and I-Lam indentation are performed, and their applications in impact response analysis are discussed.

5.1 Evaluation of Bond between Collision Protection System and Concrete Beam

If the adhesive is used to bond the I-Lam with concrete girder, the bond strength along the interface between the I-Lam and concrete should be evaluated. A 3-point bend beam (3PBB) test (Qiao and Xu 2004) is adopted to evaluate the fracture and bond strength (fracture energy) of I-Lam and concrete interface (see Figures 24 and 25). The purpose of the 3PBB tests of I-Lam and concrete interface is to provide a general idea of the interface bond strength, which will guide the final installation design and prevent the premature failure in the collision protection system due to inadequate bond strength. The experimental setup is shown in Figures 24 and 25, and the specimen consists of bonding a concrete beam to an I-Lam block. To contour the specimen, an additional but short concrete beam is bonded to the other surface of the I-Lam, thus positioning the interface at the central span. High modulus, high strength, smooth, epoxy paste anchoring adhesive (Sikadur AnchorFix-3) from Sika Corporation is chosen as the adhesive, which has two components mixed through the mixer container. The interfaces with two different aluminum honeycomb core densities (i.e., 1/5” core – higher density and ¼” core – lower density) are tested, and their interface critical fracture loads and energies, two important factors indicating the interface strength, are reduced and compared.

Figure 24 Test setup of 3PBB with I-Lam and concrete interface

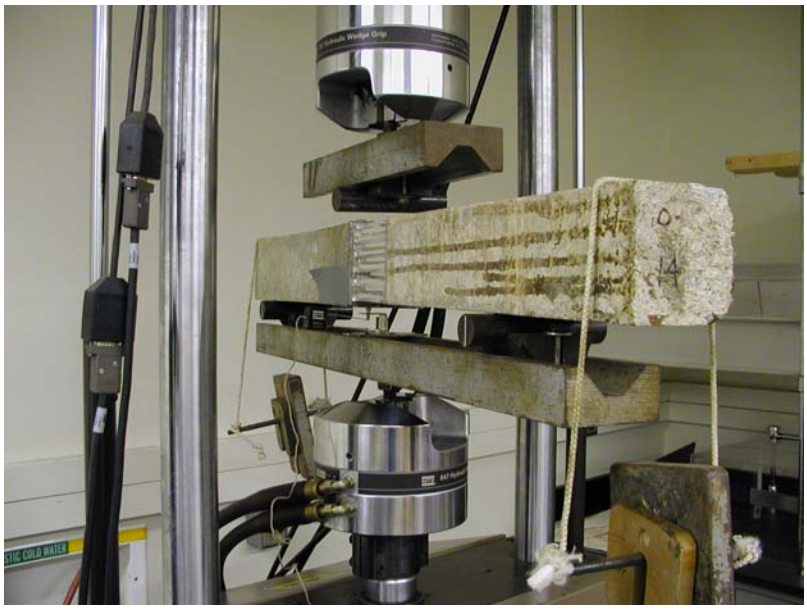

Figure 25 Side view of 3PBB test of I-Lam and concrete interface

5.1.1 Fracture surface characterization

A total of four samples (two for each density: higher or lower) are tested using the 3PBB test. The fractured surfaces of the interface between the I-lam and concrete substrate are shown in Figure 26, in which the fractures are developed mainly on the concrete sides for all the samples. The interface fractures mostly propagate in the rich resin layer, with two cases oscillating through the concrete side as well.


(1) Sample 1 (Higher density core)

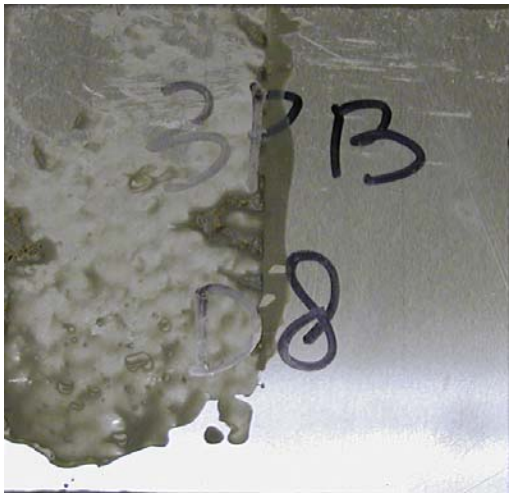


(2) Sample 2 (Higher density core)

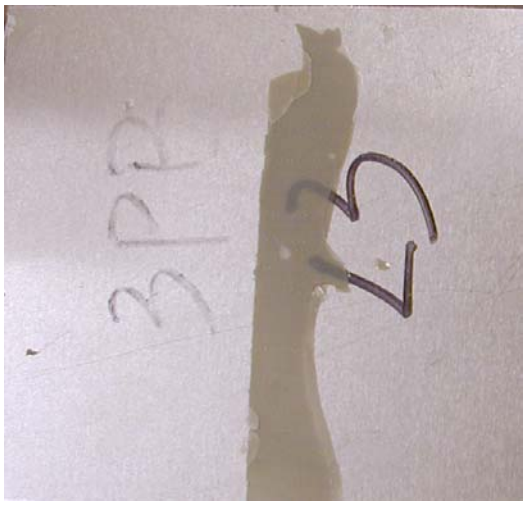
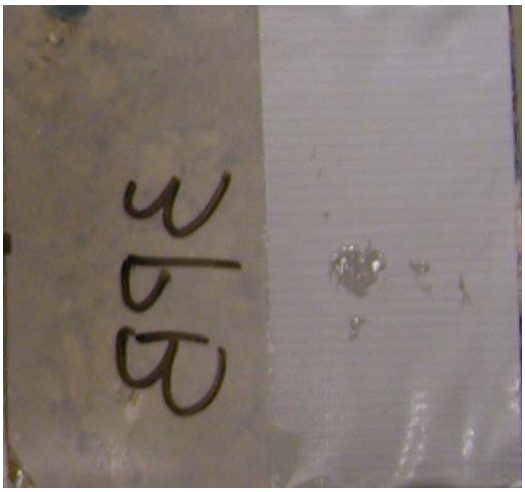

(3) Sample 3 (Lower density core)

(4) Sample 4 (Lower density core)

Figure 26 Fracture surfaces of I-Lam and concrete interfaces

5.1.2 Data reduction

From the experimental tests, the displacement and applied load are recorded through the MTS testing system and plotted in Figures 27 and 28, for the higher and lower core densities, respectively. From Figures 27 and 28, it indicates that the fracture of I-Lam and concrete interface mainly shows a brittle fracture with the critical peak values of 174.10 lb (780 N) and 14.51 lb (65 N) for the representative higher and lower density cores, respectively.

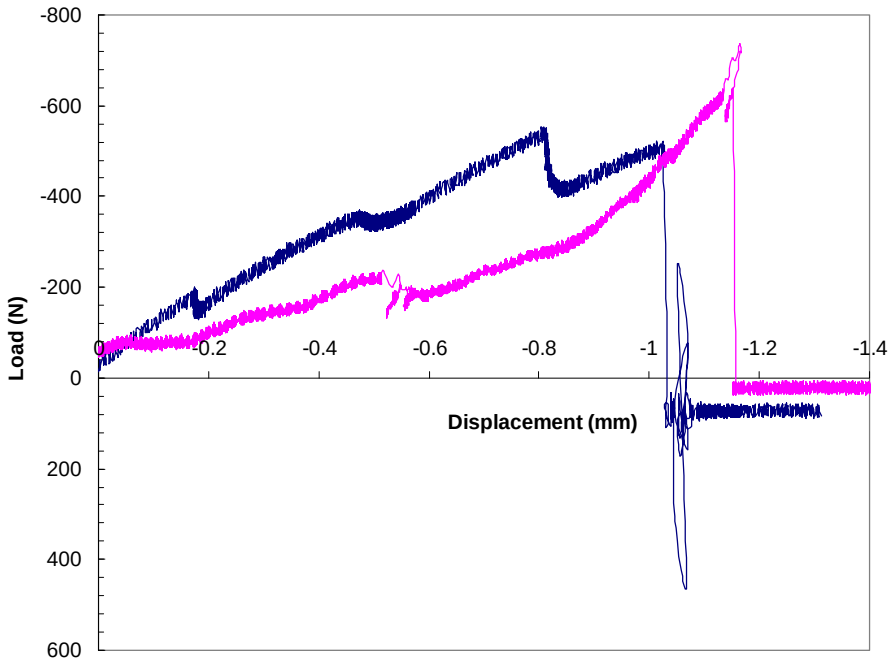

Figure 27 Load-displacement curve of higher density core I-Lam-concrete interface (Note: 1 N = 0.224 lb., 1 mm = 0.039 in.)

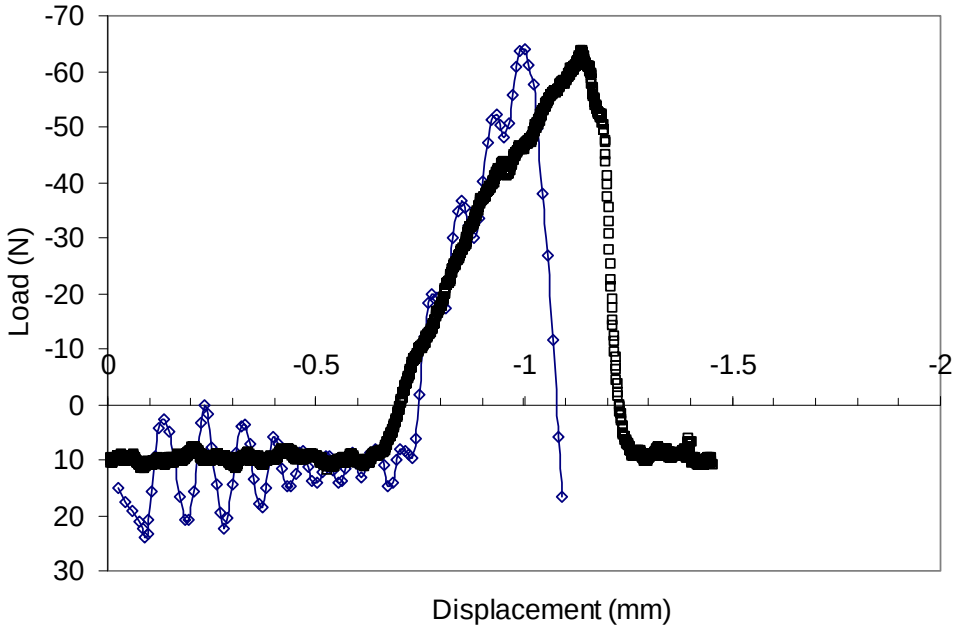

Figure 28 Load-displacement curve of lower density core I-Lam-concrete interface (Note: 1 N = 0.224 lb., 1 mm = 0.039 in.)

5.1.3 Fracture energy of I-Lam and concrete interface

From the recorded load-displacement curves (Figures 27 and 28), the fracture energies of the I-Lam and concrete interface are calculated. According to the fictitious crack model (Hillerborg 1985; Qiao and Xu 2004), the fracture energy is the one required to produce a unit area of crack (full broken). If a specimen is statically fractured and the work (W_F) applied to fracture the interface is measured, then the approximate interface fracture energy can be computed as

$$G_F = \frac{W_F}{t(b-a)} \tag{37}$$

where t is the specimen thickness; b is the height of the beam; a is the initial notch (crack) length; and $(b - a)$ is the initial ligament length of the interface. Based on the record data (Figures 27 and 28) and the procedures given in Qiao and Xu (2004), the fracture energies for the interfaces of I-Lam and concrete with the higher and lower core densities are given in Table 7.

Table 7 Fracture energy G_F and critical load P_{cr} of I-Lam and concrete bonded interfaces (Curing time: 24 hours)

Bond types	Low density sandwich-concrete interface		High density sandwich-concrete interface	
Loading Rate in/sec (mm/sec)	0.000394 (0.01)		0.000394 (0.01)	
Specimen	P_{cr} lbs (N)	G_F lbs/in (N/m)	P_{cr} lbs (N)	G_F lbs/in (N/m)
1	14.4 (64.2)	0.0228 (4.08)	176.7 (786.0)	0.511 (91.44)
2	14.2 (63.7)	0.0247 (4.42)	135.5 (602.7)	0.412 (73.83)
Avg.	14..3 (64.0)	0.0237 (4.25)	156.1 (694.4)	0.461 (82.64)

From Table 7, we could conclude that the fracture energy of the aluminum I-Lam-concrete interface depends on the material properties of the core material, and the higher density core produces larger interface fracture energy. It indicates that the deformation of the I-Lam sandwich is important in determining the interface energy or strength. Compared to the corresponding laminate-concrete interface (Qiao and Xu 2004), the aluminum sandwich concrete interface with the higher density core gives comparable interface fracture peak load and fracture energy. Also the load-displacement curve of lower density I-Lam/concrete interface shows more ductile behavior (Figure 28) than that of the higher density concrete interface, which affects fracture progress of the interface. Be aware that in the practice installation of the I-Lam structures, the high density side of the I-Lam is bonded to the concrete girder.

5.2 Behavior of I-Lam Core Crushing

In order to simulate the progressive crushing process and energy absorption capability of the honeycomb sandwich material, a series of I-Lam crushing tests are performed using the MTS machine and the ARAMIS system.

5.2.1 Crushing tests

To study the folding mechanism of the honeycomb materials, the ARAMIS system is employed to experimentally measure the deformation and strain fields during the crushing process. The ARAMIS system is a full field optical technique, which is increasingly appreciated as an effective deformation and strain measurement tool. The ARAMIS system employs 3D image correlation photogrammetry, and the test processes involve sample preparation, setup calibration, and data reduction. The sample preparation consists of applying a regular or random high contrast dot patterns to the surface, commonly with spray paint. Thousands of unique correlation areas known as facets (typically 15 x 13 pixels) are defined across the entire imaging area. Each facet can be thought of as an extensometer. Through tracing the movement of facets, the full strain field can be measured directly. The

test setup of the specimen in the Materials Testing System (MTS) with the ARAMIS system is shown in Figure 29.

5.2.2 Honeycomb materials

In the honeycomb core crush tests, three honeycomb aluminum materials are investigated, and the honeycomb core is in hexagonal configuration. The honeycomb aluminum materials include: (1) 1/5 in. (5.08 mm) cell size core (high density); (2) ¼ in. (6.35 mm) cell size core (low density); and (3) two-layer honeycomb core consisting of 1/5 in. (5.08 mm) and ¼ in. (6.35 mm) cell size cores. The wall thickness of the hexagonal walls is about 0.003 in. (0.0762 mm). The honeycomb materials are fabricated and provided by Plascore Inc., Zeeland, MI.

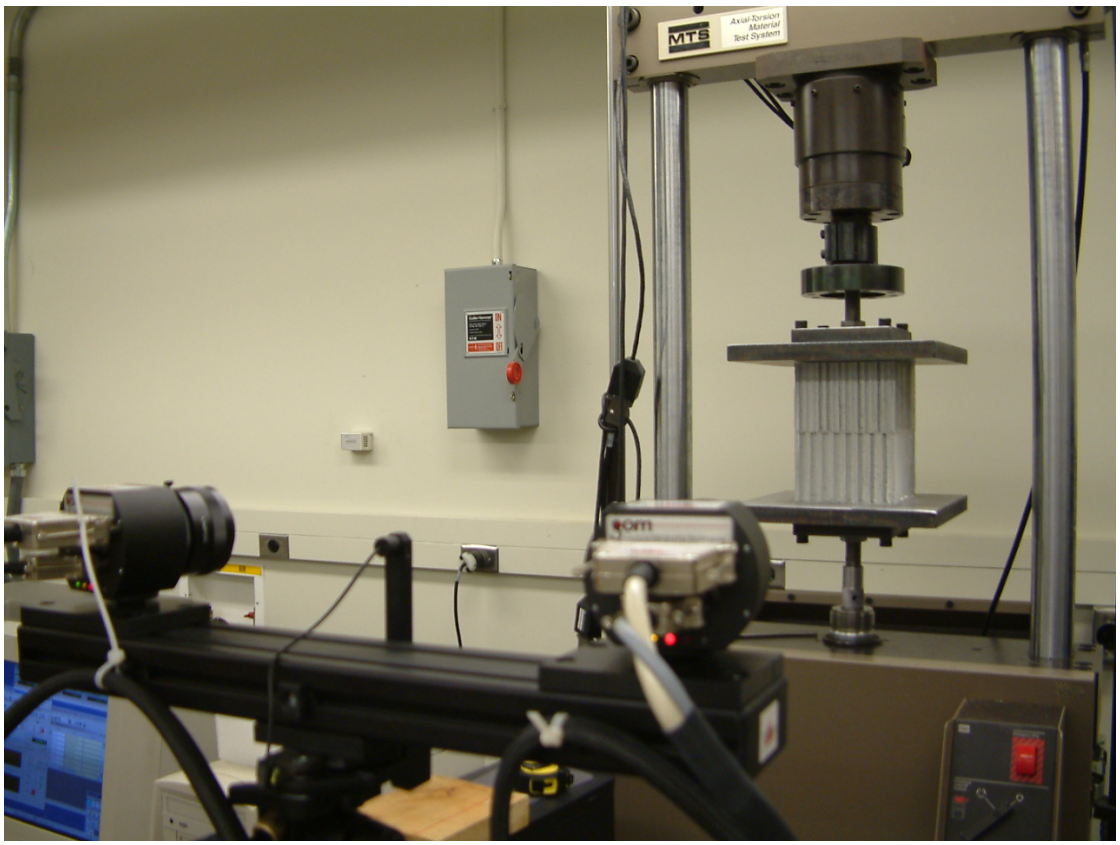

Figure 29 ARAMIS system and specimen setup on the MTS

5.2.3 Experimental characterization

Understanding the mechanical response of cellular materials is a key to design of ultra-light and high energy absorbing structures. Physical experiments, theoretical investigations, and numerical simulations provide the insight of the nucleation and propagation of plastic collapse bands in aluminum honeycomb under impact conditions. For the honeycomb core compressed in the axial direction, the localization occurs in the well

defined plastic collapse bands at the interface between the crushed and uncrushed regions. Globally, a flat crushing front propagating in the specimen is observed in the experiment.

The physical specimens are in a configuration of a 6 in. (152.4 mm) by 6 in. (152.4 mm) cross-section and a height of 4 in. (101.6 mm) for the 1/5 in. (5.08 mm) and 1/4 in. (6.35 mm) cores and of 8 in. (203.2 mm) for the two-layer core. The test setup is shown in Figure 29. Each specimen is placed between two 1 in. (25.4 mm) thick parallel steel plates and compressed by a hydraulic servo-controlled MTS machine. The test is conducted using the displacement control with four different rates of piston V_p = 0.2 in./mm (5 mm/min), 0.4 in./mm (10 mm/min), 0.8 in./mm (20 mm/min), and 1.2 in./min (30 mm/min), and the specimen is unloaded at every 0.6 in. (15 mm) or 0.8 in. (20 mm) with the displacement rate of V_p = - 0.04 in./min (-1 mm/min, where V_p is the loading velocity of the piston).

During the compressive crushing tests of honeycomb aluminum, two distinct configurations related to the crushed and uncrushed regions are developed. The transformation of uncrushed to crushed regions is characterized by the progressive folding of the honeycomb structure. About 24 and 36 folds are developed in the honeycomb materials with the 1/4 in. (6.35 mm) and 1/5 in. (5.08 mm) cores, respectively (Figure 30), and the lengths of folding are very close to the cell sizes of the two materials. The interface position is determined from the specimen photo images (Figure 31) at every 0.6 in. (15 mm) or 0.8 in. (20 mm) of the crosshead motion of the piston, and it reveals clearly a linear function of core crushed front with respect to the crosshead displacement (Figure 32). From Figure 32, the compaction index is computed, and they are 1.16 and 1.22, respectively, for the 1/4 in. (6.35 mm) and 1/5 in. (5.08 mm) cell size materials.

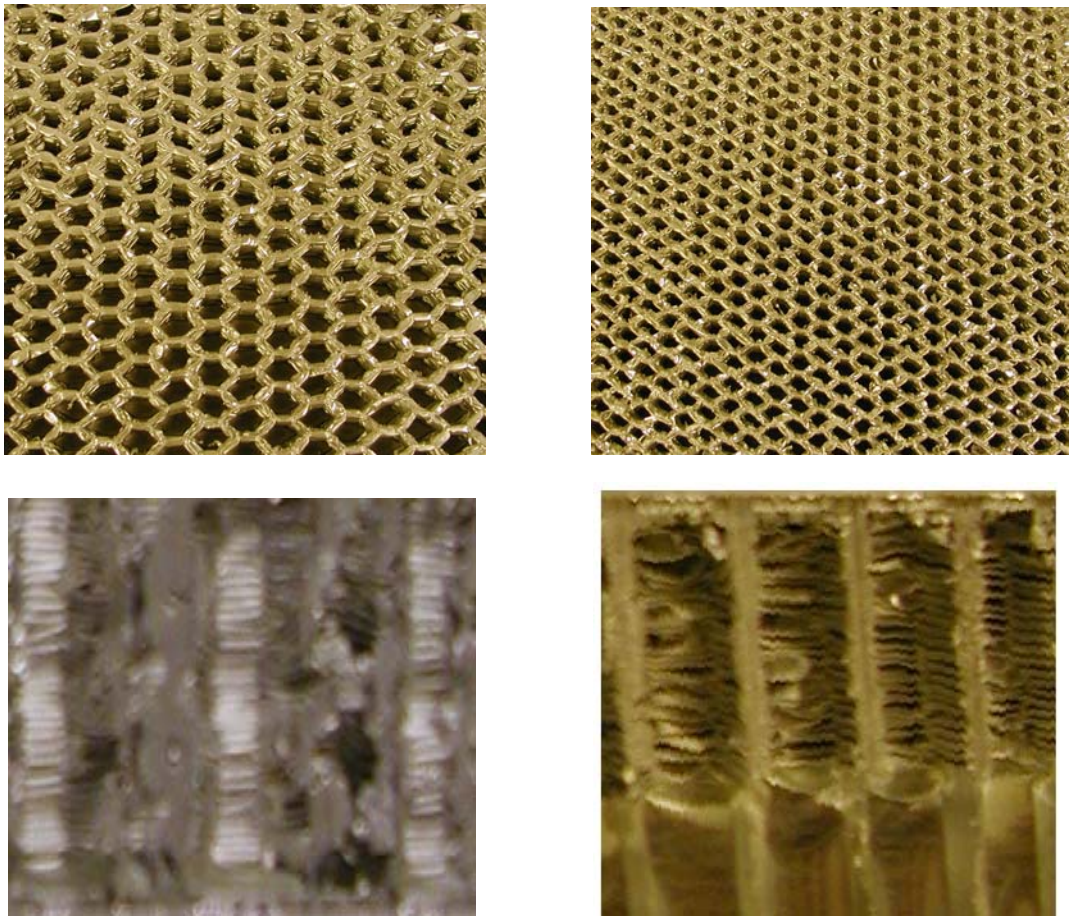

(a) 1/5 in. (5.08 mm) core (b) 1/4 in. (6.35 mm) core

Figure 30 Folding patterns in the aluminum materials with two difference core sizes

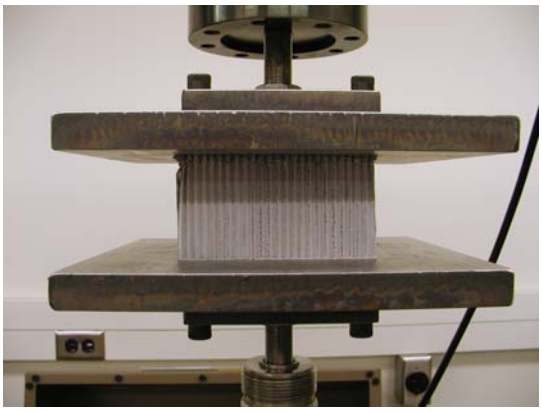

(a) Stage 1

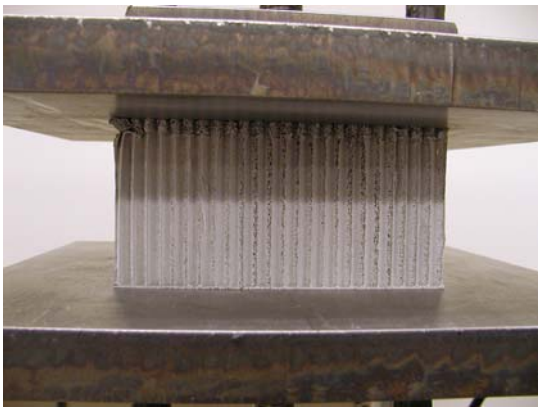

(b) Stage 2

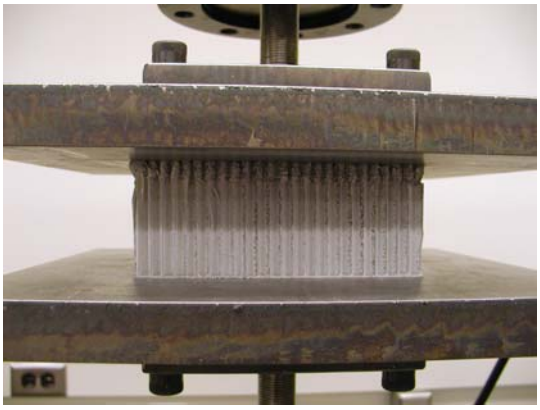

(c) Stage 3

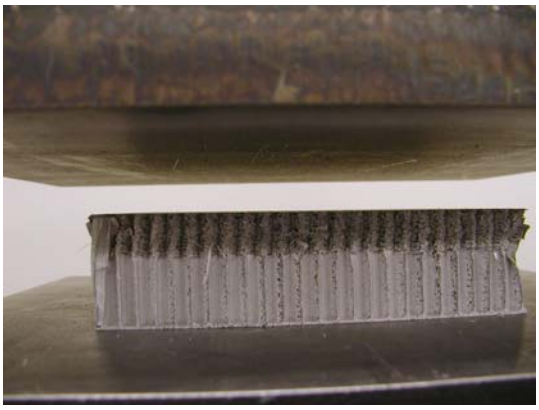

(d) Stage 4

Figure 31 Four different stages of the core crushed front with the displacement rate of 0.2 in./mm (5 mm/min, the core cell size is 6.35 mm)

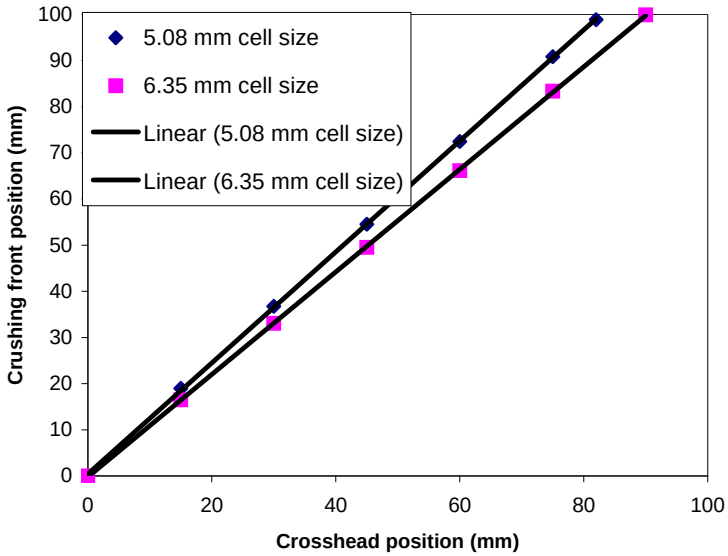

Figure 32 Experimental observation of the core crushed front interface (Note: 1 mm = 0.04 in.)

5.2.4 Load-displacement curve

Even though the microscopic analysis shows that the material loses homogeneity in the micro structures due to deformation localization, the macro responses still indicate the statistical homogeneity in terms of the compression responses and the repetition of the test results in different specimens with varying degrees of imperfection. Due to the special structures of honeycomb materials (deformation localization), the local defections or imperfection cannot propagate too far, and they are limited to several cell sizes. Thus, changing of local failure modes does not affect the macro responses pronouncedly.

Based on the uniaxial compression (crushing) experiments performed on aluminum honeycombs, the macro constitutive properties are obtained. A representative load-displacement curve for the three type structures is shown in Figure 33. Due to very limited cross sectional expansion or contraction observed when compressed in the axial direction, the macroscopic stress (σ) is defined as the axial compression load per unit specimen cross-sectional area. As shown in Figure 33, the force or stress increases monotonically to an initial peak. As the loading continues, the force or stress drops a little, and it then reaches a long plateau regime. During the progressive crushing in which a core folding mechanics is involved, the stress fluctuates around a constant value of about 118.93 psi (0.82 MPa) and 237.86 psi (1.64 MPa) for 1/4 in. (6.35 mm) and 1/5 in. (5.08 mm) cores, respectively; while their corresponding energy absorption capacity for the two materials for a 6 x 6 x 4 in. block is about 2.10 KJ and 4.13 KJ, respectively. The initial peak stress can be viewed as the nucleation threshold of collapse bands; while the subsequent lower peaks are the growth thresholds for the crushed regions. After the bands have covered the entire specimen, which is about 75 - 90% of the original height, the stress increases steeply, and the transition to the densification regime occurs.

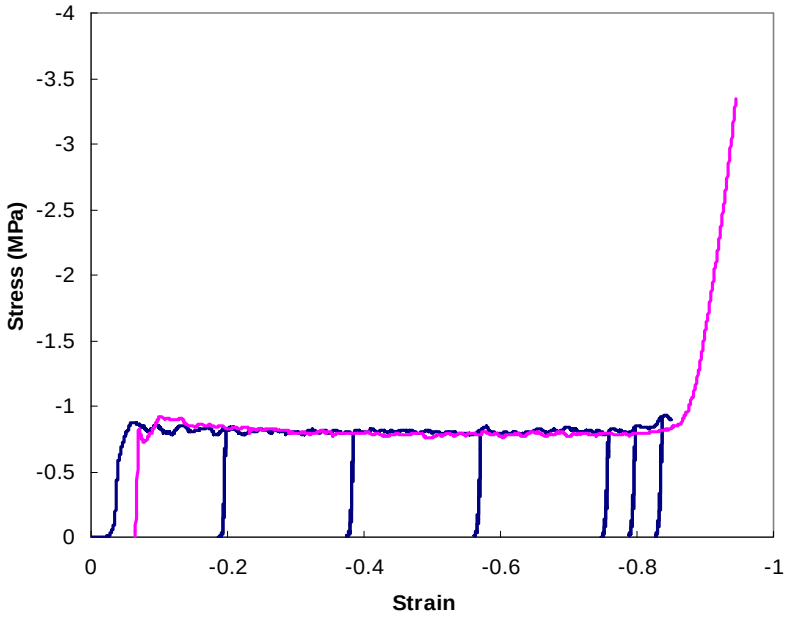

(a) 1/4 in (6.35 mm) cell core

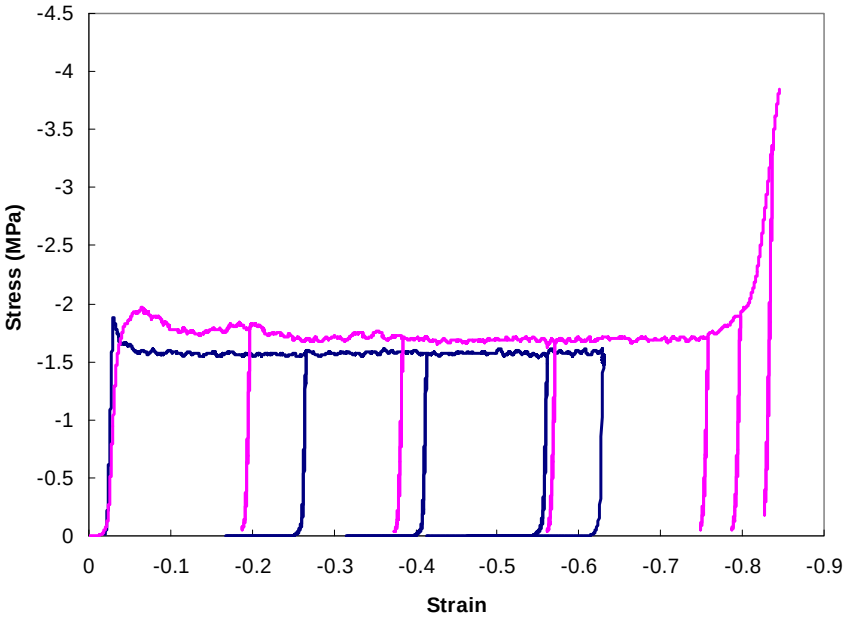

(b) 1/5 in (5.08 mm) cell core

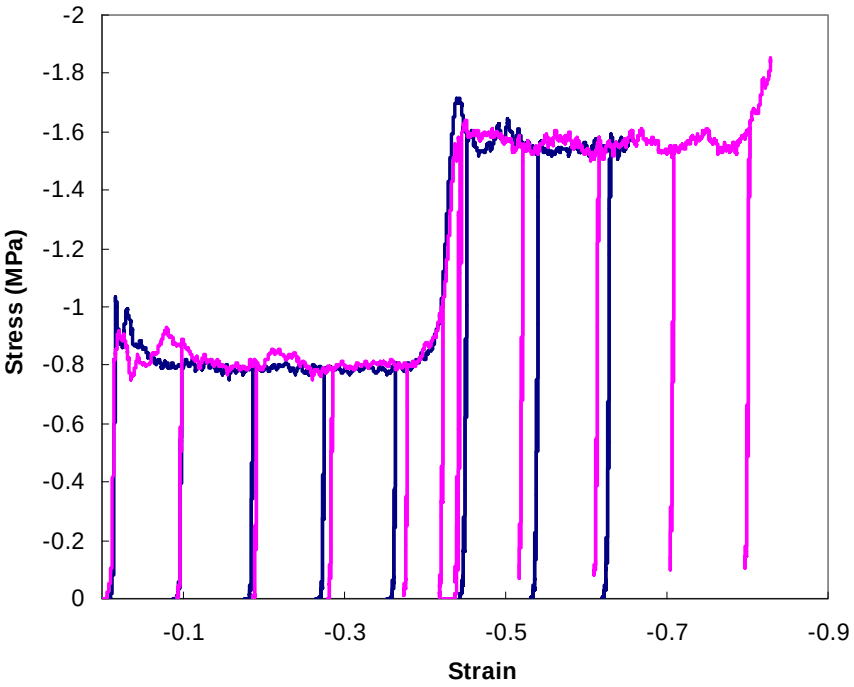

(c) Two-layer core

Figure 33 Load-displacement curves and densification locations for the loose (1/4 in. (6.35 mm)), dense (1/5 in. (5.08 mm)) and two-layer materials at displacement rate of 0.2 in./mm (5 mm/min) (Note: 1 MPa = 145.0 psi)

5.2.5 Strain rate effect

Four different strain rates (i.e., V_p = 0.2 in./mm (5 mm/min), 0.4 in./mm (10 mm/min), 0.8 in./mm (20 mm/min), and 1.2 in./ min (30 mm/min) are employed in the tests, and the results are shown in Figure 34. From the quasi-static tests, it is noted that the effect of the strain rate on the crushing force is relatively small. The multilayer configuration affects the crushing stress a little bit; however, the effect is not significant, which leads to the applicability of simple superposition of absorbed energy.

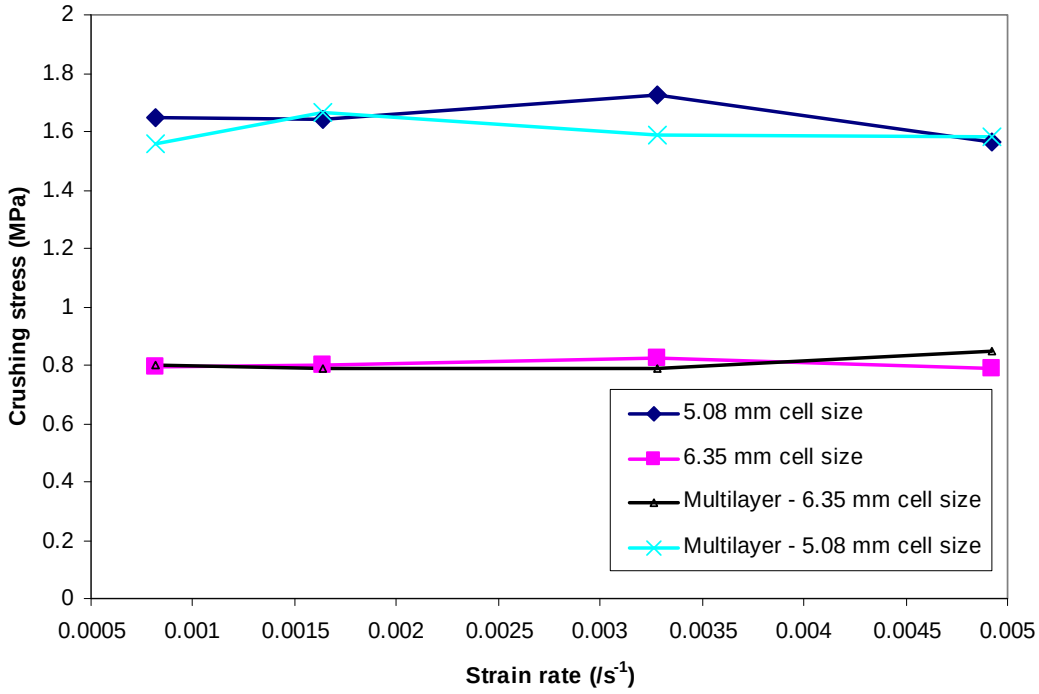

Figure 34 Strain rate effect on the crushing forces (Note: 1 MPa = 145 psi)

5.2.6 Stiffness change during the crushing process

From the quasi-static tests, the compliance or stiffness of the honeycomb materials with respect to the crushing process is analyzed. In Figure 35, it is observed that the stiffness increases from the starting position to the peak due to the imperfection of the structure and the settlement of the piston during the loading. When the stress rises to the global yielding stresses, the stiffness begins to decrease until the specimen reaches to the densification point. A one dimensional theoretical explanation of the phenomenon shown in Figure 35 can be found in Mohr and Doyoyo (2003).

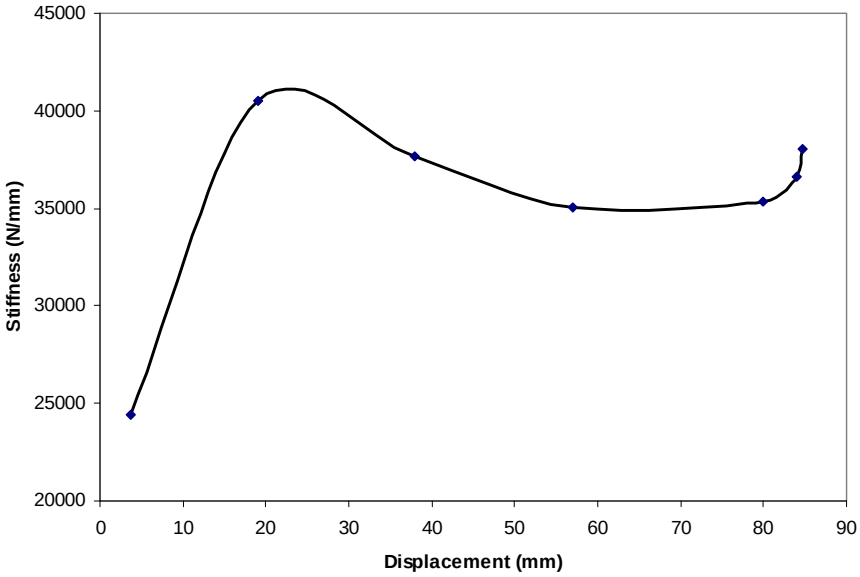

(a) 1/4 in. (6.35 mm) cell size core

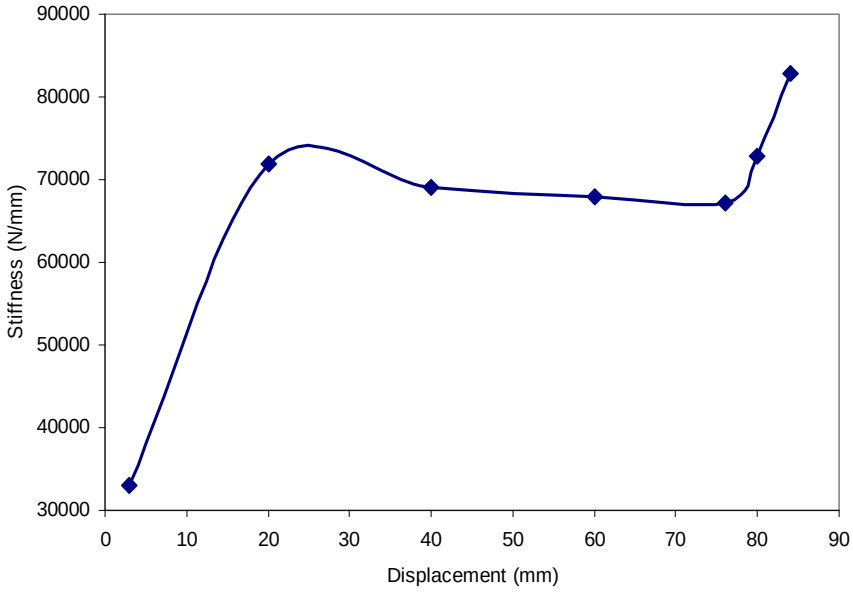

(b) 1/5 in. (5.08 mm) cell size core

Figure 35 Change of stiffness during the crushing process at displacement rate of 0.2 in./min (5 mm/min) (Note: 1 N = 0.224 lb, 1 mm = 0.04 in.)

5.3 Partial Crushing Test

In the previous sections, the crushing behavior of honeycomb materials compressed between two rigid steel plates is studied. However, in the practical application, a more realistic situation is the honeycomb material/sandwich under partial loading. In this section, the partial crushing behavior of the three honeycomb materials is experimentally

characterized.

5.3.1 Test setup

The size of the indenter has a pronounced effect over the crushing process. Choosing a one-inch diameter cylinder indenter, a series of partial crushing tests over sandwich beams are conducted using the MTS and ARAMIS systems with the strain rate of 0.2 in/min (5 mm/min) (Figure 36). At least two samples per honeycomb materials are tested. The deformation captured by the ARAMIS system is shown in Figure 37, from which a sharp local deformed region is formed under the indenter.

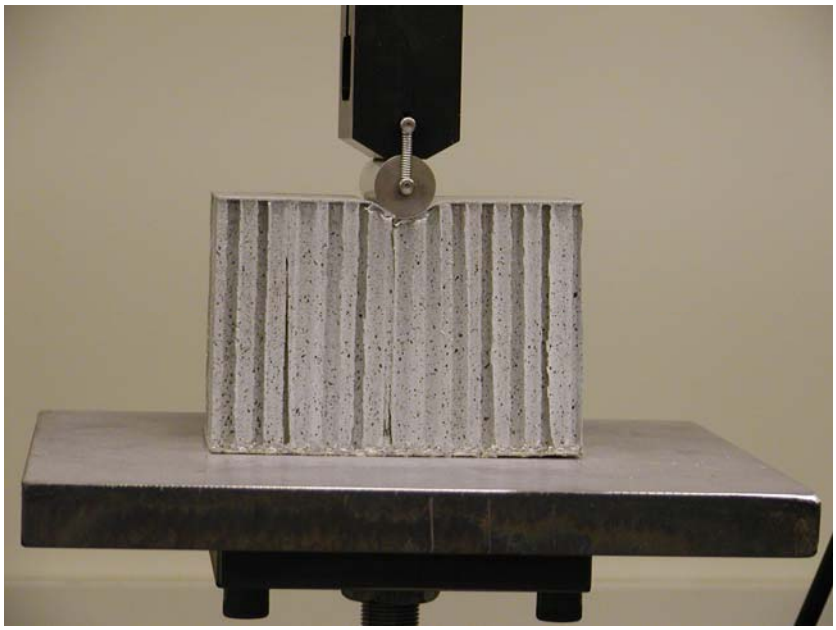

Figure 36 Test setup of partial crushing

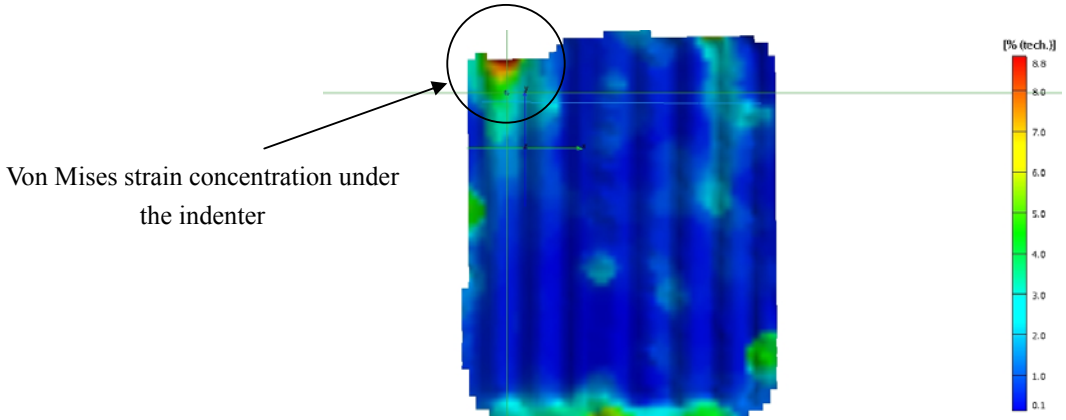

Figure 37 Von Mises strain distribution from ARAMIS system at the displacement of intender of 0.08 in. (2.0 mm)

5.3.2 Data reduction and discussions

The test data recorded from MTS are analyzed, and the results are shown in Figures 38 to 41. From all the tests, it is interesting to observe that the partial crushing behavior of the honeycomb aluminum shows a plastic hardening behavior. For the ¼ in. (6.35 mm) cell size material, the stiffness changes from 8,943.02 psi (61.66 MPa) to 1,003.40 psi (6.92 MPa) (Figure 38); while for the 1/5 in. (5.08 mm) cell size material, the stiffness changes from 46,559.50 psi (321.10 MPa) to 1,744.35 psi (12.03 MPa) (Figure 39). It is also interesting to observe that when the material of 1/5 in. (5.08 mm) cell size is compressed under the indenter (is directly in contact with the indenter) but with the material of ¼ in. (6.35 mm) cell size as a substrate, the post-buckling behavior in the two-layer honeycomb is observed in Figure 41.

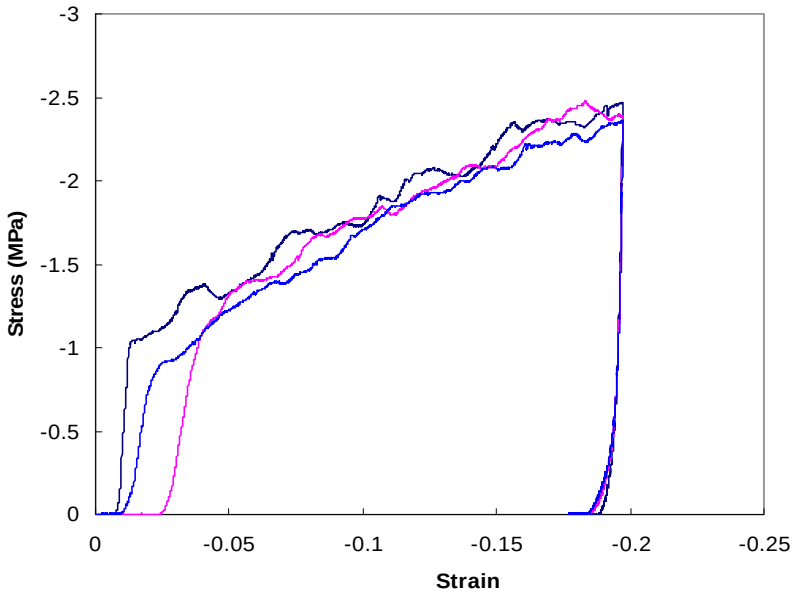

Figure 38 Load-displacement response of the sandwich beam with ¼ in. (6.35 mm) cell size honeycomb core under one-inch diameter cylindrical indenter (Note: 1 MPa = 145 psi)

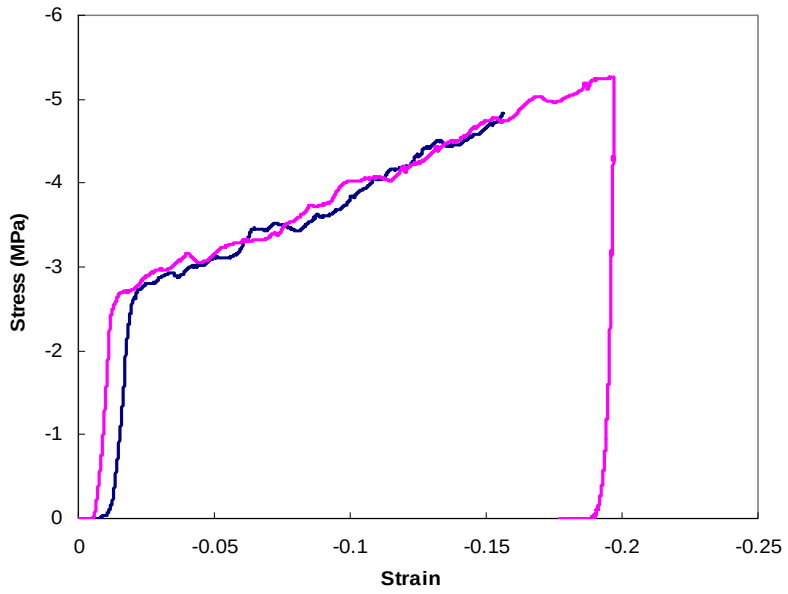

Figure 39 Load-displacement response of the sandwich beam with 1/5 in. (5.08 mm) cell size honeycomb core under one-inch diameter cylindrical indenter (Note: 1 MPa = 145 psi)

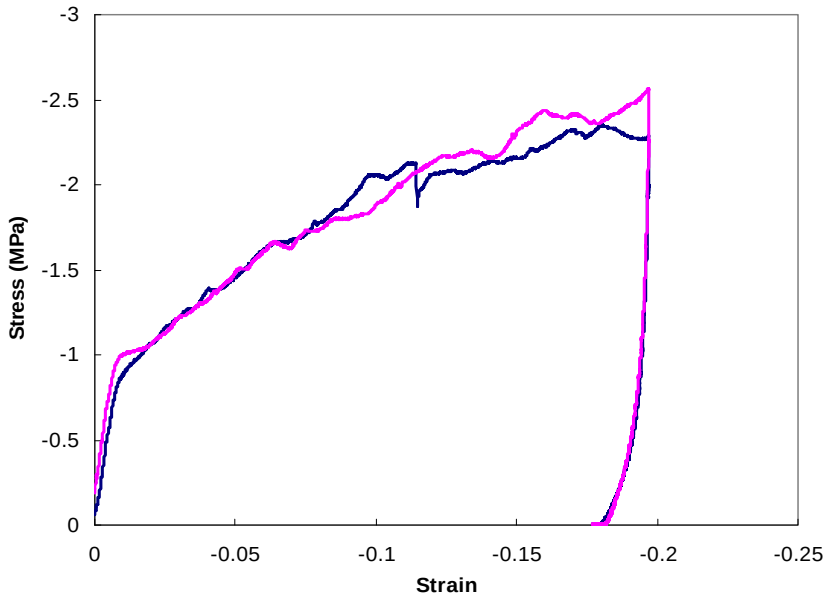

Figure 40 Load-displacement response of multilayer sandwich beam indented on the ¼ in. (6.35 mm) cell size core under one-inch diameter cylindrical indenter (Note: 1 MPa = 145 psi)

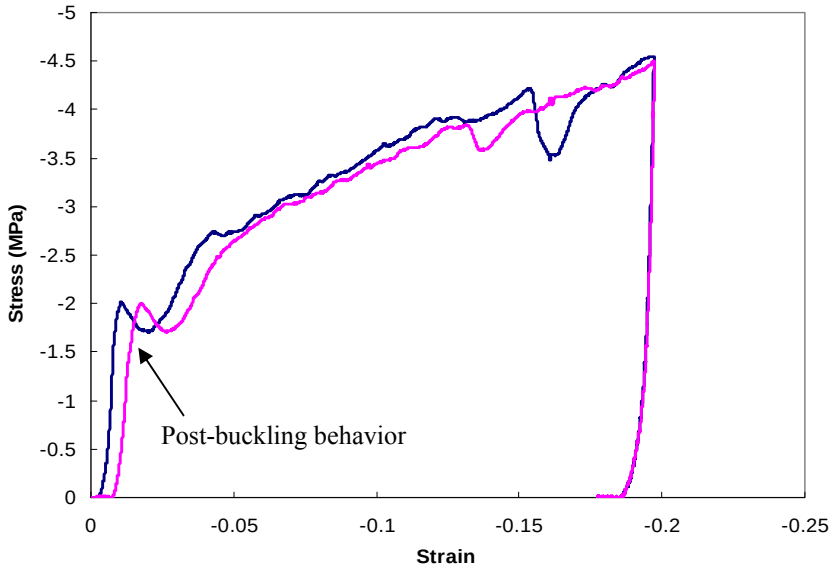

Figure 41 Load-displacement response of multilayer sandwich beam indented on the 1/5 in. (5.08 mm) cell size core under one-inch diameter cylindrical indenter (Note: 1 MPa = 145 psi)

5.4 Indentation Tests

In a similar fashion to the partial crushing tests, a series of indentation tests are also conducted on the MTS machine (Figure 42), from which the contact law for impact design is obtained. Two types of indenters (i.e., spherical and square shapes) are used to characterize the effects of different contact manners.

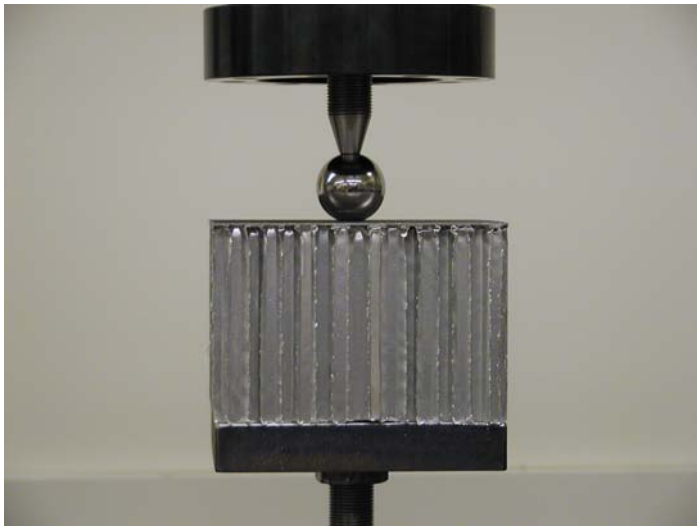

(a) Sphere indenter

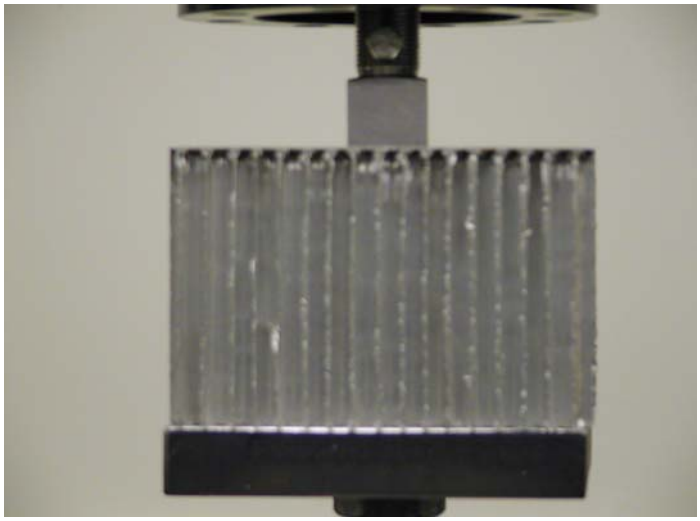

(b) Square indenter

Figure 42 Indentation tests

5.4.1 Contact law and its implementation in design

Observing the load-displacement curves derived for the indentation tests in Figures 43 and 44, the two types of indentation curves are simplified into a generalized curve as shown in Figure 45.

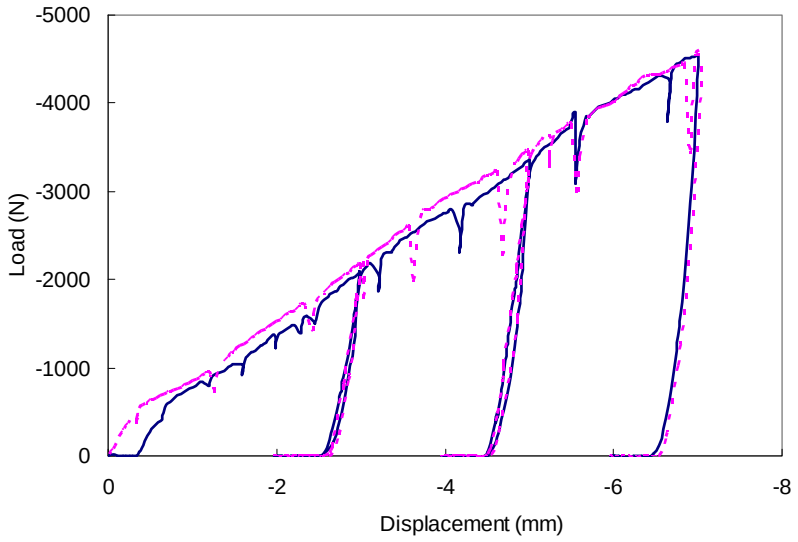

Figure 43 Load indentation curve of the higher density aluminum honeycomb sandwich indented by a 1.5 in. sphere indenter

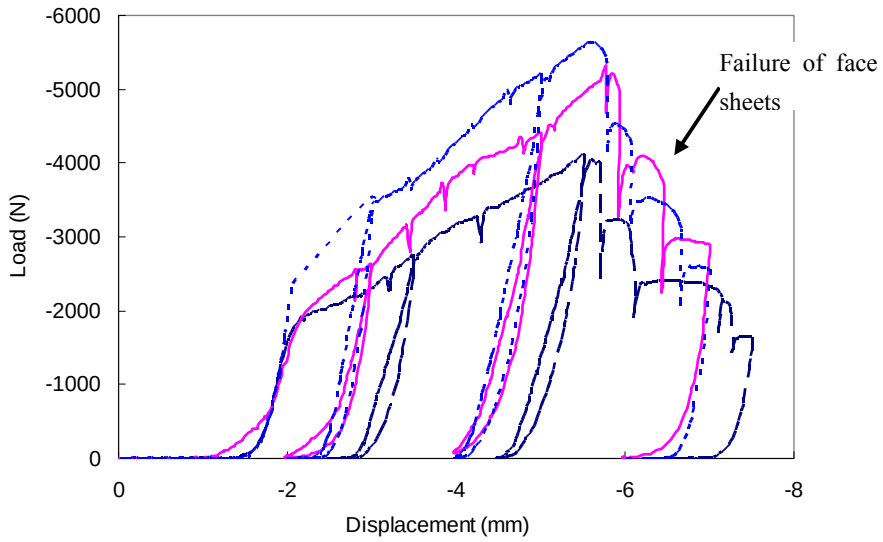

Figure 44 Load indentation curve of the higher density aluminum honeycomb sandwich indented by a 1.0 in. flat square indenter

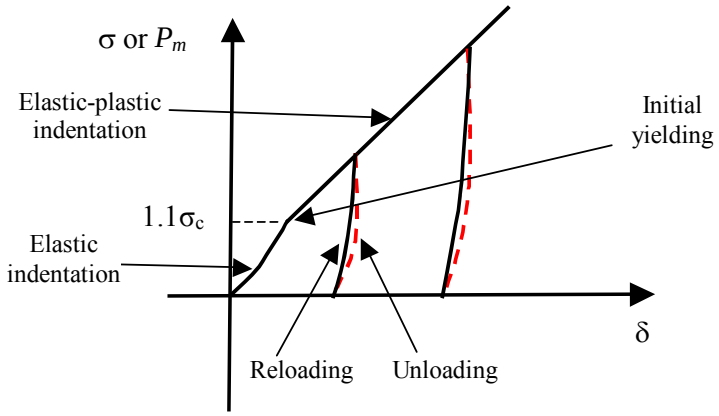

Figure 45 Generalized description of indentation behavior of a rigid supported aluminum honeycomb sandwich

From Figure 45, it is observed that the first loading phase to $1.1\sigma_c$ (initial yielding, Gibson and Ashby (1988)) can be used to determine the contact stiffness and the contact law for elastic contact region. The second loading phase from $1.1\sigma_c$ to $3.0\sigma_c$ (fully plastic state around the indenter, Gibson and Ashby (1988)) can be used to capture the load-indentation behavior in the elastic-plastic region. The unloading and reloading process in the plastic indentation region can be used to capture the loading and unloading behavior with plastic permanent deformation. Inversely, if the properties of the material tested are not previously known, the load-indentation curves can be used to get the corresponding material and

mechanical properties. In fact, most of the indentation experiments, especially nano-indentation experiments, belong to the later category.

Using different shapes and sizes of indenters, the contact stiffness and contact law of the rigid supported aluminum honeycomb sandwich are first analyzed. The classical contact law between an elastic sphere and an elastic half-space was first derived by Hertz in 1929 (Johnson 1985) and used in tribology and impact analysis (Tan and Sun 1995). Willis (1966) extended Hertz's solution and derived the explicit formulas for contact of a rigid sphere and a transversely isotropic half-space. Sneddon (1948) also found that the load-indentation depth function for an ideally elastic material under general arbitrary indenters could be described in both the loading and unloading periods by the same equation as

$$P = k\delta^2 \tag{38}$$

where P is the indentation load; k is the contact stiffness; and δ is the deflection or displacement at the indentation point.

In this report, considering the inherent layered structure of the I-Lam sandwich and without differentiating the material compression and indentation displacement, the relation of the load displacement curve for an indenter could be expressed as the modified Hertz's law by fitting the elastic load-displacement curve as

$$F = K\delta^n \tag{39}$$

and the elastic-plastic load-displacement curve in the elastic-plastic region can be fitted into the following loading ranges

$$F = \begin{cases} K_h\delta^n & Elastic-Loading & 0 \le \delta \le \delta_y \\ K_y(\delta-\delta_y)+K_h\delta^n & Elastic-Plastic-Loading & \delta_y \le \delta \le \delta_m \\ K_u(\delta-\delta_r)^n & Unloading & \delta_r \le \delta \le \delta_m \\ K_r(\delta-\delta_r) & \mathrm{Re}loading & \delta_r \le \delta \le \delta_m \end{cases} \tag{40}$$

where δ is the displacement at the indentation point; δ_y is the displacement at the indentation point when the core begins yielding; δ_r is the residual or permanent displacement at the indentation point when the sandwich is fully unloaded; δ_m is the maximum history displacement at the indentation point.

It should be pointed out that the load indentation curve is proposed based on the experimental curves, which capture the main contact process assuming that each unloading process must be completed before reloading can take place.

5.4.2 Modified Hertz's contact law in the elastic contact region

The 6"x6" I-Lam panels were tested in the MTS, and the load vs. displacement curves for all the tests under the elastic contain region and corresponding fitting results are given in Appendix B. Based on the fitting results (see Appendix B), the contact stiffness and power index for different materials are summarized in Table 8.

Table 8 Different contact stiffness and *n* for each combination of indenter and sandwich

Types	Flat-indenter (n/*K*)	Ball-indenter (n/*K*)	1-in-Flat-indenter (n/*K*)	1-in-ball-indenter (n/*K*)
SL-L	1.658/2793.90	1.3468/313.50	1.457/1974.36	1.0489/286.66
SL-D	1.5153/13719.8	1.9891/4448.4	1.337/6055.37	1.4446/4934.96

The multilayer sandwich indented by a 1.5 in. flat square indenter can be described using the same indentation law with n = 2.0426 and K = 1923.50 for indentation over the lower density honeycomb sandwich, and n = 2.0367 and K = 19141.23 for indentation over the higher density honeycomb sandwich.

From Table 8, it is noted that the lower density honeycomb sandwich gives a lower contact stiffness, and the power indices for all the materials are close to 1.5 with high correlation coefficients. For the larger indenters, both a larger power index and a larger contact stiffness are observed compared to the ones with smaller indenters. For the effects of different shapes of indenters, the flat indenters usually produce a higher contact stiffness with little variation of power indices.

The data in Appendix B show that the experiments indicate a strong linear relation after the initial yielding. Thus, the load indentation curve after the initial yielding can be approximated as the linear relation given in Eq. (40) as

$$F = K_y(\delta - \delta_y) + K_h\delta^n \quad \text{with} \quad \delta_y = \frac{\sigma_c h}{E_c}. \tag{41}$$

By equaling the slope of the elastic-plastic loading phase K_y to the slope of the elastic indentation curve at $\delta = \delta_y$, the contact stiffness is obtained as,

$$K_y = 1.5K_h\sqrt{\delta_y} \quad \text{if } n = 3/2 \tag{42}$$

where E_c is the Young's Modulus of the core material; h is the core height.

5.4.3 Loading and unloading effect

For the loading paths in the plastic region, the material is either in plastic flow or in plastic hardening, which changes the contact behavior of the materials. Therefore, different loading and unloading load displacement curves (see Appendix C) are measured during the process of the testing, and the corresponding contact stiffness and power indices are summarized in Table 9.

For the multilayer cases indented by the 1.5 in. square flat indenter, the corresponding power index and stiffness could be summarized as n = 1.5305 and K = 1720.38 for unloading and n = 1.3303 and K = 2442.56 for reloading when indented on the lower density side; n = 1.5724 and K = 9626.74 for unloading and n = 1.1442 and K = 9354.38 for reloading when indented on the higher density core side.

Table 9 Contact stiffness and *n* of the elastic-plastic loading and unloading for each combination of indenter and materials

Types	Flat-indenter (n/K)	Ball-indenter (n/K)	1-in-Flat-indenter (n/K)	1-in-ball-indenter (n/K)
SL-L	1.456/3572.43 1.000/4238.65	1.5337/985.06 1.2564/1175.32	2.4002/5016.56 1.5012/2701.06	2.001/866.71 1.3954/1609.70
SL-D	2.0502/15241.85 1.5225/12997.34	1.4765/6947.94 0.9815/4643.85	2.6517/15713.89 1.9208/11877.50	1.9261/14190.10 1.0988/5427.32

Even though the variation of data is observed in the test data, the proposed contact indentation law is good at capturing the indentation relation. It is noted that the flat square indenters cause a large contact stiffness compared to the sphere indenters. Increasing the diameters of sphere indenters or the side lengths of flat square indenters also increases their contact stiffnesses and power indices. Including the second layer of the sandwich material slightly decreases the contact stiffness and power index. However, the proposed indentation law still gives a good estimation about the load vs. indentation relations. In this study, the 1.5 in. sphere indenter is chosen as the representative indenter, and the corresponding contact parameters are given as Table 10.

Table 10 Contact stiffness of two different sandwich materials under the 1.5'' sphere indenter

Types	Elastic loading, lbs/in$^{2/3}$ (N/m$^{2/3}$)	Plastic unloading, lbs/in$^{2/3}$ (N/m$^{2/3}$)	Plastic reloading, lbs/in (N/m)
SL-L	1.88E+05 (9.91E+06)	5.91E+05 (3.11E+07)	6.59E+03 (1.18E+06)
SL-D	2.68E+06 (1.41E+08)	4.14E+06 (2.18E+08)	2.59E+04 (4.63E+06)

The parameters for the bi-layer I-Lam sandwich (Figures 12 and 13) indented by the 1.5'' square flat indenter are presented in Table 11.

Table 11 Various contact stiffness for indentation over the two layer sandwich materials

Types	Elastic loading, lbs/in$^{2/3}$ (N/m$^{2/3}$)	Unloading in plastic region, lbs/in$^{2/3}$ (N/m$^{2/3}$)	Reloading in plastic region, lbs/in (N/m)
SL-L	1.16E+06 (6.08E+07)	1.04E+06 (5.46E+07)	1.36E+04 (2.44E+06)
SL-D	1.15E+06 (6.05E+08)	5.78E+06 (3.04E+08)	5.22E+05 (9.35E+06)

5.5 Impact Responses of I-Lam

Considering the projectile as a free body and neglecting the mass effect of the face sheet, the dynamic equation of the projectile is expressed as

$$M\ddot{w}(t) = -P \tag{43}$$

Eq. (43) describes a rigid sphere impact of an elastic-plastic sandwich supported by a rigid substrate (fully-backed case), and it is subjected to the following boundary and initial conditions,

$$w(0) = 0\,,\quad \dot{w}(0) = V_0\,,\quad \delta = w \tag{44}$$

P is described as,

$$P = \begin{cases} K_h\delta^n & Elastic-Loading & 0 \le \delta \le \delta_y \\ K_y(\delta-\delta_y) + K_h\delta^n & Elastic-Plastic-Loading & \delta_y \le \delta \le \delta_m \\ K_u(\delta-\delta_r)^n & Unloading & \delta_r \le \delta \le \delta_m \\ K_r(\delta-\delta_r) & \mathrm{Re}\,loading & \delta_r \le \delta \le \delta_m \end{cases} \tag{45}$$

with

$$\delta_r = \delta_m - \delta_e \tag{46}$$

$$\delta_e = \frac{P_m}{K_r} \tag{47}$$

By incorporating the contact law given in Eq. (45), the impact problem can be solved by decomposing the above equations into several differential equations (Yigit and Christoforou 1995), and the residual deformation, absorbed energy, and contact force time history can be derived (Yang 2006).

5.5.1 Case study of a single layer sandwich panel

A case simulating the single layer fully-backed I-Lam beam under impact of a mass of 6.62 lbs (3 kg) with an initial velocity of 7.62 miles/hour (3 m/s) is conducted and compared with the LS-DYNA results. The residual deformation, contact force, residual velocity and force-indentation behavior are shown in Figures 46 to 49, respectively. From Figure 46, it is noted that the present model is good at capturing the displacement history and permanent deformation of the sandwich after impact.

Figure 47 shows that the present model is good at capturing the force history and duration of the sandwich after impact. The present model gives a lower estimation about the contact duration (about 15% lower than the LS-DYNA result) and provides very close peak contact force estimation (about 10% higher than the LS-DYNA results). The discrepancy between the analytical and LS-DYNA results may be caused by the lower contact stiffness estimation in LS-DYNA when compared to the experimental results.

The energy absorbed and its portion consumed by the sandwich deformation are shown in Figures 48 and 49. Figure 48 indicates that the analytical model is very accurate at capturing the energy loss during the contact process. While Figure 49 demonstrates that the analytical model is also very capable of calculating the deformation energy consumed even though the maximum deformation is about 8% difference. The energy absorbed by the sandwich plastic deformation (10.1 J) composes of 95% of the total energy loss (10.3 J), thus demonstrating the effectiveness of proposed I-Lam design in absorbing impact energy and protecting the underneath structures.

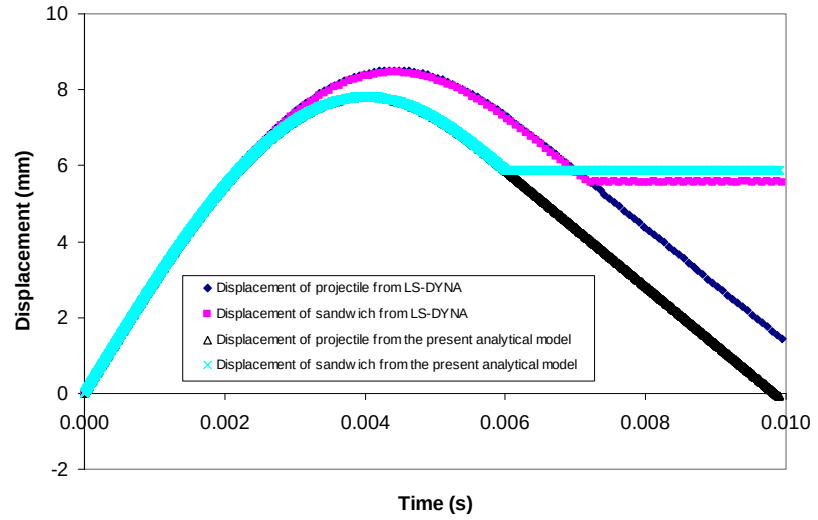

Figure 46 Residual deformation of the sandwich under an impact of 6.62 lb (3 kg) mass with an initial velocity of 6.72 miles/hour (3 m/s)

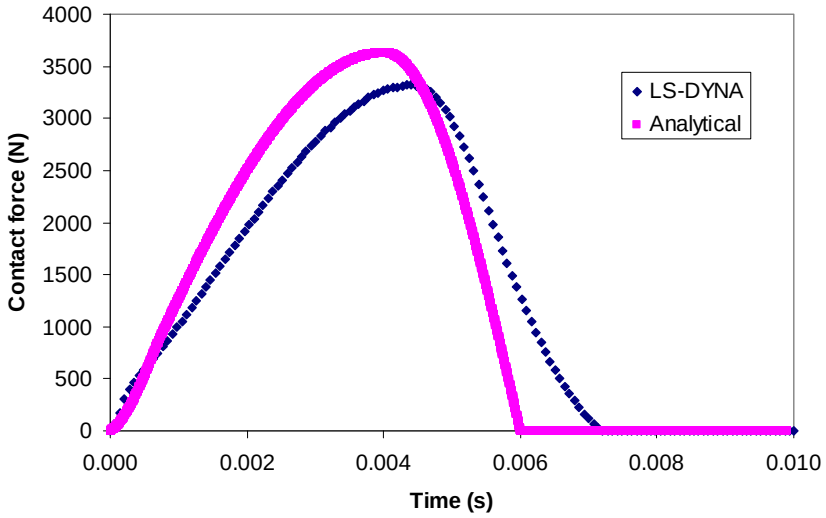

Figure 47 Contact force history and duration of the sandwich under an impact of 6.62 lb (3 kg) mass with an initial velocity of 6.72 miles/hour (3 m/s) (Note: 1 N = 0.224 lbs)

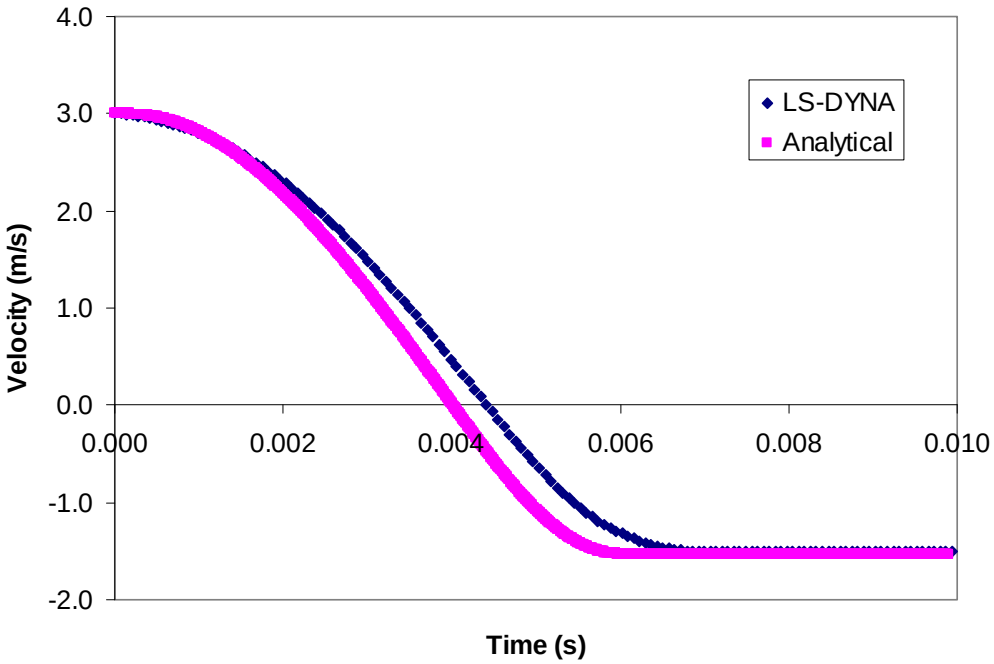

Figure 48 Velocity history of the sandwich under an impact of 6.62 lb (3 kg) mass with an initial velocity of 6.72 miles/hour (3 m/s)

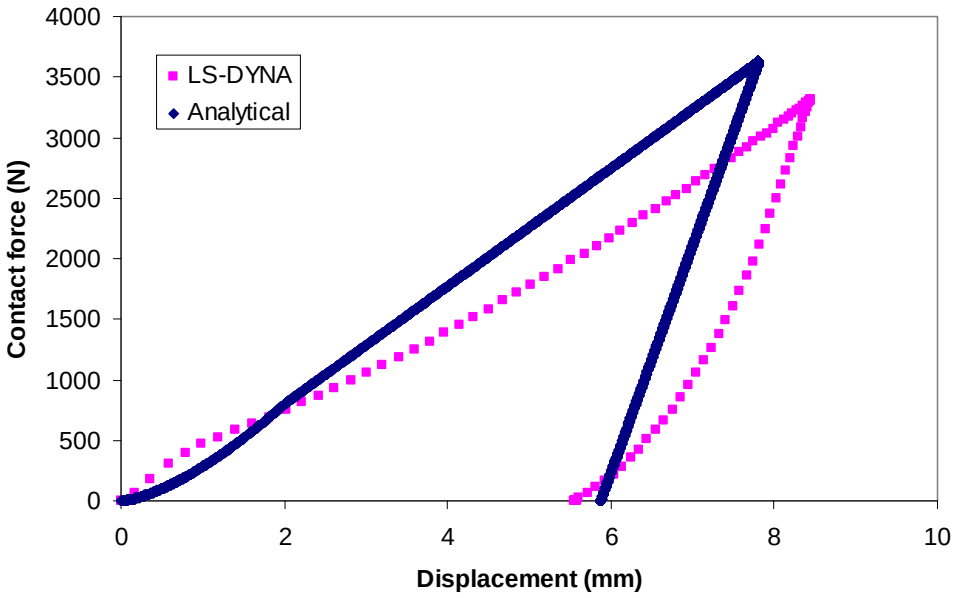

Figure 49 Contact force –displacement curve of the sandwich under an impact of 6.62 lb (3 kg) mass with an initial velocity of 6.7 miles/hour (3 m/s) (Note: 1 N = 0.224 lbs)

5.5.2 Flat crushing impact of sandwich panels

Using the crushing behavior derived in the crushing test, a combined impact with crushing behavior is proposed as follows,

$$P=\begin{cases} K_h\delta^{3/2} & Elastic-Loading & 0\le\delta\le\delta_y \\ P_y & Elastic-Plastic-Loading & \delta_y\le\delta\le\delta_d \\ K_u(\delta-\delta_r) & Unloading-\mathrm{Re}loading & \delta_r\le\delta\le\delta_m \\ P_y+K_D(\delta-\delta_r) & Densitification & \delta_d\le\delta\le\delta_m \end{cases} \tag{48}$$

Considering the multilayer cases of I-Lam used, the sandwich impacted by a passing truck with a velocity of 22.5 miles/hour (10 m/s) with a mass of 66.23 lbs (30 kg) is simulated, and its deformation history is shown in Figure 50. From Figure 50, it is observed that the permanent deformation associated with this case can be reached to 2.98 in. (75.80 mm), corresponding to the situation in which 76% of the first layer is crushed.

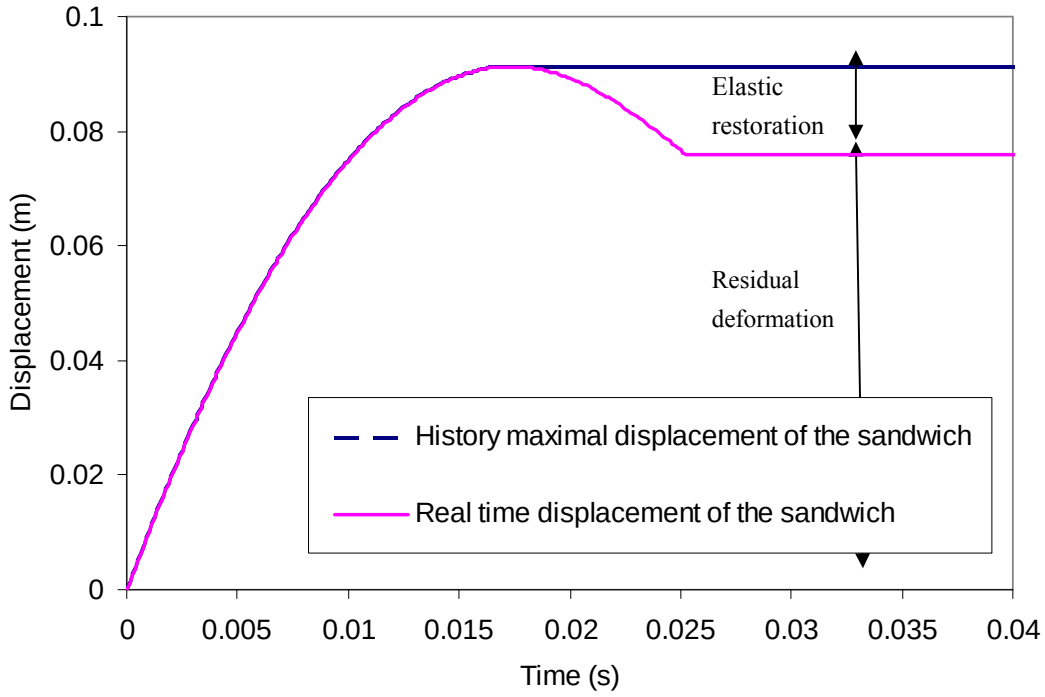

Figure 50 Deformation history of a sandwich panel impacted by a mass of 66.22 lb (30 kg) at a speed of 22.5 miles/hour (10 m/s) (Note: 1 m = 39.37 in.)

The force time history is also captured and shown in Figure 51. In Figure 51, the peak contact force is close to 4,067.0 lbs (18.22 KN), which is safe for a common concrete over a contact area of 35.66 in^2 (0.023 m^2), while the contact duration is close to 0.025 s.

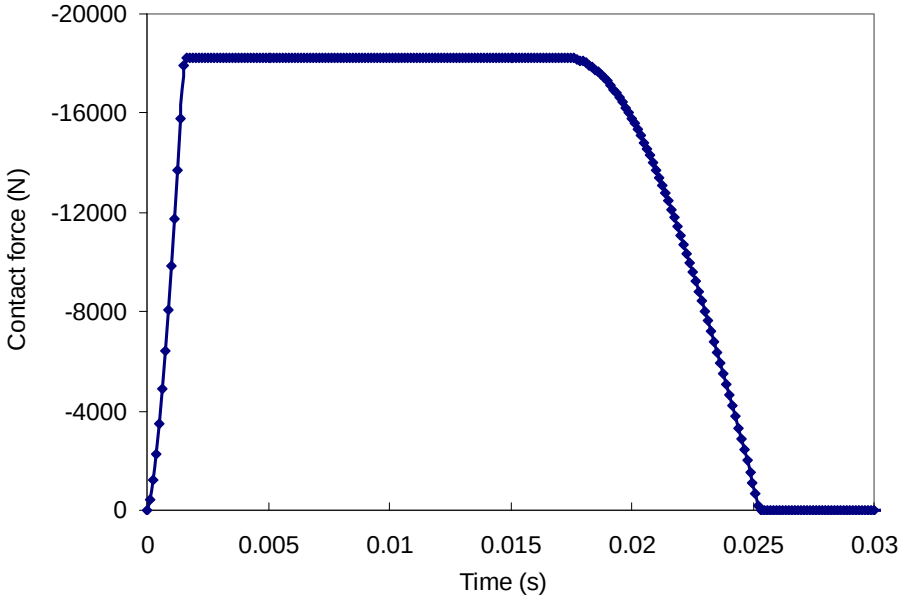

Figure 51 Contact force time history of the multi-layer sandwich impacted by a passing truck with a shear-off mass of 66.22 lb (30 kg) at a speed of 22.5 miles/hour (10 m/s) (Note: 1 N = 0.224 lbs)

The absorbed energy is also calculated and shown in Figures 52 and 53. From Figures 52 and 53, we note that the total loss of energy of the impact process is about 1,365 J and the deformation energy counts about 1,350 J. Thus, most of the energy is absorbed by the deformation of the I-Lam sandwich, and the vibration and the indentation only take a very small portion of the total dissipated energy in this case.

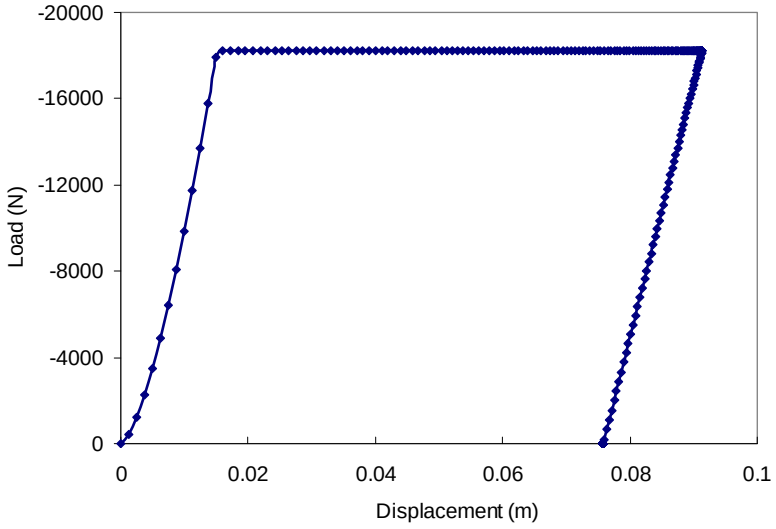

Figure 52 Contact force deflection curve showing the energy absorbed by the deformation of sandwich system (Note: 1 N = 0.224 lbs)

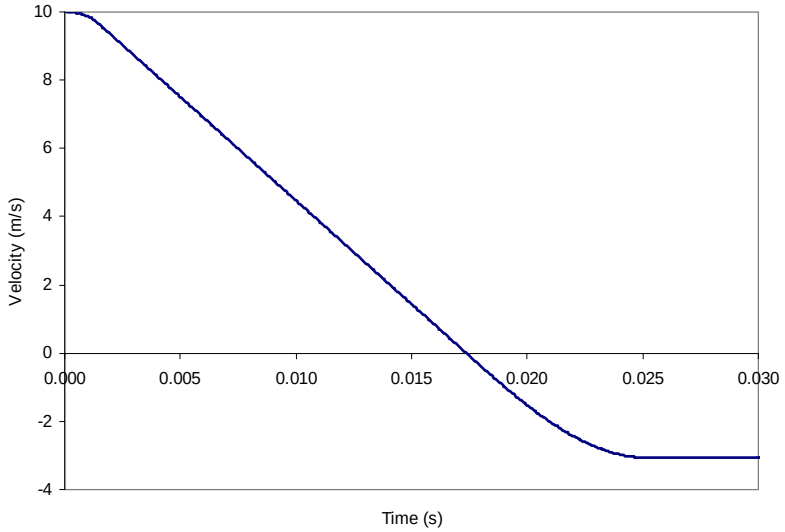

Figure 53 Velocity time history of the projectile when the sandwich panel impacted by a 66.22 lb (30 kg) crushable projectile under a speed of 22.5 miles/hour (10 m/s)

5.5.3 Concluding remarks on impact responses of I-Lam

Based on the experimental crushing and indentation tests and combining the test data (e.g., experimentally-based contact law and core crushing strength), the impact analysis performed can accurately and more realistically predict the impact responses of I-Lam systems, including their elastic and elastic-plastic behaviors, core densification, and energy absorption.

6. FULL-SCALE I-LAM/CONCRETE INTERFACE IMPACT TESTS

To evaluate the performance of I-Lam under real impact application, full-scale I-Lam/concrete interface impact tests were conducted at Transportation Research Center, Inc. (TRC) near Columbus, Ohio, on February 7 and 8, 2006. Three full-scale impact tests were performed: (1) Two reinforced concrete (RC) beams with protection of I-Lam panels designated as I-Lam/Concrete 1 (Figure 54) and I-Lam/Concrete 2 (Figure 55), and (2) One reinforced concrete beam without protection of I-Lam panel designated as Concrete Beam (Figure 56). A 12 x 12 x 12 in (0.3048 x 0.3048 x 0.3048 m) wooden projectile was used to impact the beams in all the three tests, and the impact speed was set as about 45 mile/h (72.421 km/h) in all the tests (see Figure 57 of measured velocity). The load cells were installed at the supports of the RC beams, and the measured maximum reaction forces (Left and Right Load cells) for the three tests are summarized in Table 12. The reaction force histories for all the three tests are shown in Figures 58 to 60. As shown in Table 12, similar reaction forces are achieved for all the three tests under the same wooden projectile impact with the same impact velocity.

Based on the testing observation, a qualitative analysis is summarized. The concrete beams after impact are shown in Figures 61 to 63, for I-Lam/Concrete 1, I-Lam/Concrete 2, and Concrete Beam, respectively. As shown in Figures 61 and 62 for the RC beams protected with I-Lam panels, only minor cracks are induced in the beams after the I-Lam. The partial height of I-Lam panels (see Figures 61(a) and 62(a)) are crushed and damaged, indicating that some of the kinetic energy is absorbed by the I-Lam panel during the impact event, and the kinetic energy is absorbed by effectively crushing and damaging the core materials, the same as observed in the core crushing tests. While for the bare RC concrete beam without I-Lam panel protection, severe concrete beam damage is observed (see Figure 63). Large cracks are developed at the back face of the RC beam, due to impact tensile stresses induced during the impact event. These large cracks are not observed in the I-Lam protected RC beams. The qualitative observation from the full-scale I-Lam interface impact tests and comparisons between the I-Lam protected and unprotected RC beams indicate that the I-Lam panels are capable of protecting the substrate materials from severe damage and absorbing the impact energy by effectively crushing and damaging of core materials.

Table 12 Maximum reaction forces measured from the load cells

Test	Force (left), kips (kN)	Force (right), kips (kN)
I-Lam/Concrete 1	15.176 (67.505)	15.557 (69.203)
I-Lam/Concrete 2	15.220 (67.700)	14.479 (64.405)
Concrete Beam	14.614 (65.005)	15.837 (70.446)

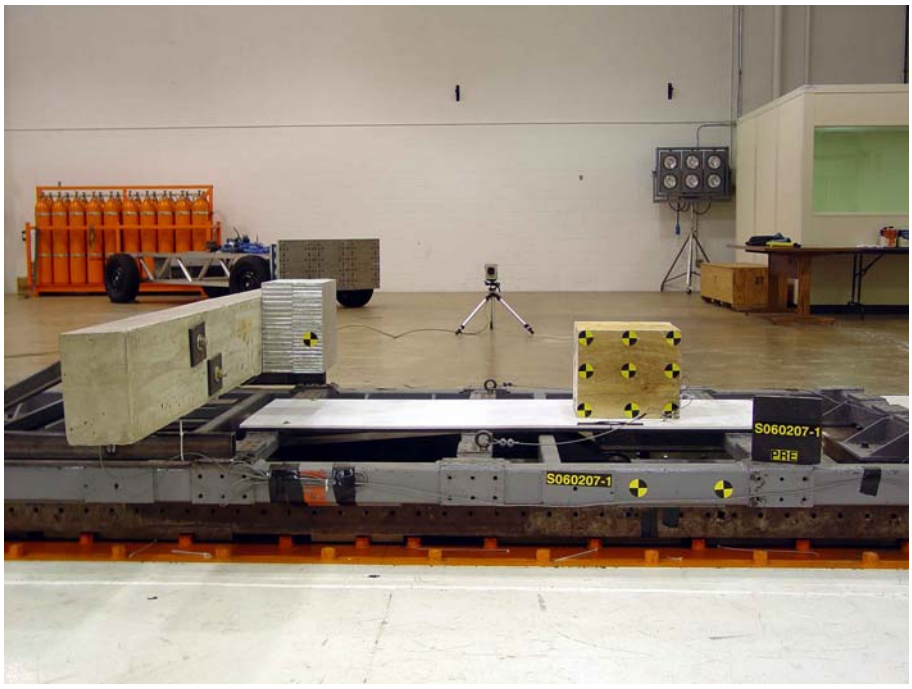

Figure 54 Impact test set-up for concrete beam with I-Lam panel protection (I-Lam/Concrete 1)

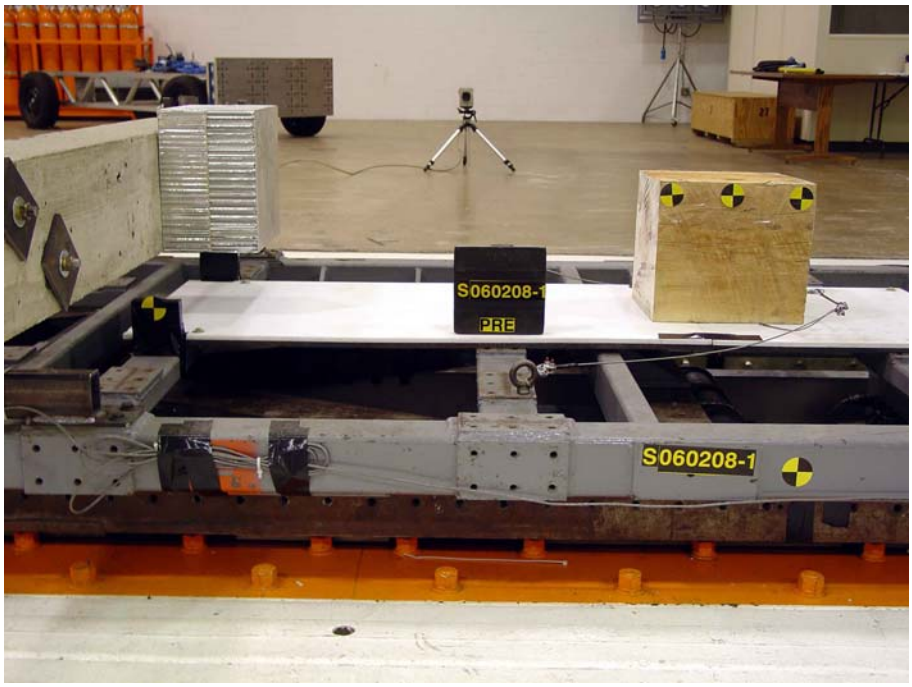

Figure 55 Impact test set-up for concrete beam with I-Lam panel protection (I-Lam/Concrete 2)

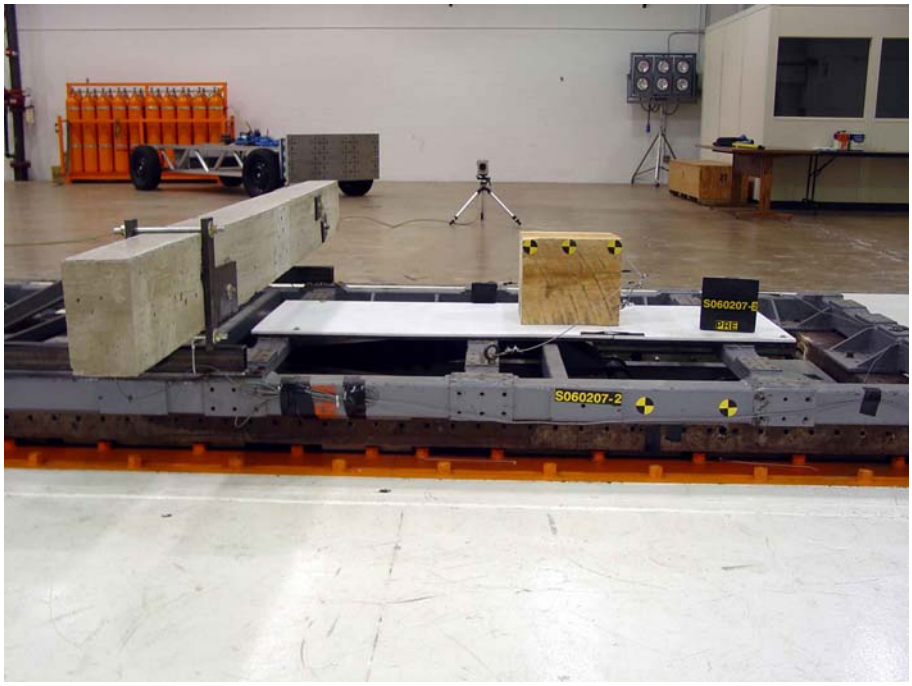

Figure 56 Impact test set-up for concrete beam without I-Lam panel protection (Concrete Beam)

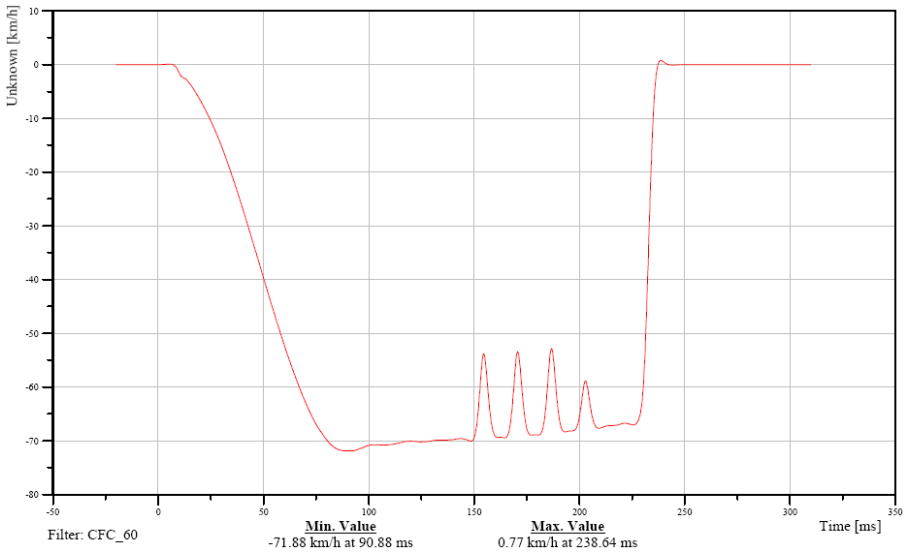

Figure 57 Measured velocity of the wooden projectile in the impact test (I-Lam/Concrete 1)

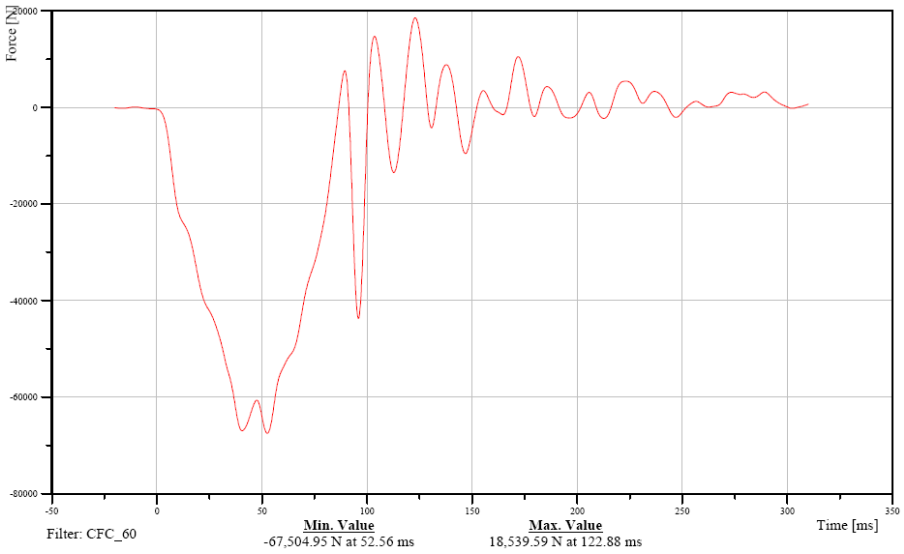

(a) Left load cell

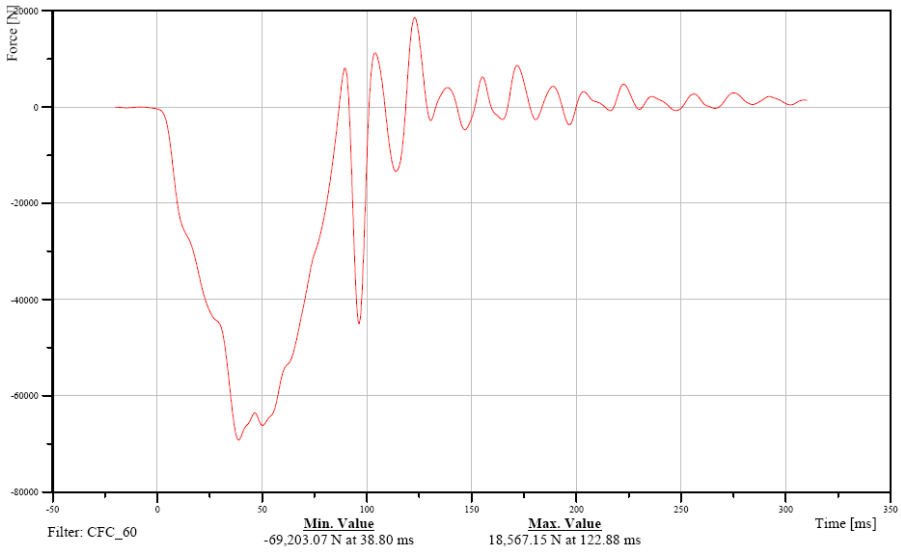

(b) Right load cell

Figure 58 Measured reaction forces from the load cells at the beam supports (I-Lam/Concrete 1)

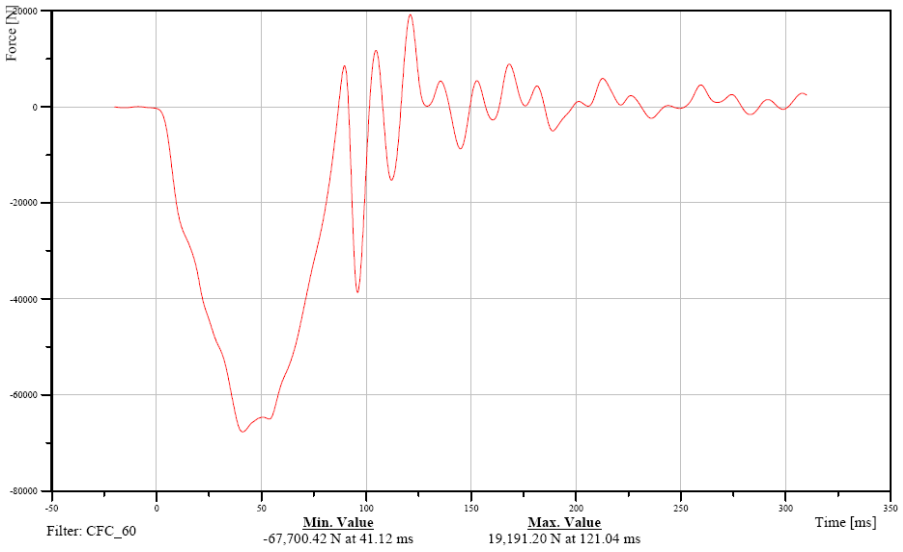

(a) Left load cell

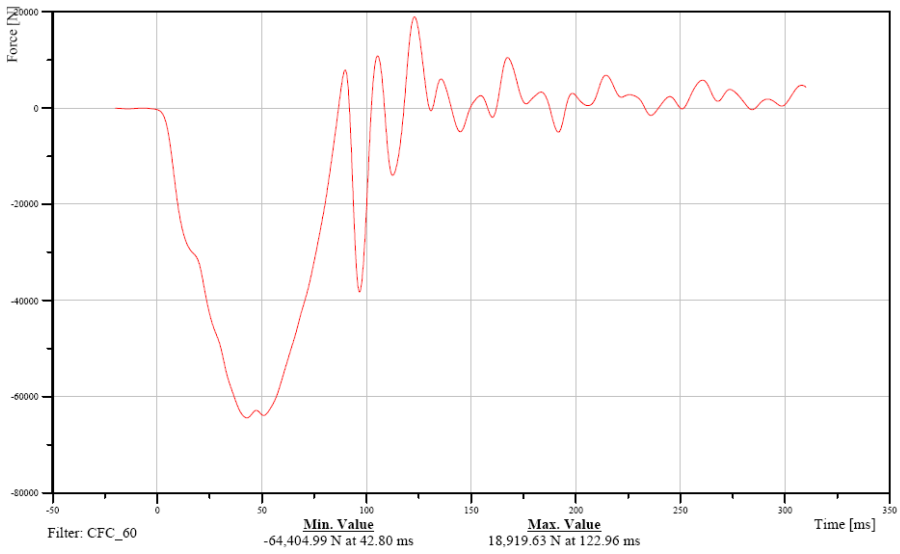

(b) Right load cell

Figure 59 Measured reaction forces from the load cells at the beam supports (I-Lam/Concrete 2)

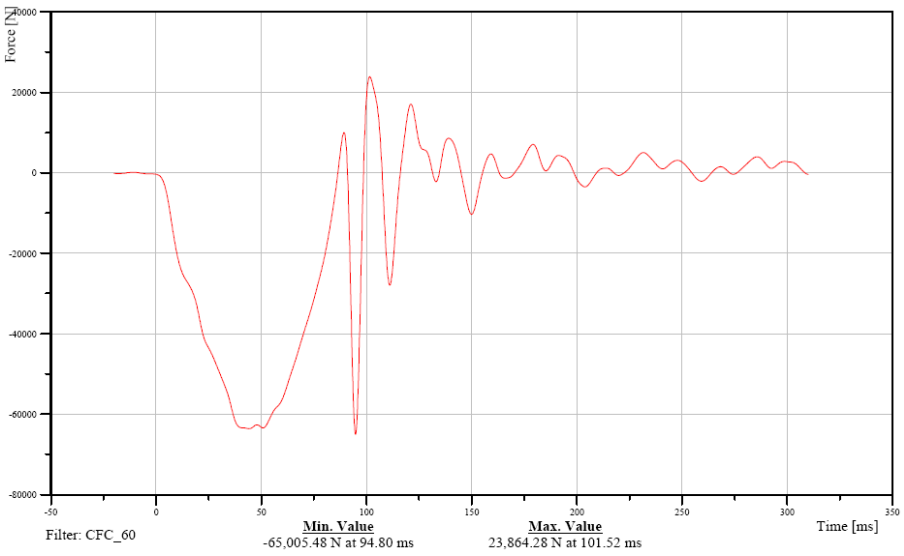

(a) Left load cell

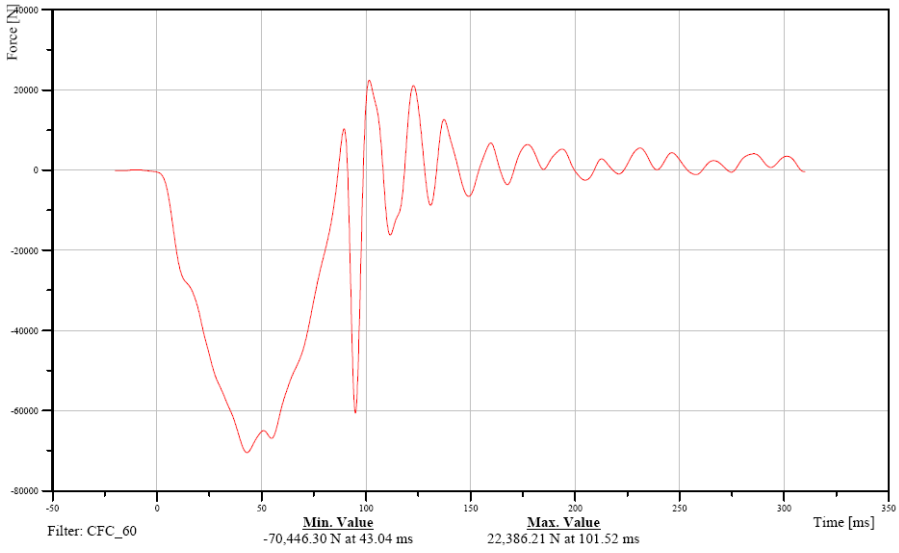

(b) Right load cell

Figure 60 Measured reaction forces from the load cells at the beam supports (Concrete Beam)

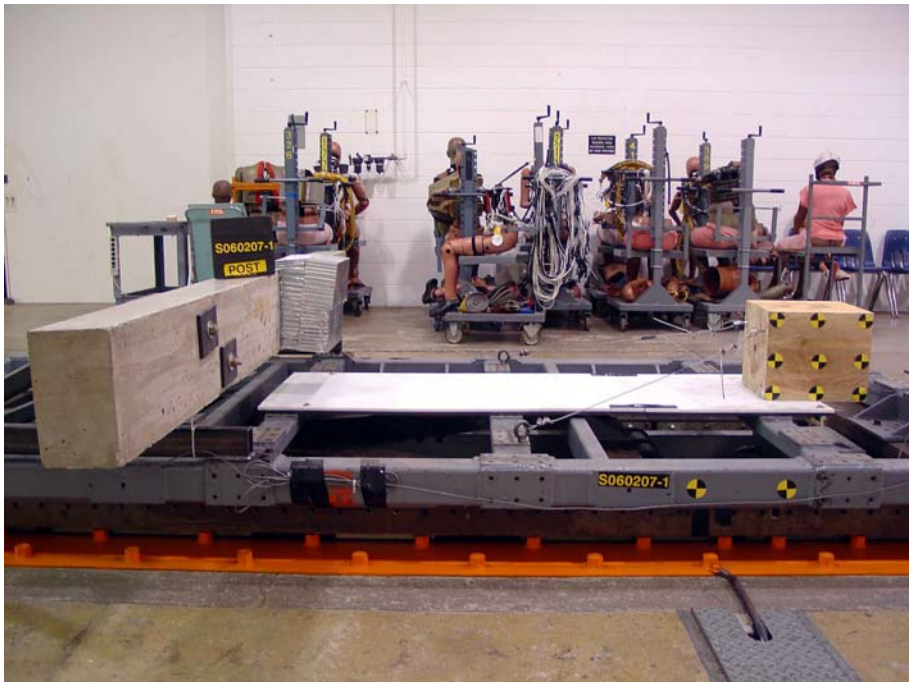

(a) Beam after impact

(b) Marked crack and/or damage

Figure 61 Photos of the I-Lam protected RC concrete beam after impact (I-Lam/Concrete 1)

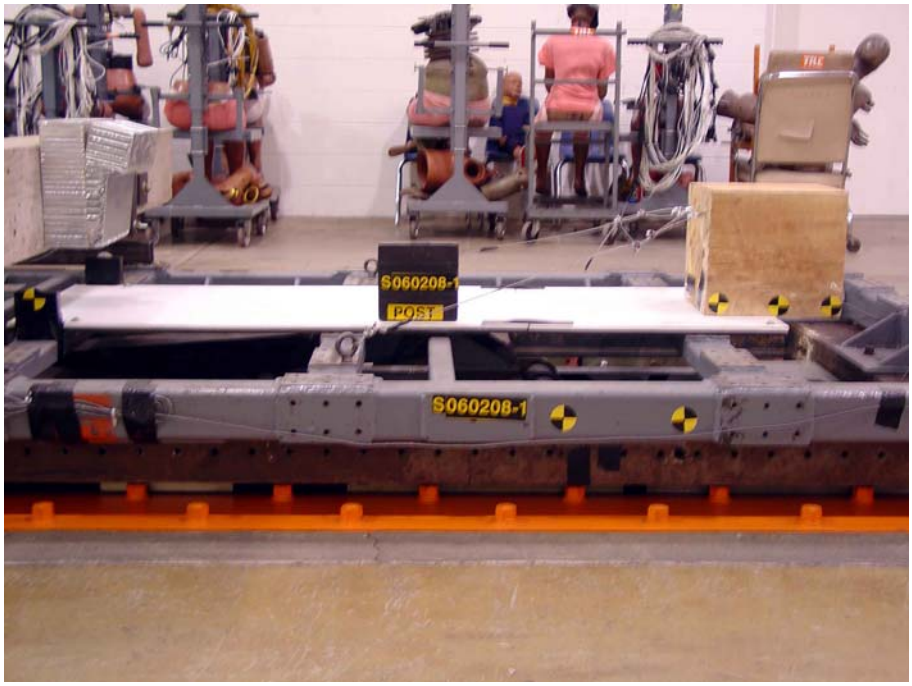

(a) Beam after impact

(b) Marked crack and/or damage

Figure 62 Photos of the I-Lam protected RC concrete beam after impact (I-Lam/Concrete 2)

(a) Beam after impact

(b) Marked crack and/or damage

Figure 63 Photos of the RC concrete beam without I-Lam protection after impact (Concrete Beam)

7. SMART TRIGGERING AND MONITORING SYSTEM

Piezoelectric material has the advantages of being lightweight, low-cost, and easy-to-implement. It can be applied to the impact force detection and health monitoring of large scale of concrete structures.

In recent years, some scholars have conducted research of the impact test with piezoelectric transducer. Lorenz et al. (1994) have designed and calibrated an impact penetrometer using a piezoelectric transducer for use on the spacecraft scheduled to land on the surface of Saturn's moon -Titan. The impact force profile allows estimation of the density and cohesion of the surface material, and its particle size distribution. Lee et al. (1998) designed and built an ultra-high-precision high-speed piezoelectric impact system. The experimental data indicate that this piezoelectric impact hammer has a timing accuracy in the range of microseconds and a positioning accuracy in the range of micrometers. The short impact time achieved by the impact hammer also warrants a high-frequency excitation achievable by the impact hammer. Tong et al. (2002) designed and fabricated a piezoelectric impact hammer for nondestructive evaluation of concrete structures. Due to the stable impact generation of the piezoelectric impact hammer, the experimental results showed that the accuracy of the wave velocity measurement was enhanced significantly through the signal averaging. The accurate impact time origin has been determined by embedding a tiny piezoelectric sensor in the flying head. Measurements of the longitudinal and Rayleigh wave velocities of a concrete specimen were conducted. The newly designed impact hammer can be utilized to measure the depth of a normal surface-breaking crack in a concrete specimen.

Piezoelectric materials have also been successfully applied to the health monitoring of the concrete structures. Many of the conventional nondestructive evaluation (NDE) methods such as C-scan, X-ray, etc. require accessibility to the inspected structural components and usually involve bulky equipment. The piezoelectric material-based health monitoring method has provided a promising approach for health monitoring of large-scale concrete structures. Ayres et al. (1998) utilized the electrical impedance of a bonded piezoelectric actuator/sensor as the means to qualitatively detect structural damage and actively monitor a structure's integrity. This technique is very sensitive to local damage in the sensing area. Tseng and Wang (2004) present a smart-piezoelectric-transducer-based method that is being developed to detect the presence of damage and monitor its progression in concrete structures. The frequency-dependent electric admittance signatures of the piezoelectric transducer are compared with the baseline signatures to determine the status of the health of the structures. The damage is quantified by the root-mean-square deviation (RMSD) index. Saafi and Sayyah (2001) attached an array of piezoelectric transducers to a structure to detect and localize disbonds and delamination of advanced composite reinforcement from concrete structures. The authors compared the transfer function of damaged structure with the undamaged structure to detect the disbond and delamination. Wang et al. (2001) studied the Lamb wave-based health monitoring of both fiber-reinforced composites and the steel-reinforced concrete. For health monitoring of the steel-reinforced concrete, a

piezoelectric sensor network was installed in selected rebars in areas such as the deck, the columns of bridges, and the footing area of columns. Experimental results showed that the cracks or debonding damage in reinforced concrete structures can be detected by the proposed built-in active sensing system. Piezoelectric materials can also be applied to health monitoring in other forms such as powder (Egusa and Iwasawa 1998) or film (Galea et al. 1993). Wavelet transform is a useful signal-processing tool for health monitoring. Quek et al. (2001) used the experimental dynamic response data obtained from piezoelectric sensors to locate the crack position in the beam. By estimating the wave arrival times based on theoretical flexural wave velocity, the approximate wavelet scale to process the data can be determined.

In this report, an overheight impact detection and evaluation system based on piezoelectric material is presented. The proposed method can be divided into two sections: (a) overheight impact detection and image capturing system, and (b) impact evaluation and health monitoring system. This research takes advantage of an early work (Song et al. 2004, 2005). In the previous work, the piezoelectric transducers were embedded into concrete to perform the health monitoring by using wavelet packet analysis. In this research, not only two piezoelectric transducers were used for health monitoring purpose, but also one additional piezoelectric transducer was used to detect impact force and an impact trig circuit was designed for trigging the camera to take photos of the truck which makes accident. Data acquired by the piezoelectric impact transducer was analyzed and the relation between the impact energy and the energy of sensor signal was calculated from the experimental data. The proposed method has the potential to be applied to the in-situ health monitoring and maintenance of bridge.

7.1 Overheight Impact Detection and Image Capturing System

7.1.1 Experimental setup

A concrete specimen with embedded PZT transducers was used for simulating a bridge structure. To detect the actual impact, a circuit was designed to read the PZT signal and output a trigger signal to an image capturing system at the moment of the impact. To reduce the total cost of ownership (TCO), a commercial network camera, DCS3220 from D-Link, was used to take pictures of the offensive vehicle. The camera is capable of capturing sill images, and it sends them by email or File Transfer Protocol (FTP) to a remote location. Also, an integrated trigger input in the back of the camera allows sending pictures based on the level of the input itself. To receive the images, a local networked computer with Serv-U FTP server software loaded was used. All networked components were connected using a Linksys router BEFSR41. Figure 64 shows the block diagram of the complete system.

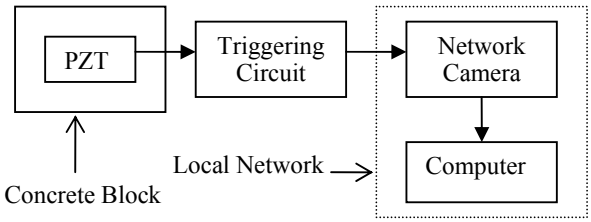

Figure 64 Block diagram of impact detection system

For the actual simulation of an impact, a radio controlled (RC) truck model was used in the test. After an initial inspection, the model was modified to create a stronger impact on the concrete block, meanwhile not damaging itself in the process. The concrete block was elevated to about 6 inches from ground to allow the truck to impact the lower area of the bridge. In addition to the RC truck, a Modally Impact Hammer from PCB Piezoelectronic Inc. Model 086C03 was used for calculating the force applied to the concrete block during impact testing.

Labview 7.1 software with the NIDAQ 6251 PCI acquisition board and the SC2345 signal conditioning unit was used to capture relevant data from the circuit and the impact hammer. A total of 3 probes were used to capture the piezoelectric, the output trigger, and the hammer signal.

7.1.2 System and circuit design

Piezoelectric sensors output a charge proportional to the mechanical stress applied to them. In terms of voltage, the output signal is approximately

$$V = \frac{Q}{C} \tag{49}$$

where Q is the charge generated and C is the PZT internal capacitance. The piezoelectric model used in this experiment is composed by a voltage source in series with a capacitor. Our goal is to identify the maximum voltage level of the piezoelectric signal and compare it to a preset value. When the PZT signal does not exceed the preset value, the circuit will remain in a normal low voltage state. If the impact signal is higher than the preset value, the circuit will change its output from low to high voltage. Figure 65 shows the triggering circuit block diagram used in this experiment.

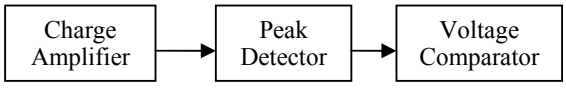

Figure 65 Triggering circuit block diagram

The internal capacitance of PZT sensors combined with an external resistive load, such as the one found in cables or bench instruments, is equivalent to a high pass filter. To avoid reducing the signal strength at low frequencies, a charge amplifier design was used. The amplifier produces a voltage proportional to the input charge; thus, small changes in the input capacitance will not affect the output amplitude. The following equation describes the transfer function of the amplifier

$$H(s) = -\frac{(R_f C_{PZT})s}{(C_f R_f C_{PZT} R_1)s^2 + (C_{PZT} R_1 + C_f R_f)s + 1} \tag{50}$$

After amplifying the piezoelectric signal, the circuit identifies the highest voltage reached using a peak detector which is composed by a simple diode-capacitor combination. The last block in the triggering circuit compares the peak detector voltage to a preset voltage reference. The output will be at a high voltage when an impact is detected, and it will stay high for

$$t = -R_5 C_2 \ln\left(\frac{V_{ref}}{V_{pk}}\right) \tag{51}$$

where V_{ref} is the preset voltage reference, V_{pk} and R_5C_2 are respectively the voltage detected and the time constant of the peak detector. The preset voltage reference should be used to change the impact sensibility of the circuit.

To actually capture the picture of the offense vehicle, the output of the triggering circuit was directly connected to the network camera trigger input. Through the web-based interface, the camera was set up to connect to the local computer and save a picture of the impact when a rise in voltage is detected at the trigger input. To accomplish the transfer of images, a local network was setup using a router and a FTP server on the local computer. To simplify the experiment setup, administrator privileges were granted to the FTP client that will eventually connect to save the pictures.

7.1.3 Experiment results

After setting up the experiment, the radio controlled truck was sent several times against the concrete block. The signal generated by the piezoelectric sensor and the output trigger was recorded using Labview. During the pre-testing time, the RC truck did not create a strong enough impact. To detect the impact, the sensitivity of the circuit, or preset value, was adjusted.

In the first impact after the pre-testing period, the circuit captured and processed the signal correctly. At the same time, the network camera took a picture of the ongoing impact.

In this experiment, the preset voltage reference was set to 6 V. Figure 66 shows the signal detected and the output trigger.

During the impact, the RC truck did not hit the concrete block perpendicularly, but with a small angle. Figure 66 shows that the first impact happened approximately 120 ms before the final one. The length of the first impulse was not recognized by the network camera input. Unfortunately, the minimum trigger signal period value was not available from the manufacture, but can be estimated at approximately 50 ms. A picture of the impact is shown in Figure 67.

In a second attempt, the RC truck was exchanged with an impact hammer. The tool outputs a signal proportional to the force applied to the concrete block. Figure 68 shows the hammer, the piezoelectric, and the trigger output signals. The maximum force applied by the hammer in this second attempt was 1501 N while the trigger signal was high for 64 ms. The force calculation was provided by the hammer resolution of 2.25 mV/N.

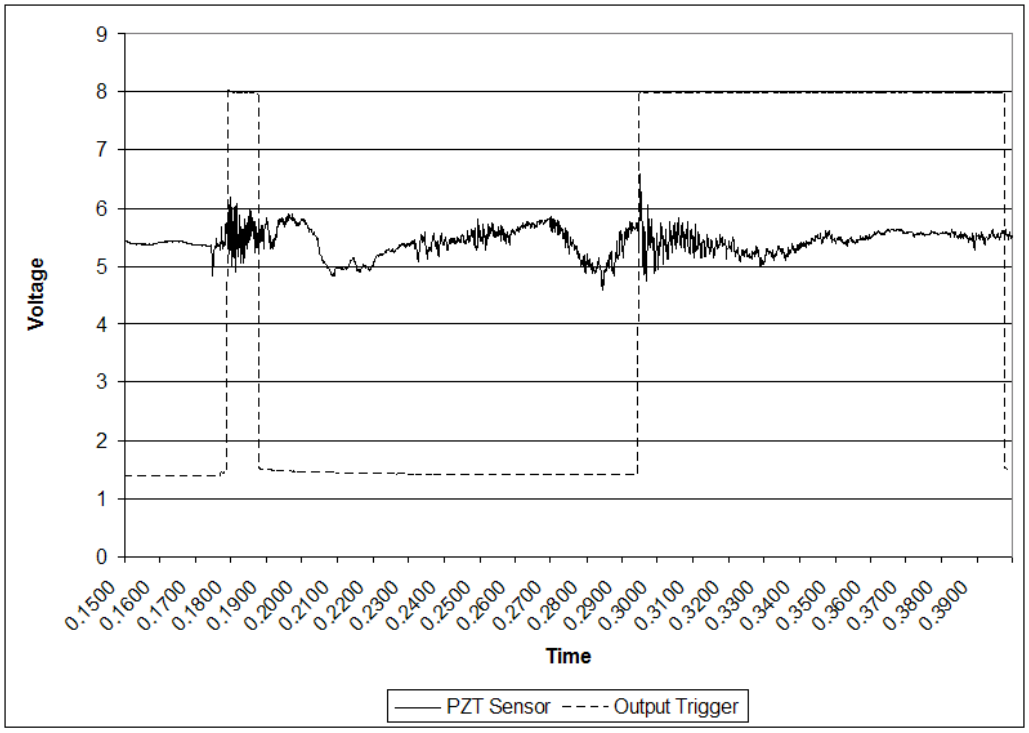

Figure 66 PZT and output signal from triggering circuit during an impact

Figure 67 Acquired picture of the detected impact from first test

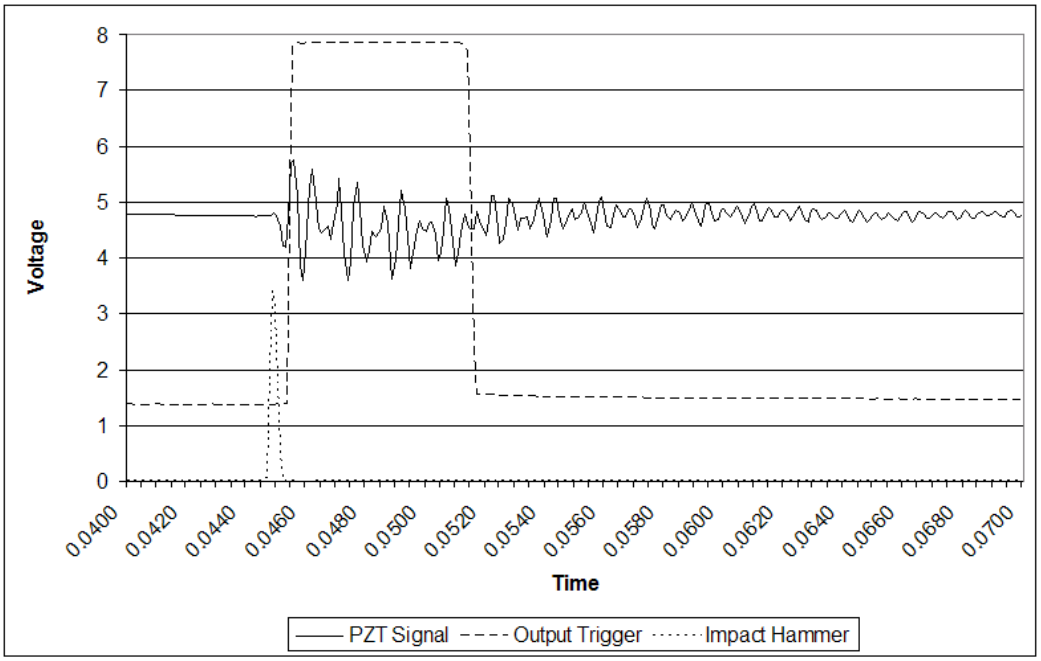

Figure 68 PZT and output signal after impact with the impact hammer

7.1.4 Triggering system

Based on the above impact detection and capturing system design concept, a triggering system is designed. The details of the triggering system are given in Appendix D, and the

flow chart of impact monitoring and triggering system with inclusion of cameras is shown in Figure 69.

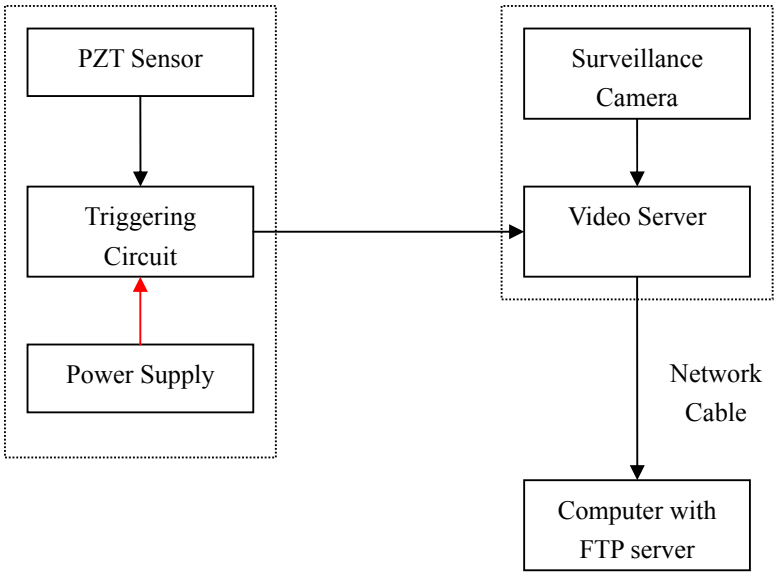

Figure 69 Impact monitoring and triggering system

7.2 Impact Evaluation and Health Monitoring System

7.2.1 Experimental setup

A concrete beam 101.6 × 914.4 × 19 mm (4" × 36" × 0.75") was fabricated as a test object. Three piezoceramic patches (PZT1, PZT2 and PZT3) coated with water-proof coating have been embedded into the concrete specimen before casting. The size of piezoceramic patch is 8 × 8 mm. One piezoceramic transducer (PZT2) was used as impact force detector. It was used to trig the camera to take photos of the offensive truck and also used to estimate the level of impact force. The three piezoceramic transducers were also used for health monitoring purpose. The status of damage level will be determined from the sensor signal by using wavelet packet analysis. Damage index is defined on the basis of the energy vector of the decomposed signal on different frequency bands. A rebar was put at the bottom of the concrete specimen. The diameter of the rebar is 4.7625 mm (0.1875"). Figure 70 shows the block diagram of the concrete specimen. The coordinates of the piezoceramic patches and the properties of the piezoceramic transducers are shown in Tables 13 and 14.

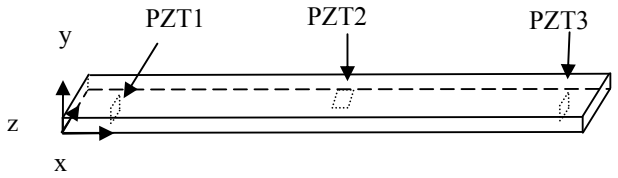

(a)

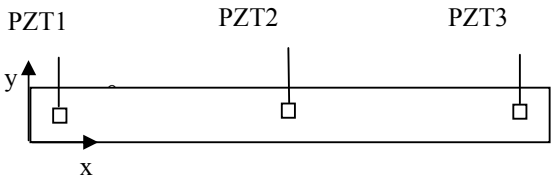

(b)

Figure 70 (a) Concrete specimen (b) Top view of the concrete specimen

7.2.2 Impact tests

Impact tests include two parts (1) Impact hammer test. (2) Free dropping test. During impact hammer test, an impact hammer was used to generate impulse impact at different peak values on the concrete specimen. The relation between the sensor signal and the impulse signal is analyzed. In the free dropping test, two balls of different masses were freely dropping from different heights. The relation between output of impact sensor energy and impact velocity and impact force was analyzed. The experimental data show that the output of sensor energy is related with both impact force and impact velocity.

Table 13 The coordinates and capacitance of the pezoceramic transducers (1 inch = 25.4 mm)

	X (inch)	Y (inch)	Z (inch)	Capacitance (nF)
PZT1	2	2	0.375	4.41
PZT2	18	2	0.375	4.21
PZT3	34	2	0.375	4.43

Table 14 Properties of the piezoceramic transducer

Property coefficient		Unit	value
Strain/field coefficient	d_{33}	Meters/Volt	390×10^{-12}
Strain/field coefficient	d_{31}	Meters/Volt	-190×10^{-12}
Strain/charge density coefficient	g_{33}	Volts/Newton meter	24×10^{-3}
Strain/charge density coefficient	g_{31}	Volts/Newton meter	-11.6×10^{-3}
Coupling coefficient	k_{33}		0.72
Coupling coefficient	k_{31}		0.35

7.2.3 Background of piezoelectric transducer

The piezoelectric effect was discovered by Jacques and Pierre Curie in 1880. Piezoelectricity is a phenomenon exhibited by non-centrosymmetric crystals whereby an electric polarization (i.e. charge) is induced in the material upon the application of a stress. Conversely, it is the development of an induced strain which is directly proportional to an applied electric field. In piezoelectric materials the elastic and electrical properties are coupled; mechanical and electrical parameters must therefore be involved in constituent relations. For a piezoelectric medium, the interaction between electrical and mechanical variables can be described by linear relations of the form

$$D = dT + \varepsilon^T E \tag{52a}$$

$$S = s^E T + dE \tag{52b}$$

where D represents electric displacement, d represents piezoelectric coefficient, ε^T is the dielectric constant. T is the stress. E is the electric field. S^E is compliance. The first equation describes the direct piezoelectric effect while the second equation describes the converse piezoelectric effect. The direct piezoelectric effect means the piezoelectric material will generate an electric charge when subjected to mechanical stress. The piezoelectric material could function as sensor due to the direct piezoelectric effect. The converse piezoelectric effect means the piezoelectric material will generate a mechanical strain in response to an applied electric field. The piezoelectric material could function as actuator due to the converse piezoelectric effect.

At present the most suitable and popular piezoelectric ceramic materials are Lead Zirconate Titanates (PZT). The leading position of the Lead Zirconate Titanates is due to their strong piezoelectric effect and high Curie point, together with the wide range of properties they offer simply by making small changes in composition. PZT can be fabricated into different shapes to meet specific geometric requirements. PZT patches can often be used as

both sensors and actuators which can be integrated into structures. In the proposed impact detection and evaluation system, PZT patches are used as transducers embedded into concrete before casting.

The open-circuit voltage yielded by the PZT transducer when compressed with force F is $g_{33}Ft/A$, where A is the area of transducer, t is the thickness of the PZT transducer and g_{33} is the piezoelectric voltage constant. The piezoelectric voltage constant is defined as the electric field generated in a material per unit mechanical stress applied to it. The first subscript refers to the direction of the electric field generated in the material or to the applied electric displacement; the second refers respectively to the direction of the applied stress or to the direction of the induced strain. The area of the PZT transducer is 64 mm^2. The thickness of the transducer is 0.267 mm. The piezoelectric voltage constant g_{33} is 24×10^{-3} VmN^{-1}.

7.2.4 Impact hammer test

Modally Tuned Impact Hammer (model NO. 086C03, PCB Inc.) was used for impact test. Sensitivity: 2.25 mV/N. Hammer mass is 0.16 kg. LeCroy Waverunner digital oscilloscope (model No. LT 342) was used to record the impact signal and the sensor signal at the sampling frequency of 1 MHz. When the hammer impacts the concrete specimen, the impact impulse signal can be captured from a PZT transducer which is embedded inside the hammer. The output of the hammer signal is proportional to the impact force. From the impact hammer experiment results (Figure 71), it can be seen that the peak value of impact sensor is proportional to the peak value of the impact hammer. The peak value of impact sensor can be used to estimate the impact force peak value.

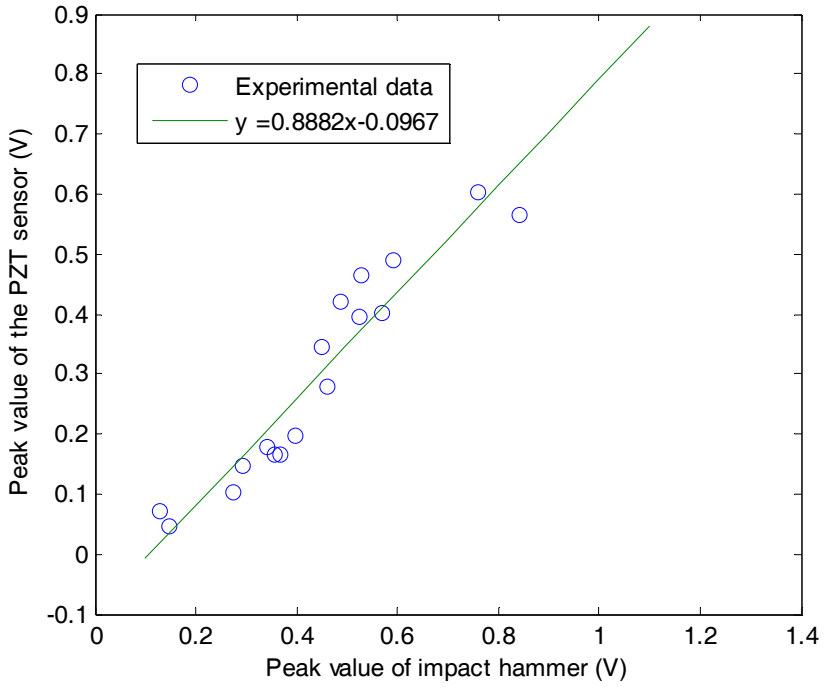

Figure 71 The PZT impact peak voltage VS. peak value of the hammer

7.2.5 Free dropping impact test

In order to study the relation between impact energy and sensor signal, free dropping impact test is implemented on the concrete specimen. The impact of a free dropping ball is point load for the concrete specimen. Two balls were used for test. The mass of one ball is 28 gram; the mass of the other ball is 242 gram. Both balls were freely dropping at different height at zero initial velocity. From the conservation of energy principle, the value of the kinetic energy when impact happens should be the amount of the loss of the potential energy from the dropping point. By adjusting the height, the impact kinetic energy is changed. The energy of PZT impact sensor is calculated as

$$E = \int_{t_0}^{t_f} u^2 dt \tag{53}$$

where t_o is starting time, t_f is finish time and u is the sensor voltage.

From Figure 72, it can be seen that the relation between the sensor energy and impact energy is linearly proportional and the two curves have similar slope for different masses. For the same mass, bigger impact energy means bigger impact velocity. With the increment of impact velocity, the impact energy is increasing which will result in the proportional increment of the energy output of impact sensor. The increment ratio of sensor energy to impact energy is regardless of mass. However, from the experimental results, the 242 gram ball has more energy output than the 28 gram ball if they have the same impact energy. This is because for the same impact energy, the impact force of 242 gram ball is much larger than that of the 28 gram ball if the impact duration is assumed the same. A larger impact force will generate more charge on the PZT impact sensor. There would be more cycles for the reaction force to stop the bigger mass ball at last. From the time response comparison different mass ball at the same velocity and the time response comparison of the same mass ball at different velocity, it can be seen that the impact effect is both related with the velocity and the impact force. Figure 73 shows the time response comparison of different impact forces at same impact energy. Figure 74 shows the time response comparison of different impact forces at same velocity. Figure 75 shows the time response comparison of the same impact force at different velocities.

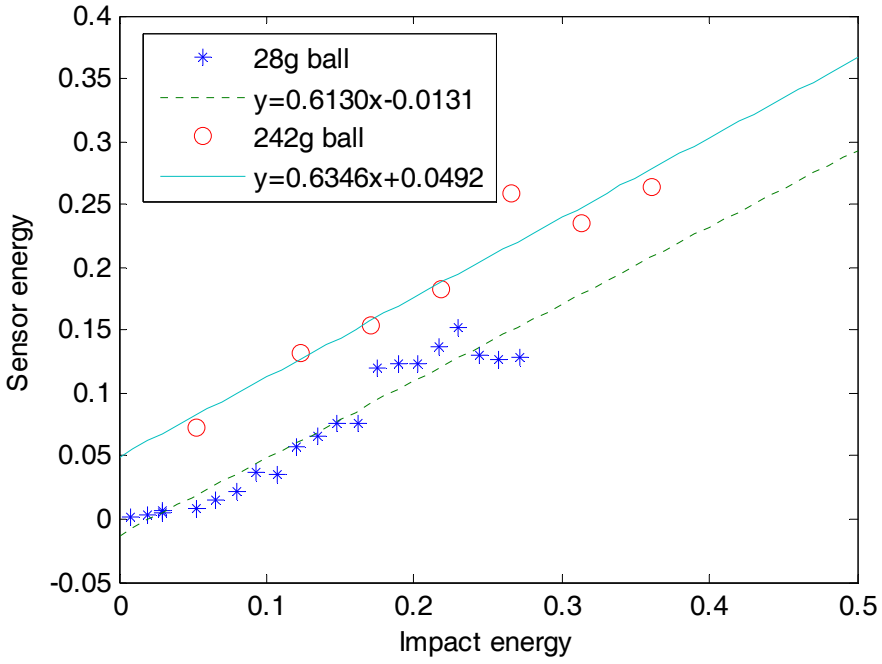

Figure 72 The sensor energy VS. the impact energy.

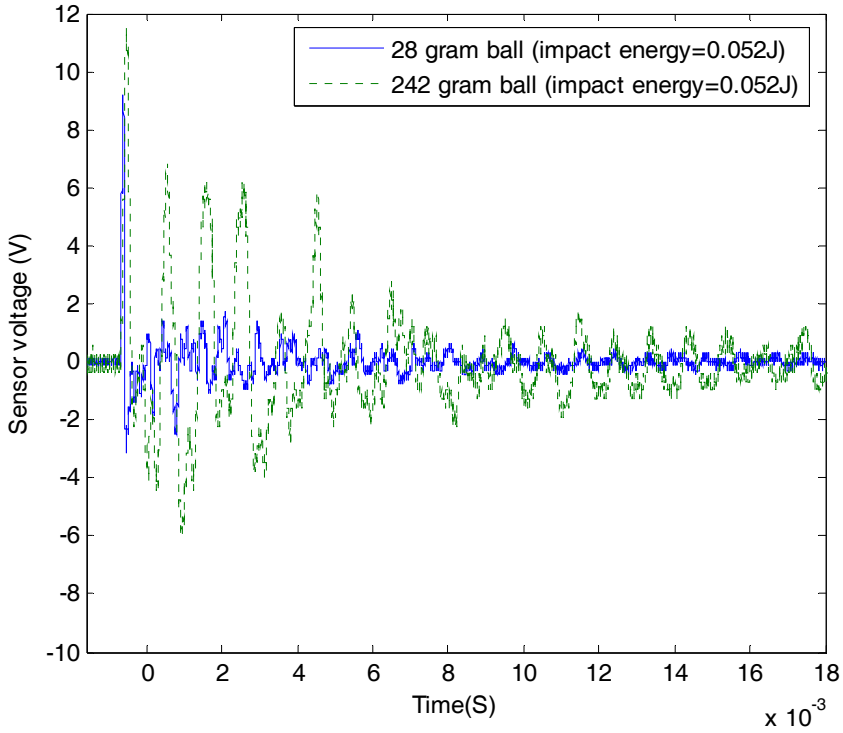

Figure 73 The time response comparison of the 28 gram ball with 242 gram ball at the same impact energy value (0.052 J)

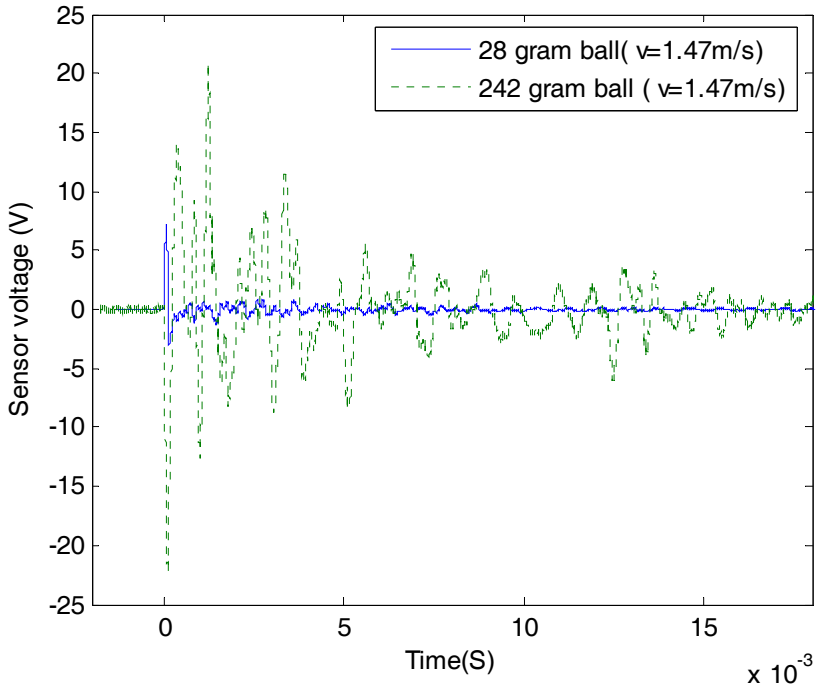

Figure 74 The time response comparison of 28 gram ball with 242 gram ball at the same impacting velocity (v = 1.47 m/s).

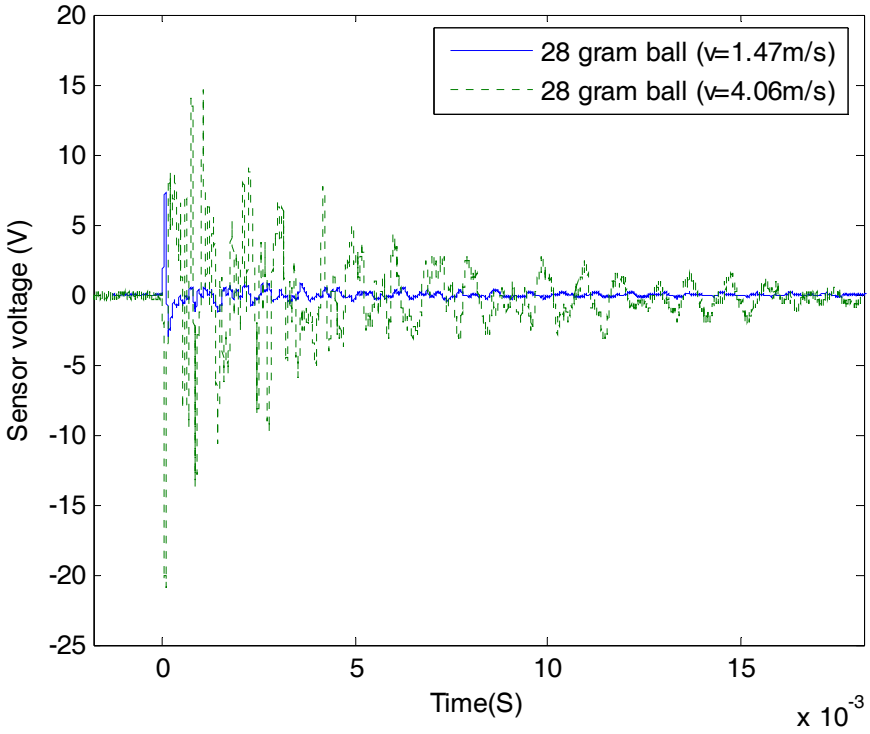

Figure 75 The time response comparison of 28 gram ball at different impact velocities

7.3 Health Monitoring of Concrete Girder after Impact

During the impact test, health monitoring test is conducted simultaneously. The wavelet packet analysis is used as the signal-processing tool to analyze the sensor signal of the imbedded PZT patch in concrete. A wavelet is a waveform of effectively limited duration that has an average value of zero.

$$\int_{-\infty}^{+\infty} \Psi(t)dt = 0 \tag{54}$$

Using a selected mother wavelet function $\Psi(t)$, the continuous wavelet transform (CWT) of a function *f*(t) is defined as:

$$W_f(a,b) = \frac{1}{\sqrt{a}} \int_{-\infty}^{+\infty} f(t)\bar{\Psi}(\frac{t-b}{a})dt \tag{55}$$

where $a > 0$ and $b \in R$ are the dilation and translation parameters, respectively. The bar over Ψ (t) indicates its complex conjugate. In wavelet analysis, a signal is split into an approximation and a detail. The approximation is then itself split into a second-level approximation and detail, and the process is repeated. In wavelet packet analysis, the details as well as the approximations can be split. The advantage of wavelet packet analysis is that it enables the inspection of relatively narrow frequency bands over a relatively short time window. In this report, Daubechies wavelet base (db9) is used as the mother wavelet. The frequency band is not overlapped because of the orthogonality of the Daubechies wavelet base. In the proposed method, the sensor signal S is decomposed by an *n*-level wavelet packet decomposition into 2^n signal sets $\{X_1, X_2, \cdots X_{2^n}\}$ with

$$X_j = [x_{j,1}\ x_{j,2}, \cdots, x_{j,m}] \tag{56}$$

where *m* is the number of sampling data. $E_{i,j}$ is the energy of the decomposed signal, where *i* is the time index (window index), *j* is the frequency band ($j = 1,\ldots, 2^n$).

$$E_{i,j} = \left\| X_j \right\|_2^2 = x_{j,1}^2 + x_{j,2}^2 + \cdots + x_{j,m}^2 \tag{57}$$

The energy vector at time index *i* is,

$$E_i = [E_{i,1}, E_{i,2}, \cdots, E_{i,2^n}] \tag{58}$$

Various kinds of damage indices have been developed for health monitoring of civil structures in recent years. Root-mean-square deviation (RMSD) is a suitable damage index to compare the difference between the signatures of healthy state and damage state. Soh *et al.* (2000) successfully conducted RMSD between signatures of PZT transducer to form the damage index for health monitoring of a reinforced concrete (RC) bridge. Tseng & Naidu (2002) presented the damage index by calculating the RMSD between the impedance of the PZT transducer mounted on aluminum specimens. In this report, RMSD of the energy vector is calculated as the damage index for the health monitoring purpose.

The energy vector for healthy data is denoted as $E_h = [E_{h,1}, E_{h,2}, \ldots, E_{h,2^n}]$. The energy vector for damage state at time index *i* is represented by $E_i = [E_{i,1}, E_{i,2}, \ldots, E_{i,2^n}]$. The damage index at time *i* is defined as

$$I = \sqrt{\frac{\sum_{j=1}^{2^n} (E_{i,j} - E_{h,j})^2}{\sum_{j=1}^{2^n} E_{h,j}^2}} \tag{59}$$

During the test, a sweep sinusoidal signal was used as excitation source for the piezoceramic actuator (PZT1). The magnitude for the sweep sinusoidal signal is 20 V. The sweep sinusoidal signal starts from 100 Hz and ends at 10 kHz. The sweep period is 10 seconds. PZT1 was used as actuator and PZT2 and PZT3 were used as sensors.

The proposed damage index represents the transmission energy loss portion caused by damage. When the damage index is close to 0, it means it is in healthy state. The greater the index, the more severe the damage is.

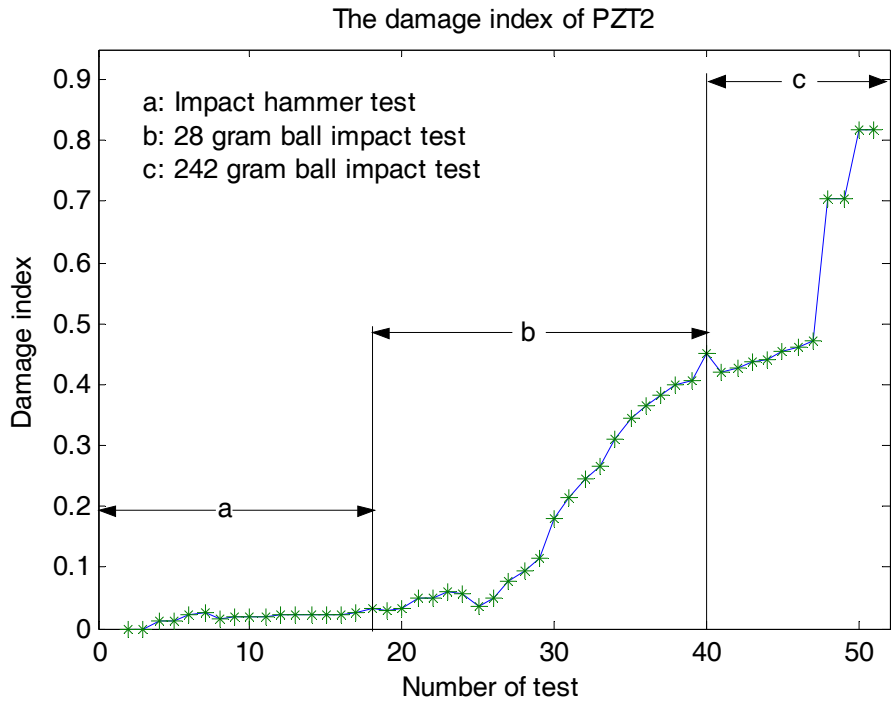

Figure 76 The damage index during the impact hammer test and free dropping test for PZT2

During the test, the impact hammer test was implemented first. After impact hammer test, 28 gram ball impact test and 242 gram ball impact test were implemented until the concrete was damaged into a severe status. From the damage index history (Figure 76), it can be seen that during the impact tests, the damage index was increasing, this means there were more damages happened inside with the repeating impact. After the concrete specimen was cracked, the width of the crack occurred in the center of the concrete specimen is 0.002 inch at the top, 0.005 inch in the middle part and at 0.015 inch the bottom.

8. INSTALLATION OF I-LAM IN CONCRETE BRIDGE (DEL-23-12.99)

The I-Lam panels were installed on a slab concrete bridge (DEL-23-12.99) in Delaware, Ohio by the ODOT District 6 on Oct. 31 to Nov. 1, 2006. A total of 20 I-Lam panels were installed over two traffic lanes. A schematic of the I-Lam panels on the DEL-23-12.99 is shown in Figure 77. The details of I-Lam installation is shown in Figure 78. The construction details include the following steps:

(1) Sandwich panels (I-Lam) of 12” x 12” x 8” (304.8 x 304.8 x 203.2 mm) were first adhesively bonded to the add-on aluminum backing plate and then back-bolted using four rivets at the four corners. The add-on plate has an L-shape which provides anchoring mechanism for the I-Lam to concrete girder (This step was prepared and fabricated in the lab in advance).

(2) In the field, the I-Lam system with L-shape backing plate was attached to the concrete girder using concrete screws. Two concrete screws of 2" long were drilled through the top of add-on aluminum backing plate and into the concrete. An additional screw was drilled through the bottom of L-shape aluminum plate to further secure the I-Lam in position.

(3) A safety steel cable was connected to the top face sheet of I-Lam to provide the additional safety measure (two cables per I-Lam were used).

(4) Total of twenty 12" x 12" x 8" (304.8 x 304.8 x 203.2 mm) I-Lam panels were installed over the coming traffic lanes. The spacing between I-Lams is about 1" (thus, the total install length is about 20 ft plus 19 in. over the traffic lanes).

(5) The conditions (e.g., any existing damage and defect) of the concrete bridge girders were inspected and recorded before the I-Lams are installed, so that a benchmark data is available for later comparisons.

The final installed I-Lam panels on the bridge is shown in Figure 79.

Figure 77 Schematic of I-Lam installation in DEL-23-12.00

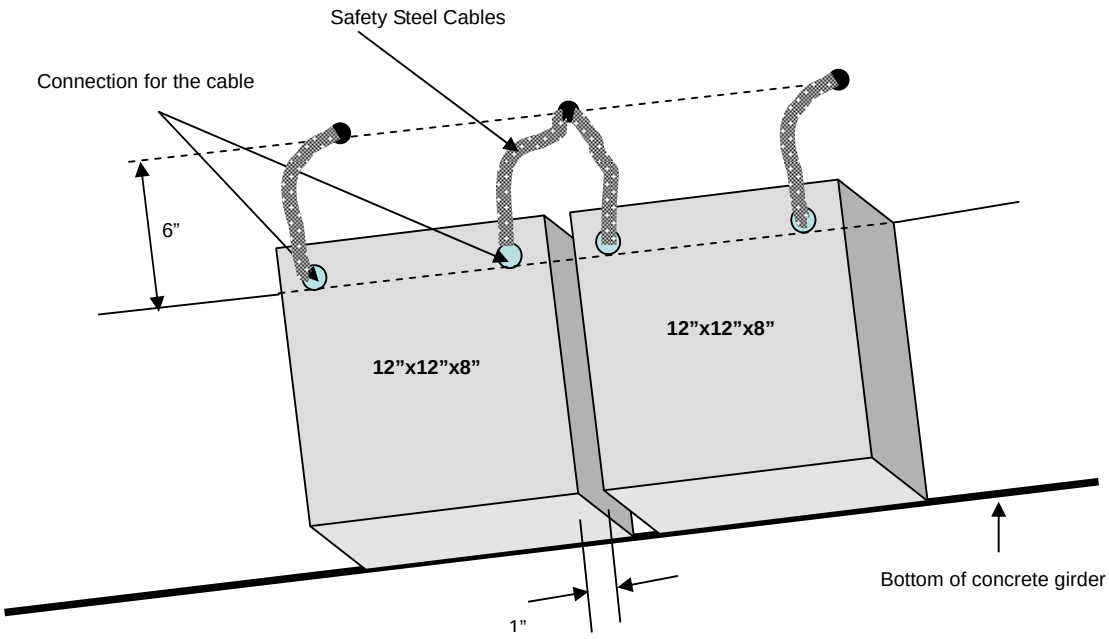

(a) Schematic review

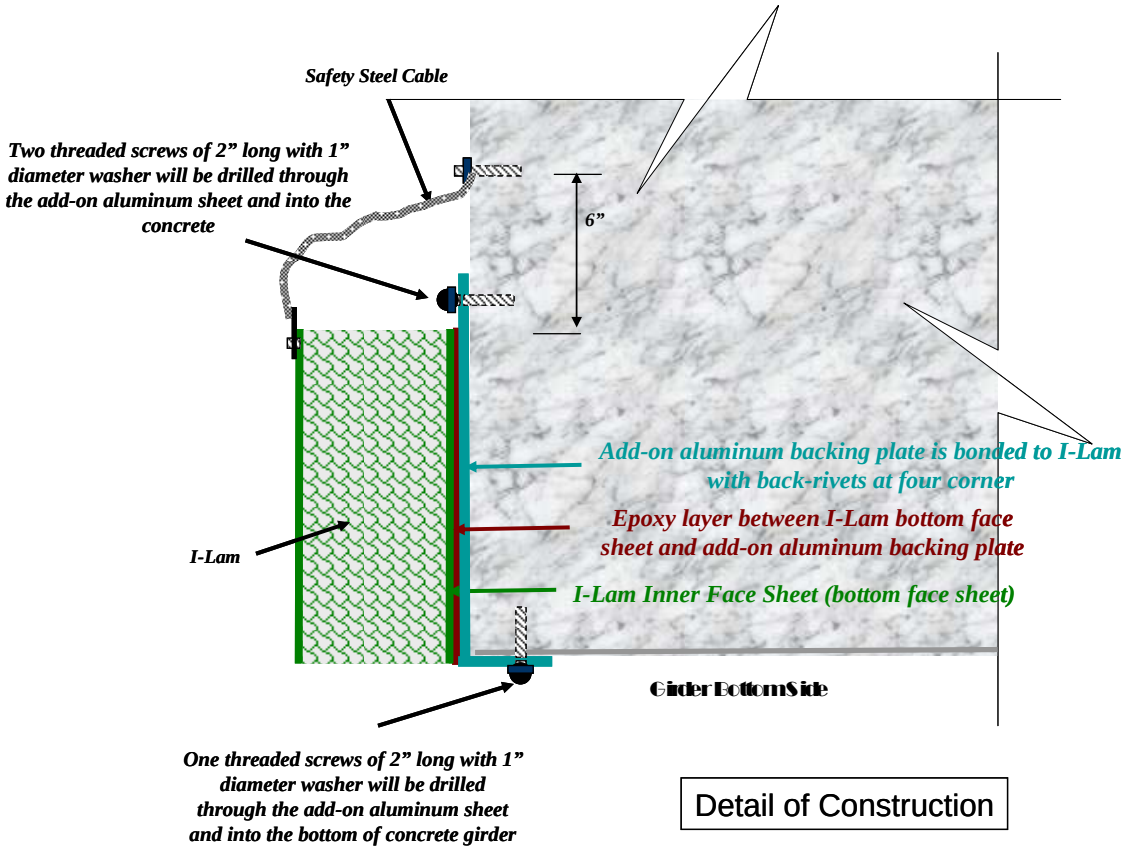

(b) Attachment details

Figure 78 Details of the I-Lam installation

Figure 79 Final installed I-Lam panel on the bridge (DEL-23-12.99)

9. SUMMARY OF RESEARCH FINDING

In this study, an aluminum honeycomb collision protection system so called "I-Lam" (**I**mpact-**Lam**inate) sandwich for concrete bridge girders is developed, designed, analyzed, fabricated, tested, and field-installed. Details of analysis procedures and engineering design criteria for collision protection system are proposed. The following research findings are obtained:

- Three simple linear elastic impact models (i.e., discrete system, beams under concentrated load, and beams under distributed load) for I-Lam sandwich beams with inclusion of shear-off effect of the overheight material are developed. The models are capable of explicitly predicting the contact force, displacement and duration during the impact event. Three simple models in the forms of explicit formulas can be used for preliminary engineering design and analysis of I-Lam sandwich structures for anti-impact applications.

- Three design criteria (i.e., contact force limit, contact displacement limit, and energy absorption limit) for I-Lam sandwich structures are proposed, and they are used as a guideline for designing impact mitigation and protection system. Correspondingly, three design methodologies (i.e., the contact force-based, contact displacement-based, and energy absorption-based) for impact of I-Lam sandwich are developed.

- Energy analysis is established to calculate the energy partition among different

components in an I-Lam sandwich system, and it provides a design criterion for design analysis of impact energy absorption systems, such as I-Lam, and offers predictability for energy absorption capacity of the system.

- Corresponding to the elastic and elastic-plastic impact analysis as well as the energy model, different design analysis stages are defined. They can be used to accurately and more realistically analyze the impact event of I-Lam under different loadings and magnitudes of impact.

- Based on the developed engineering design analysis protocol and the defined loading and impact speed requirements, a bi-layer aluminum sandwich design for I-Lam (see Figure 12) is designed and finalized. The final design product (Figure 13) is fabricated by Plascore Inc. This 12 x 12 x 8 in. I-Lam design will be used as the overheight collision protection system for concrete bridge girders, and the side-by-side arrangement of I-Lam panels will form a collision barrier; while at the same time, they are a scarifying system, in which the individual impact-damaged I-Lam panels can be conveniently replaced after the impact.

- Numerical simulations of plain and reinforced concrete beams with and without I-Lam protections are conducted using the commercial finite element software LS-DYNA. It indicates that with I-Lam protection, the transferred contact force is reduced dramatically, and as expected, about 60 to 70% of the kinetic energy is absorbed by crushing of the aluminum core in the I-Lam.

- Adhesive bond strength along the interface between the I-Lam and concrete substrate is experimentally evaluated, and the interface fracture load and fracture energy are obtained. It indicates that the bond strength between the high density core and concrete are much higher than the one between the low density core and concrete. The interface design between the high density core and concrete can be used in the installation design, if the high strength adhesive will be used to attach the I-Lam to the concrete girders.

- Both the compressive crushing and indentation tests of I-Lam sandwich materials are also performed, from which the elastic-plastic indentation behavior and contact law are experimentally obtained. The crushing and indentation behavior reduced from the experimental data are later used to develop semi-empirical elastic-plastic sandwich impact models for designing and analyzing the I-Lam system.

- The refined analysis based on the experimental data from the crushing and indentation tests is performed, and it indicates that the proposed I-Lam structure meets the given design loading and impact requirements and behaves satisfactorily (core crushing to absorb/mitigate collision energy, reduced contact force, and protecting the underneath concrete structures).

- Full-scale impact test are conducted to three reinforced concrete (RC) beams (i.e., two

protected with I-Lam panels and one without I-Lam protection) at Transportation Research Center, Inc. (TRC), and the beams are impacted by a 12x12x12" wooden projectile traveling at 45 mile/hr. Based on the test observations, the RC beam without I-Lam protection is severely damaged, and large cracks with exposure of steel reinforcement are developed after impact. While for the beams with I-Lam protection, only minor fine cracks developed after impact, and the I-Lam panels are partially damaged (crushed) to absorb the kinetic energy. The experimental evidence indicates that the I-Lam panels can be used to effectively protect the substrate structures and mitigate the impact damage by core crushing. The full-scale lab impact tests of reinforced concrete beams with and without I-Lam protection demonstrate the effectiveness of the I-Lam panels in impact protection and mitigation and validate the proposed I-Lam concept at the lab-scale level.

- An overheight impact detection and evaluation system is developed for the concrete bridges based on smart piezoelectric material. Piezoceramic (PZT) transducers are used for impact detection and health monitoring purpose. An electric circuit is designed for trigging the digital camera to take photos of truck which hits the concrete bridge. The output of the impact PZT sensor is proportional to the impact energy when collision is simulated in impact tests. Impact level can be estimated from the impact sensor signal. The PZT-based health monitoring method can detect the growth of the cracks inside the concrete structure when the structure is gradually damaged in the impact tests. The proposed overheight collision detection and evaluation system has the advantages of simultaneously sending a triggering signal to capture an image of the offensive vehicle and estimating the impact level on the I-Lam. The proposed system has the potential to be applied to the highway bridges.

10. CONCLUSIONS AND RECOMMENDATIONS

In this project, a new collision protection/scarifying I-Lam system for concrete bridge girders using composite sandwich with crushable core is developed. It is capable of later being integrated with smart sensors and actuators for remote sensing, triggering and monitoring. A combined analytical, experimental and numerical approach is used to develop the I-Lam system for collision protection of highway bridge girders from potential overheight truck impact. Simplified design analysis models are developed, which can be easily adopted by the practicing engineers to conduct preliminary design analysis of I-Lam protection system. General design limit criteria and design procedures are proposed, based on the concept of impact mechanics and energy conservation. A final design of bi-layer honeycomb I-Lam sandwich (see Figure 12) is given, and the material (see Figure 13) is fabricated by Plascore, Inc. The numerical simulations of the plain and reinforced concrete beams with and without I-Lam protection demonstrate that the transferred contact force is significantly reduced for the beams with the I-Lam protection, and less damage is induced for the protected concrete beams, thus meeting the intended objective of protecting the underneath concrete structures. The experimental evaluation of the I-Lam-concrete interface bond indicates that a good adhesive bond exists between the high density core and

concrete, and it will provide a better attachment of I-Lam panels to concrete structures when the bonding is needed in the installation (though only the bolting is used in the field installation in this study). Both the crushing and indentation tests are conducted using the MTS and ARAMIS systems, and the core crushing strength, densification and indentation contact law of various loading stages are experimentally obtained, which are later used to develop a semi-empirical impact design. Further refined analysis is conducted using the experimentally based crushing and indentation properties, and the impact responses of I-Lam and absorbed energy are more realistically and accurately predicted under different stages of loading (e.g., elastic and elastic-plastic). Full-scale impact tests of reinforced concrete beams with and without I-Lam protection are performed, and the validity of the I-Lam panel in effective protection and impact-mitigation is manifest. An impact detection and triggering system using smart piezoelectric material is developed, and its reliability and sensitivity are validated in the lab with different magnitude and velocity of impact.

Contributions: In summary, the developed smart bi-layer honeycomb I-Lam sandwich is capable of reducing the transferred contact force dramatically, absorbing/mitigating impact energy, protecting the underneath concrete structures by system scarifying and core crushing, and monitoring the impact incident with smart piezoelectric sensors, and it is applicable to protecting other structures (e.g., steel girders, columns) from accidental vehicle impact in the highways. The simplified analytical models and corresponding design criteria and guidelines developed are contributed to advancing engineering practice and design of impact protection/mitigation systems. The conducted experimental study of I-Lam under crushing and indentation is important for better understanding the contact behavior during the impact process and helps develop semi-empirical models. The full-scale lab impact tests of reinforced concrete beams with and without I-Lam protection demonstrate the effectiveness of the I-Lam panels in impact protection and mitigation and validate the proposed I-Lam concept at the lab-scale level.

Recommendations: Based on the observations from this study, the following recommendations are suggested for further study:

- Though the full-scale lab impact/collision tests validate the proposed concept at the lab-scale load, the real field impact is needed to validate the performance of the I-Lam protection system. There is also a need to evaluate the effectiveness and practicability of the remote monitoring in the field for the potential impact incidents.

- As demonstrated in this report, the proposed I-Lam technology has potential benefits to collision protection and impact mitigation, and it should be considered for further investigation for protection of other highway structures.

- The application of I-Lam structures to concrete girders is studied. The modification of the I-Lam panels, in particular in term of installation and attachment details, to other types of structures (e.g., steel girder and prestressed I-girders, etc.) should be explored.

11. POTENTIAL IMPLEMENTATION

The simplified design criteria (i.e., contact force limit, contact displacement limit, and energy absorption limit) and methodology developed for I-Lam sandwich structures can aid and guide practicing engineers to design similar impact mitigation and protection systems and to tackle the collision-related problems encountered in the field.

The potential of the over-height collision protection (scarifying) system for future implementation in protecting concrete bridge girders from impact is promising. This developed technology could also be adopted for bridge columns and signing structures as well as steel bridge girders for protection from possible impact loads.

The outcomes of this study provide guidance for developing acceptance test procedures for similar applications, observations and recommendations useful for updating current bridge repair procedures. Ultimately, potential pilot projects should be identified and implemented to demonstrate the effectiveness and usefulness of the proposed protection system under actual field conditions.

12. BIBLIOGRAPHY

Abendroth, R. and Fanous, F., 2003, "Lateral Impact to PC Girders in Bridges with Intermediate Diaphragms", Proceedings of the 2003 Mid-continent Transportation Research Symposium, Ames, Iowa, August, 2003.

Ayres J.W., Lalande F., Chaudhry Z. & Rogers C., 1998. Qualitative impedance-based health monitoring of civil infrastructures, Smart Materials and Structures, 7(5): 599-605

Caprino, G. and Teti, R., 1994, "Impact and Post Impact Behavior of Foam Core Sandwich Structures," *Composite Structures*, 29: 47-55.

Davies, G.A.O., Hitchings, D. and Wang, J., 1995, "Prediction of Thresholds of Glass Fiber Reinforced Laminates," *Composite Structures*, 31: 185-193.

Dobyns, A.L. and Porter, T.R., 1981, "A Study of The Structural Integrity of Graphite Composite Structure Subjected to A Low Velocity Impact," *Polymer Engineering Science*, 21: 493-498.

Egusa, S. & Iwasawa N., 1998. Piezoelectric paints as one approach to smart structural materials with health-monitoring capabilities, *Smart Materials and Structures*, 7(4): 438-45

Galea C.S., Chiu W.K. & Paul J.J., 1993. Use of piezoelectric films in detecting and monitoring damage in composites, *Journal of Intelligent Material Systems and Structures,* 4: 683-89

Gibson, L. J. and Ashby, M. F., 1988, Cellular Solids: Structure & Properties, Pergamon Press

Goldsmith, W. and Sackman, J. L., 1992, "An Experimental Study of Energy Absorption in Impact on Sandwich Plates", *International Journal of Impact Engineering*, 12, 241-262.

Johnson, K.L., Contact Mechanics. Cambridge University Press, Cambridge, England, 1985.

Lee C.K. , Lin C. T. , Hsiao C. C. & Liaw W. C. , 1998. New tools for structural testing: piezoelectric impact hammers and acceleration rate sensors. *Journal of Guidance, Control and Dynamics*, 21(5):692-7

Lee, L.J., Kuang, K.Y., and Fann, Y.J., 1993, "Dynamic Response of Composite Sandwich Plate Impacted by A Rigid Ball", *Journal of Composite Materials*, 27(13): 1239~1256.

Lim, T. S, Lee, C. S and Lee, D. G, 2004, "Failure Modes of Foam Core Sandwich Beams under Static and Impact Loads", *Journal of Composite Materials*, 38(18):1639-1662.

Lorenz R.D., Bannister M., Daniel P. M., Krysinski Z., Leese M. R., Miller R. J. , Newton G. , Rabbetts P. , Willett D. M. & Zarnecki, 1994. An impact penetrometer for a landing spacecraft, *Measurement Science & Technology*, 5(9): 1033-41

Matemilola, S.A., and Strong, W.J., 1995, "Impact Induced Dynamic Deformation and Stresses in CFRP Composite Laminates," *Composites Engineering*, 5(2): 211-222.

Olsson, R., 2002, "Engineering Method for Prediction of Impact Response and Damage in Sandwich Panels", *Journal of Sandwich Structures and Materials*, 4: 3-29.

Qiao, P., Yang, M. J. and Mosallam, A. S., 2004, "Impact Analysis of I-Lam Sandwich System for Over-Height Collision Protection of Highway Bridges", Engineering Structures, 26(7): 1003 – 1012.

Qiao, P. and Xu, Y., 2004. "Evaluation of Fracture Energy of Composite-Concrete Bonded Interfaces Using Three-Point Bend Tests," *Journal of Composites for Construction*, ASCE, 8(4): 352-359.

Quek S. T., Wang Q. , Zhang L. & Ong K. H. , 2001. Practical issues in the detection of damage in beams using wavelets, *Smart Materials and Structures*, 10(5):1009-17

Reid, S.R. and Zhou, G., 2000, Impact Behavior of Fiber Reinforced Composite Materials and Structures. CRC press, Boca Raton, FL.

Saafi M. & Sayyah T., 2001. Health monitoring of concrete structures strengthened with advanced composite materials using piezoelectric transducers, *Composites: Part B*, 32: 333-42

Shipsha, A. Hallstrom, S. and Zenkert, D., 2003, "Failure Mechanisms and Modeling of Impact Damage in Sandwich Beams – A 2D Approach. Part I. Experimental Investigation". *Journal of Sandwich Structure and Material*, 5(1):7-32.

Slenk, J., Mosallam, A.S., and Kreiner, J., 2003, "Experimental Assessment of Residual Tensile Strength of Graphite Epoxy Woven Laminates after Impact," in preparation.

Sneddon, I.N., 1948, "Boussinesqs problem for a rigid cone", *Proceedings of The Cambridge Philosophical Society*, 44 (4): 492-507

Soh C. H., Tseng K.K., Bhalla S. and Gupta A., 2000. Performance of smart piezoceramic patches in health monitoring of a RC bridge, *Smart materials and Structures*, 9(4): 533-42

Song, G., H. Gu, Y. L. Mo, T. T.C. Hsu, H. Dhonde & R.H. Zhu, 2004. Health monitoring of a reinforced concrete bridge bent-cap using piezoceramic materials, *Proceedings of the Third European Conference on Structural Control*, 12-15 July, Vienna, Austria

Song, G., H. Gu, Y. L. Mo, T. T.C. Hsu, H. Dhonde & R.H. Zhu, 2005. Health monitoring of a concrete structure using piezoceramic material. *SPIE international Symposia-Smart Structures & Materials /NDE,* San Diego, California, USA

Tan, T.M. and Sun, C.T., 1985, "Use of Statical Indentation Laws in the Impact Analysis of Laminated Composite Plates," *J. Appl. Mech*., 52: 6-12.

Tong J. H., Wu T.T. & Lee C.K. , 2002. Fabrication of a piezoelectric impact hammer and its application to the in-situ nondestructive evaluation of concrete, *the Japan Society of Applied Physics,* Part 1, 41(11A): 6595-600

Tsai, C.Z., Wu E., and Luo, B.H., 1998, "Forward and Inverse Analysis for Impact on Sandwich Panels," *AIAA J.*, 36(11): 2130~2136.

Tseng K K-H & Naidu A S K, 2002. Non-parametric damage detection and characterization using smart piezoceramic material, *Smart Materials and Structures*, 11(3): 317-29

Tseng K. T. & Wang L. 2004. Smart piezoelectric transducers for in situ health monitoring of concrete, *Smart Materials and Structures*, 13(5): 1017-24

Turk, M.H. and Hoo Fatt, M.S., 1999, "Localized Damage Response of Composite Sandwich Plates," *Composites Part B: Engineering J.*, 30: 157-165.

Wang S. C., Wu F. & Chang F-k, 2001. Structural health monitoring from fiber-reinforced composites to steel-reinforced concrete, *Smart Materials and Structures*, 10(3): 548-52

Willis J.R., 1966. "Hertz contact of anisotropic bodies". *Journal of The Mechanics and Physics of Solids*, 14, 163-176

Yigit, A.S. and Christoufou, A. P., 1995. "On the impact between a rigid sphere and a thin composite laminate supported by a rigid substrate", *Composite Structures*, 30:168-177.

Yang, M. J., 2006. "Impact Mechanics of Elastic and Elastic-plastic Sandwich Structures", Ph.D Thesis, The University of Akron.

Appendix A: Original Installation Design of I-Lam

The I-Lam panels are eventually installed in a concrete slab bridge (DEL-23-12.99) in Delaware, OH. The actual implementation and installation details are given in Section 9. In this appendix, the original installation design of I-Lam is given in detail, though the actual installation is slightly different, due to the site condition and limitation of resource (see Section 9). The adhesive bonding of I-Lam to the bridge and attachment of piezoelectric sensors/monitoring unit given in the original installation design are not included in the actual field implement. Step-by-step construction procedures for I-Lam sandwich panels (the I-Lam is assumed to be installed on a potential concrete girder with flat surface, see Figures A1 and A2) are given as:

1. Sandwich panels (I-Lam) of 12”x12”x8” will be first adhesively bonded to the add-on aluminum backing plate and then back-bolted using four rivets at the four corners (Figure A3). The add-on plate has an L-shape which provides anchoring mechanism for the I-Lam to concrete girder (This step will be prepared and fabricated in the lab).

2. In the field, the I-Lam system with L-shape backing plate will be then bonded to the concrete girder using epoxy. Two concrete screws of 2” long will be drilled through the top of add-on aluminum backing plate and into the concrete. An additional screw will be drilled through the bottom of L-shape aluminum plate and further secure the I-Lam in position. Besides anchoring I-Lam to the concrete, the screw mechanism is also used to apply a pressure to epoxy, thus improving the bonding condition.

3. A safety steel cable will be connected to the top face sheet of I-Lam to provide the additional safety measure. (two cables per I-Lam are used, Figure A3)

4. Total of ten I-Lams will be installed over the coming traffic lane only. The spacing between I-Lams is about 1”. (thus, the total install length is about 10 ft and 9 in. over the traffic lane)

5. The I-lams will be installed with piezoelectric sensors to monitor the incident of impact. An impact trigger is designed, and it will be connected to ODOT camera for on-line/internet monitoring.

Figure A1 Schematic of I-Lam installed on a potential concrete bridge

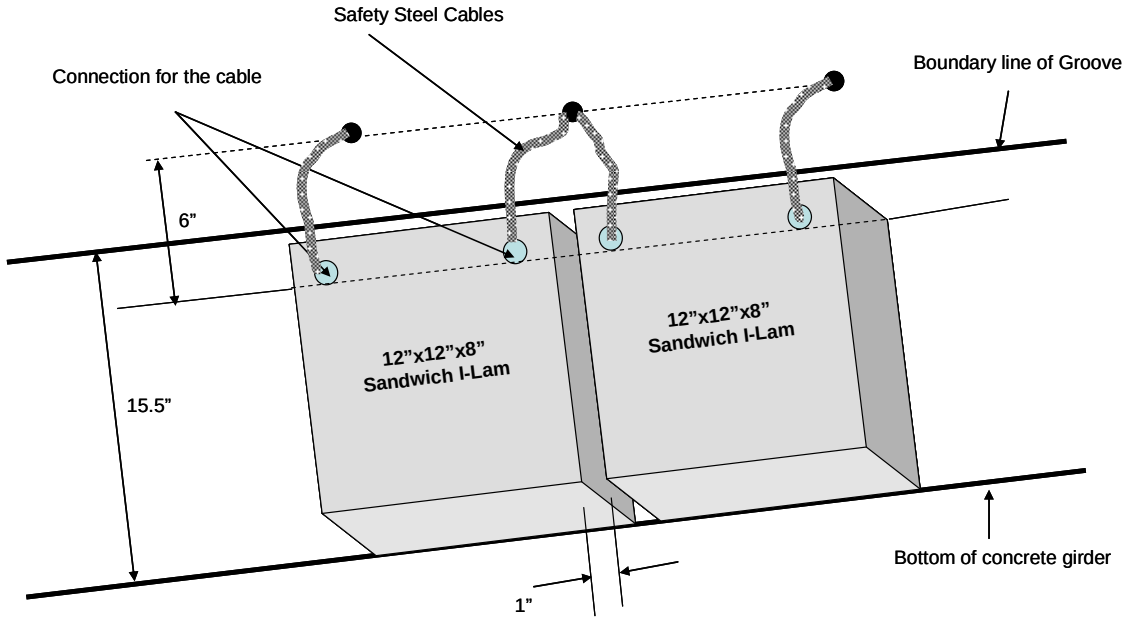

Figure A2 Installation of I-Lam

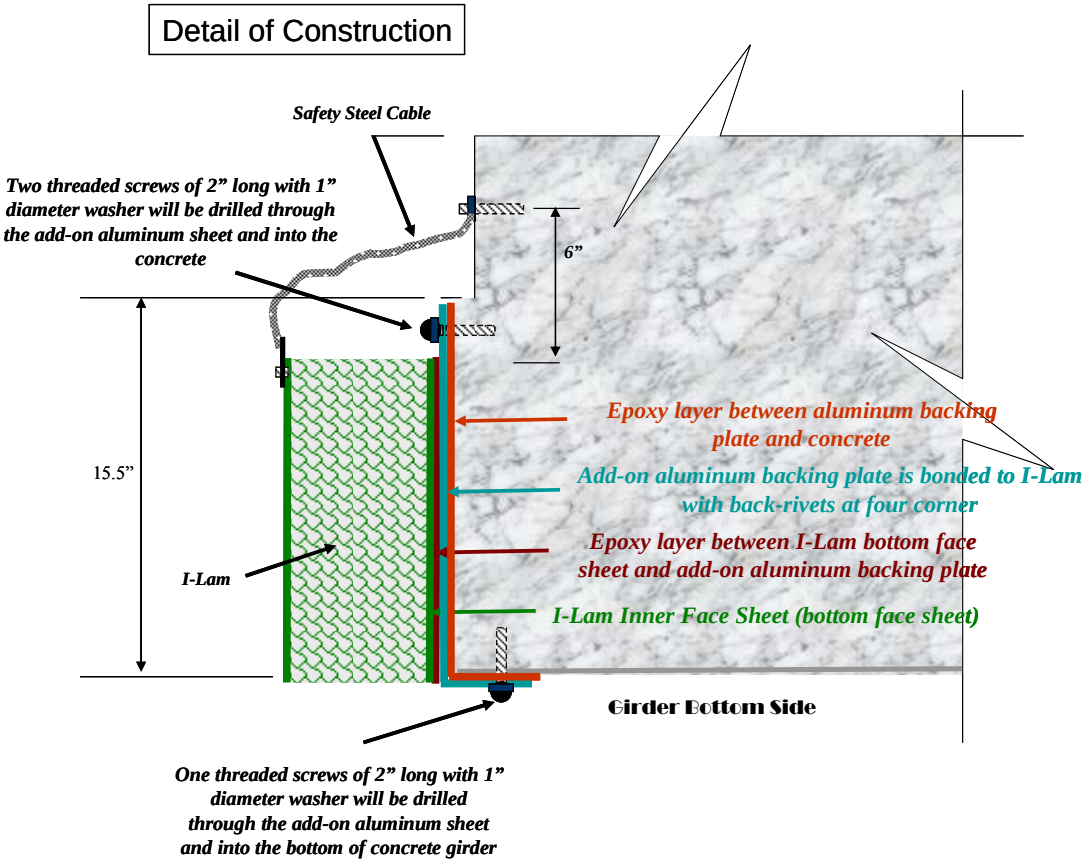

Figure A3 Details of the original I-Lam installation

Appendix B: Experimental Elastic Indentation Curves

Different loading curves for elastic contact regions of the honeycomb I-Lam sandwiches are experimentally obtained from the MST system, and they are plotted and fitted as shown in Figures B1 to B10.

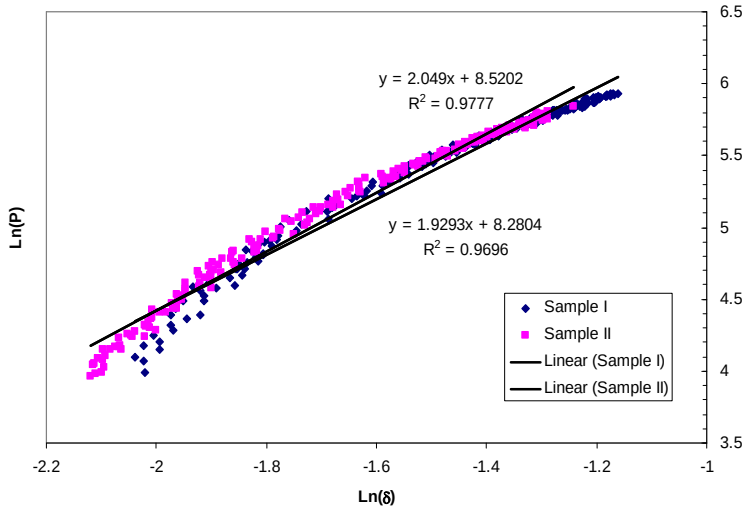

Figure B1 Fitting of elastic load indentation curves of the honeycomb sandwich with a relative density of 83.64 kg/m^3 using the 1.5'' sphere indenter

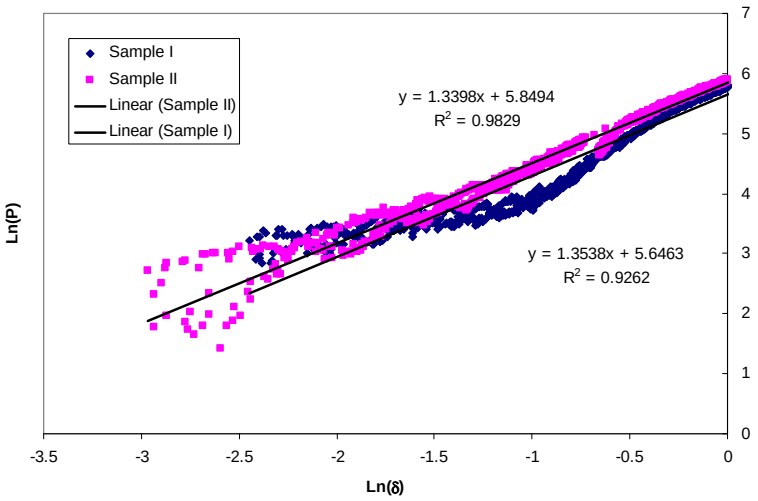

Figure B2 Fitting of elastic load indentation curves of the honeycomb sandwich with a relative density of 54.69 kg/m^3 using the 1.5'' sphere indenter

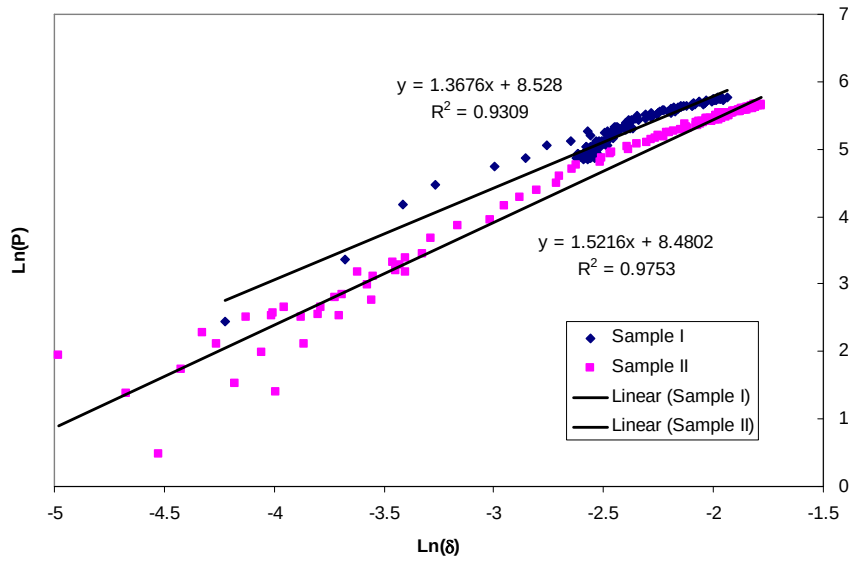

Figure B3 Fitting of elastic load indentation curves of the honeycomb sandwich with a relative density of 83.64 kg/m^3 using the 1'' sphere indenter

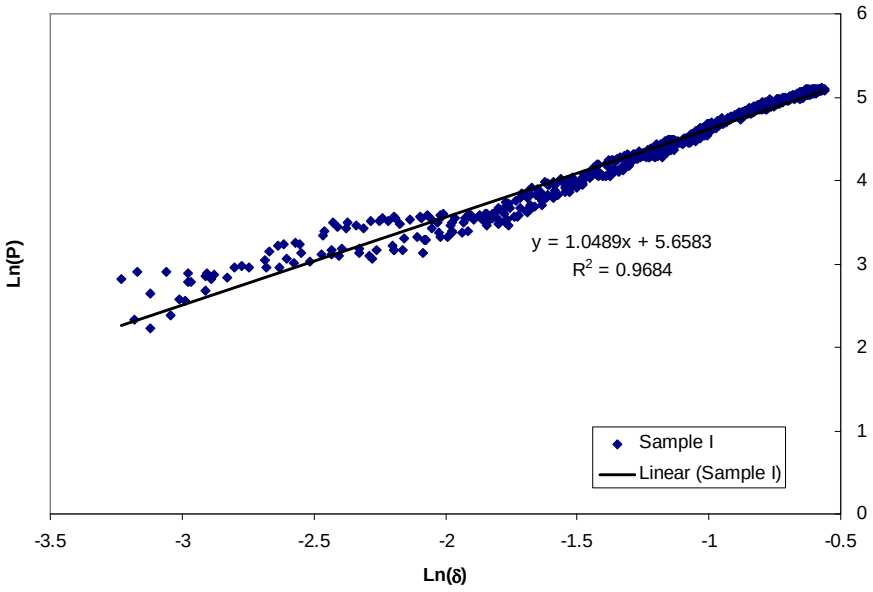

Figure B4 Fitting of elastic load indentation curves of the honeycomb sandwich with a relative density of 54.69 kg/m^3 using the 1 in sphere indenter

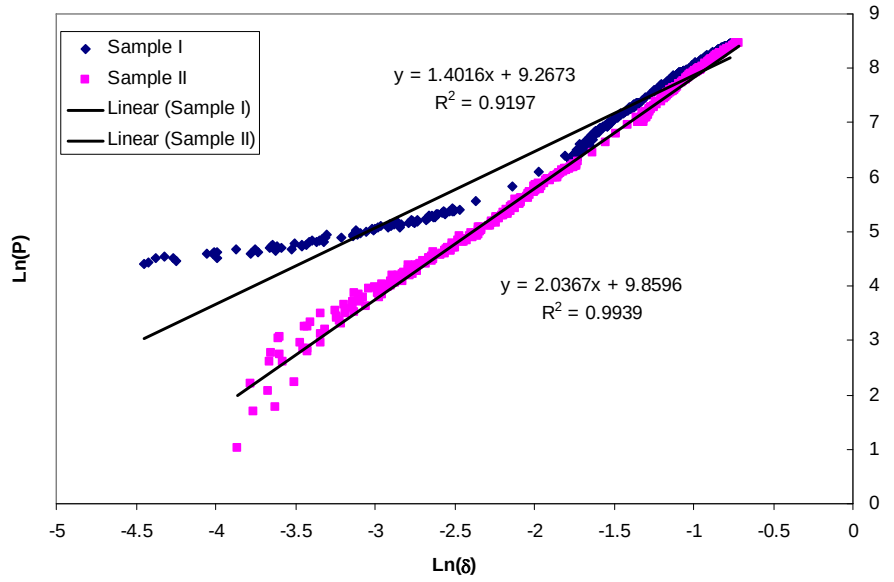

Figure B5 Fitting of elastic load indentation curves of the honeycomb sandwich with two layers and indented on the higher density side using the 1.5'' flat square indenter

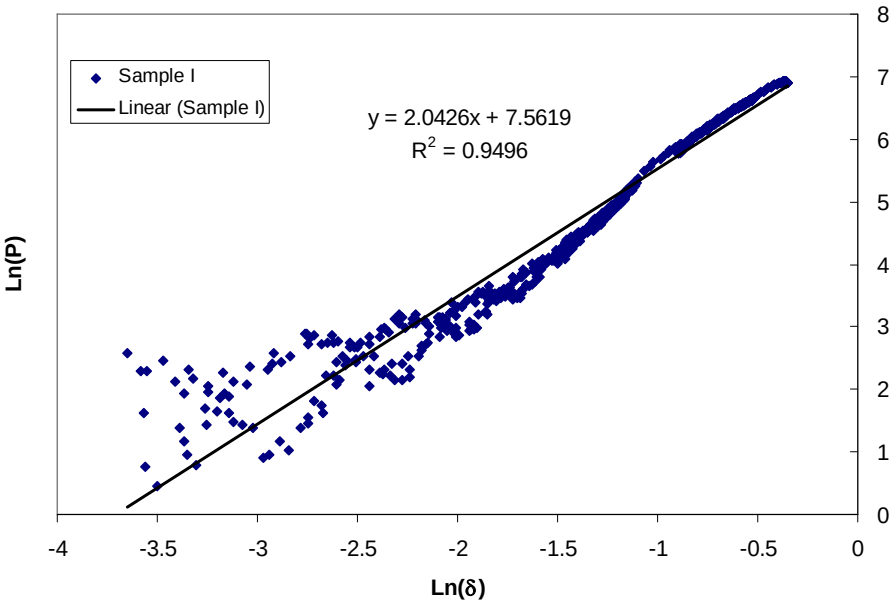

Figure B6 Fitting of elastic load indentation curves of the honeycomb sandwich with two layers and indented on the lower density side using the 1.5'' flat square indenter

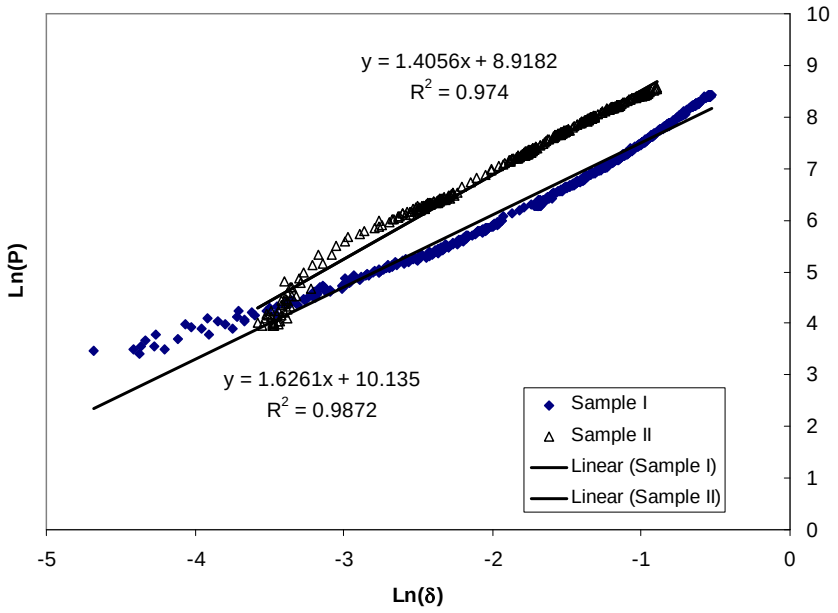

Figure B7 Fitting of elastic load indentation curves of the honeycomb sandwich with a relative density of 83.64 kg/m^3 using the 1.5'' flat square indenter

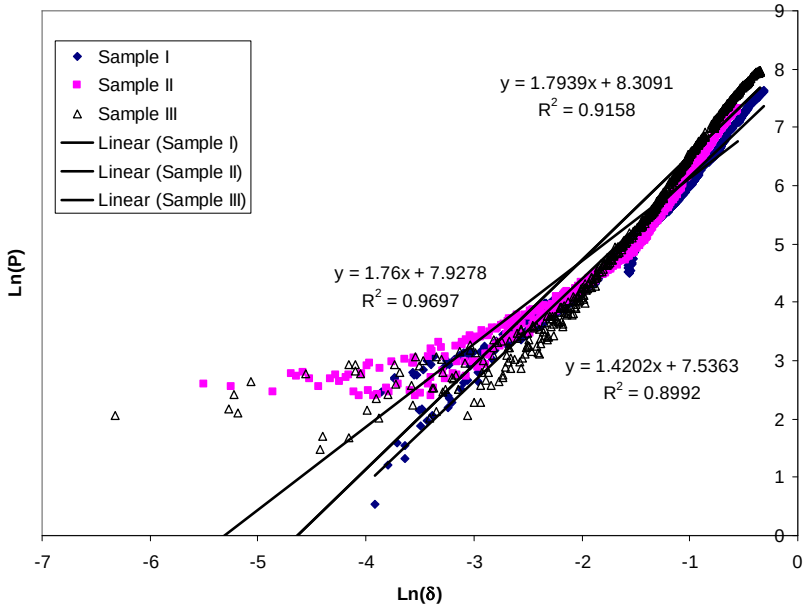

Figure B8 Fitting of elastic load indentation curves of the honeycomb sandwich with a relative density of 54.69 kg/m^3 using the 1.5'' flat square indenter

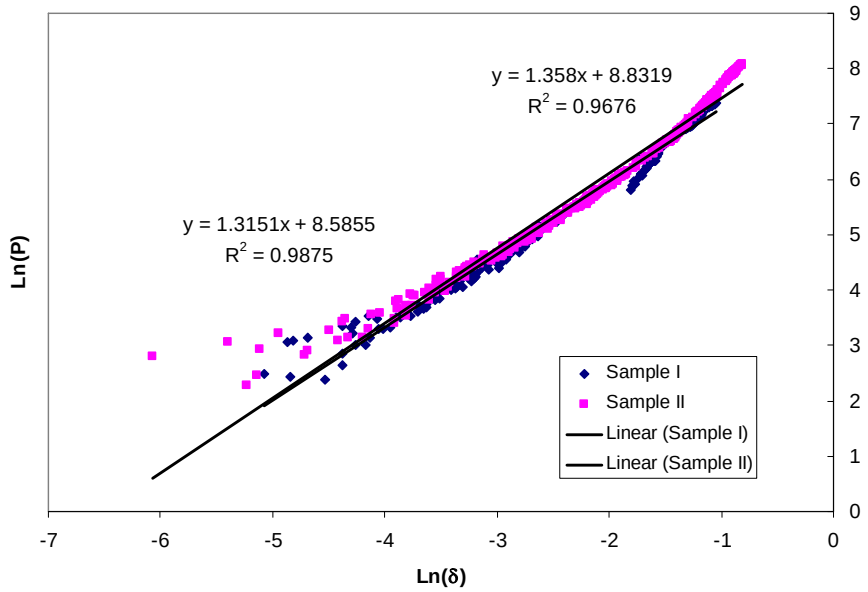

Figure B9 Fitting of elastic load indentation curves of the honeycomb sandwich with a relative density of 83.64 kg/m^3 using the 1.0'' flat square indenter

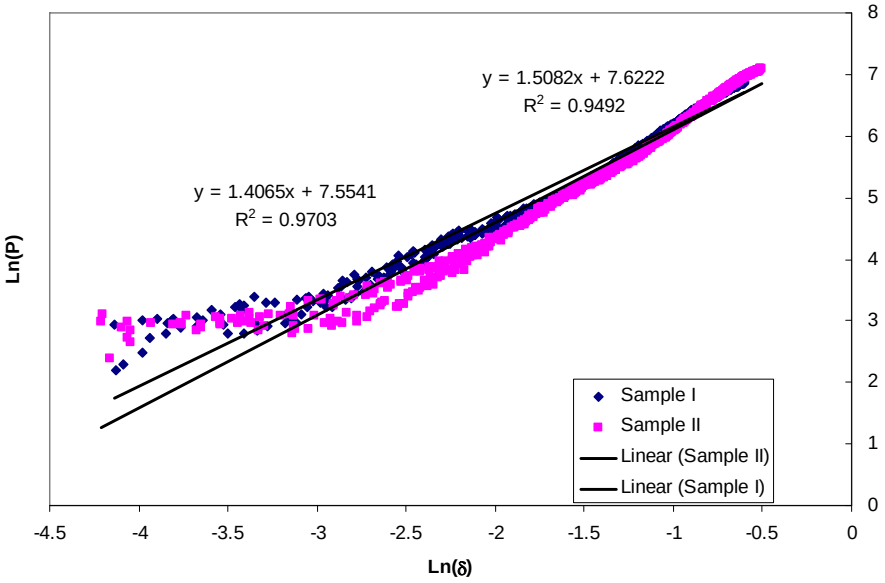

Figure B10 Fitting of elastic load indentation curves of the honeycomb sandwich with a relative density of 54.69 kg/m^3 using the 1.0'' flat square indenter

Appendix C: Experimental Elastic-plastic Indentation Curves

Different unloading and reloading curves for elastic-plastic contact regions of the honeycomb I-Lam sandwiches are experimentally obtained as well from the MST system, and they are plotted and fitted as shown in Figures C1 to C18.

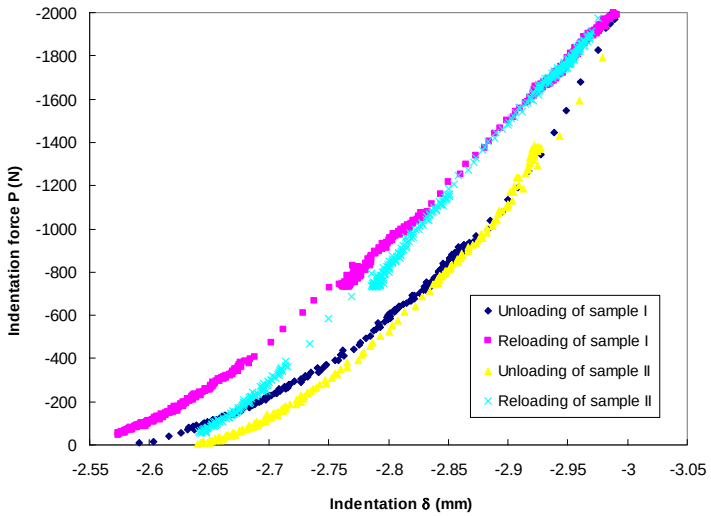

Figure C1 Elastic-plastic loading and unloading indentation curves of the honeycomb sandwich with a relative density of 83.64 kg/m^3 using the 1.5'' sphere indenter

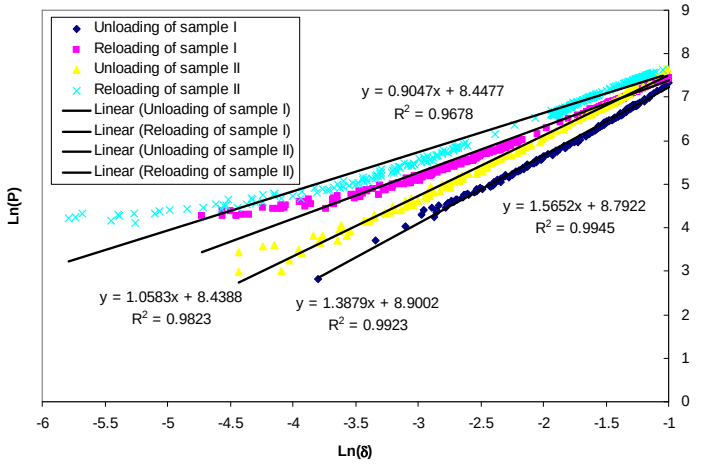

Figure C2 Fitting of elastic-plastic loading and unloading indentation curves of the honeycomb sandwich with a relative density of 83.64 kg/m^3 using the 1.5'' sphere indenter

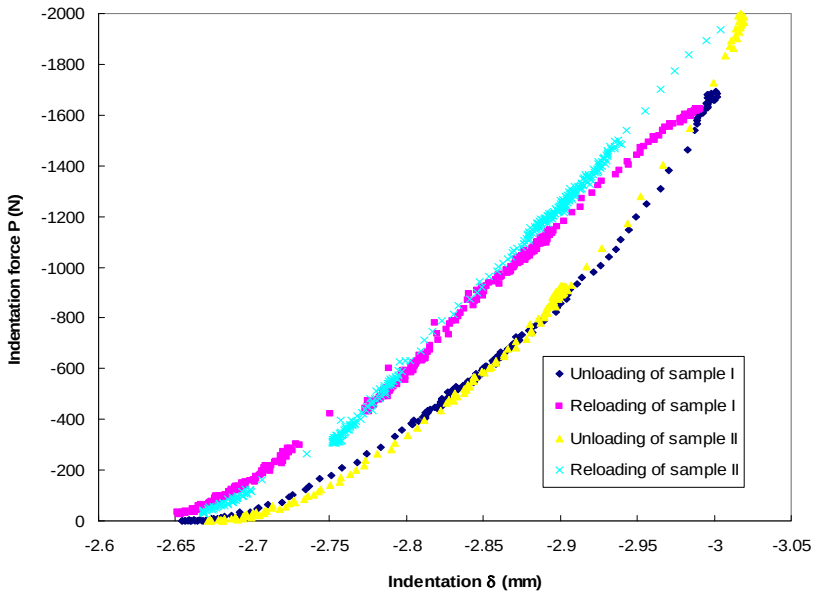

Figure C3 Elastic-plastic loading and unloading indentation curves of the honeycomb sandwich with a relative density of 83.64 kg/m^3 using the 1.0'' sphere indenter

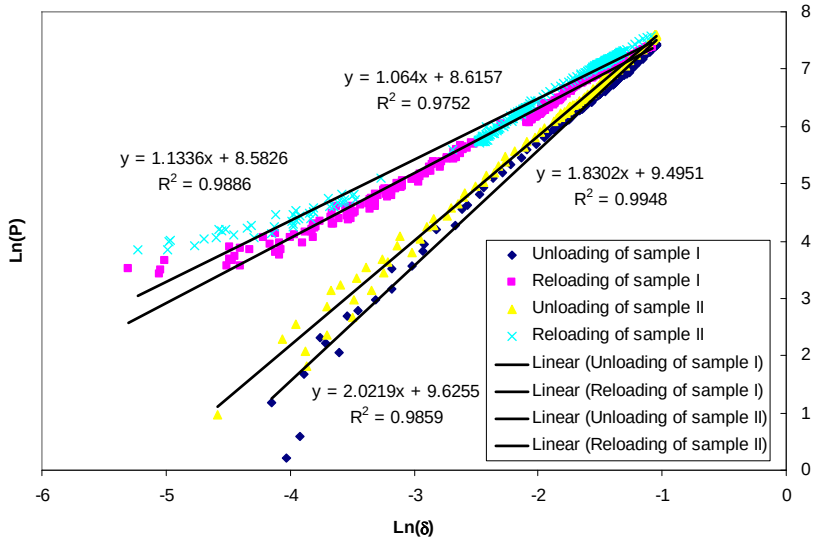

Figure C4 Fitting of elastic-plastic loading and unloading indentation curves of the honeycomb sandwich with a relative density of 83.64 kg/m^3 using the 1.0'' sphere indenter

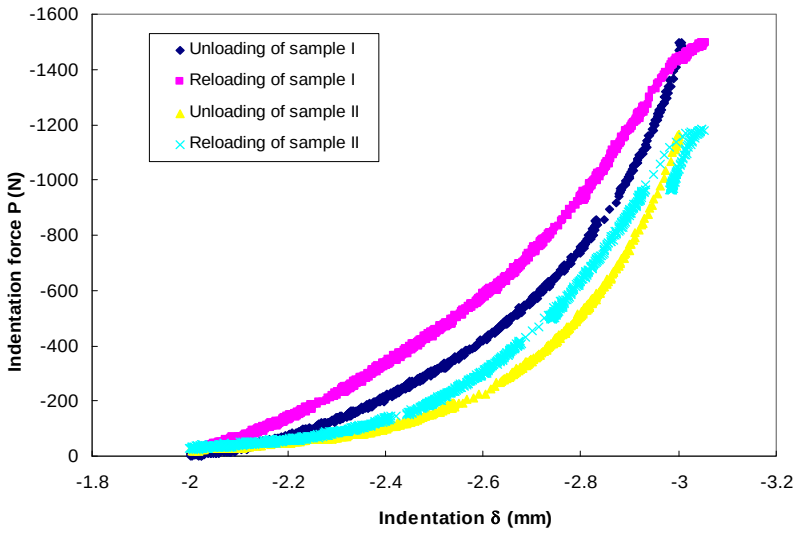

Figure C5 Elastic-plastic loading and unloading indentation curves of the honeycomb sandwich with a relative density of 54.69 kg/m^3 using the 1.5'' sphere indenter

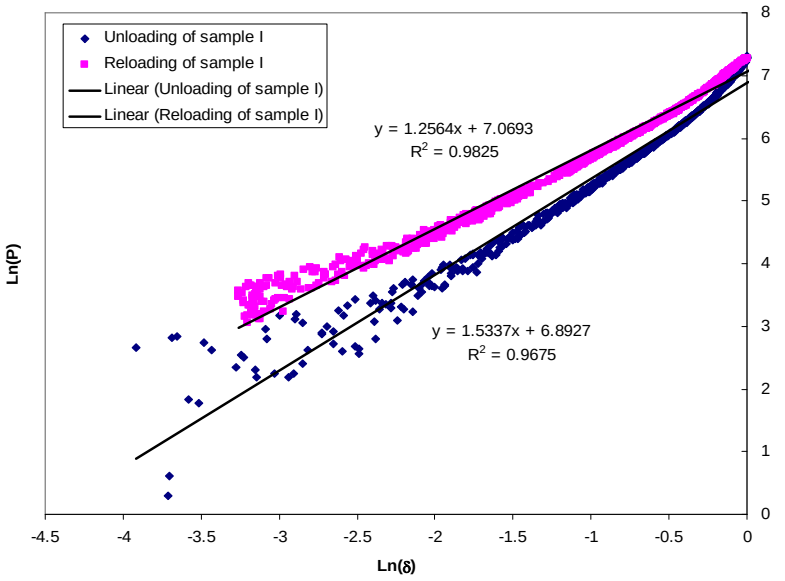

Figure C6 Fitting of elastic-plastic loading and unloading indentation curves of the honeycomb sandwich with a relative density of 54.69 kg/m^3 using the 1.5'' sphere indenter

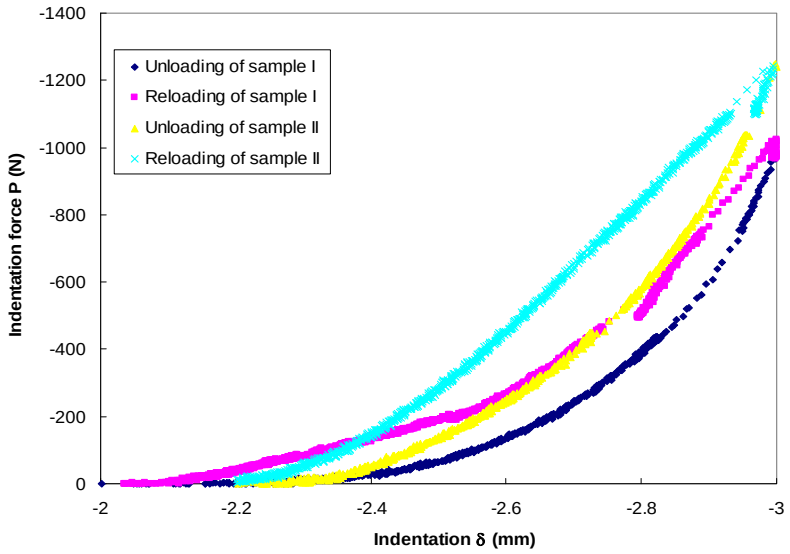

Figure C7 Elastic-plastic loading and unloading indentation curves of the honeycomb sandwich with a relative density of 54.69 kg/m^3 using the 1.0'' sphere indenter

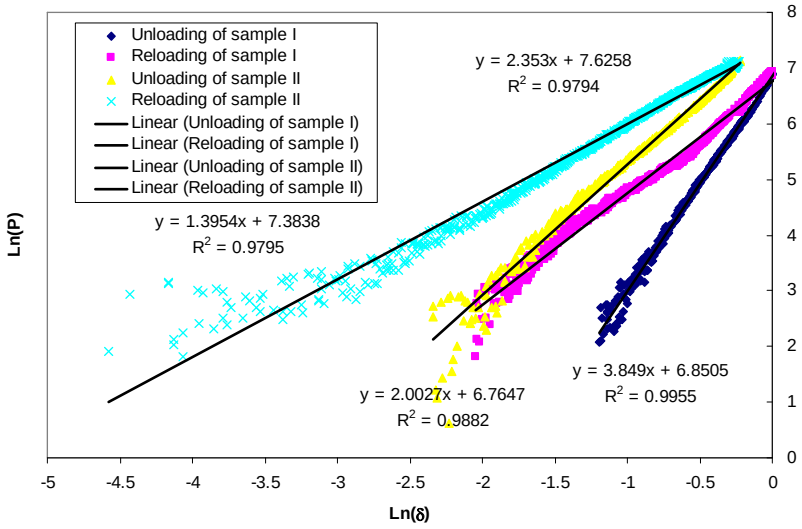

Figure C8 Fitting of elastic-plastic loading and unloading indentation curves of the honeycomb sandwich with a relative density of 54.69 kg/m^3 using the 1.0'' sphere indenter

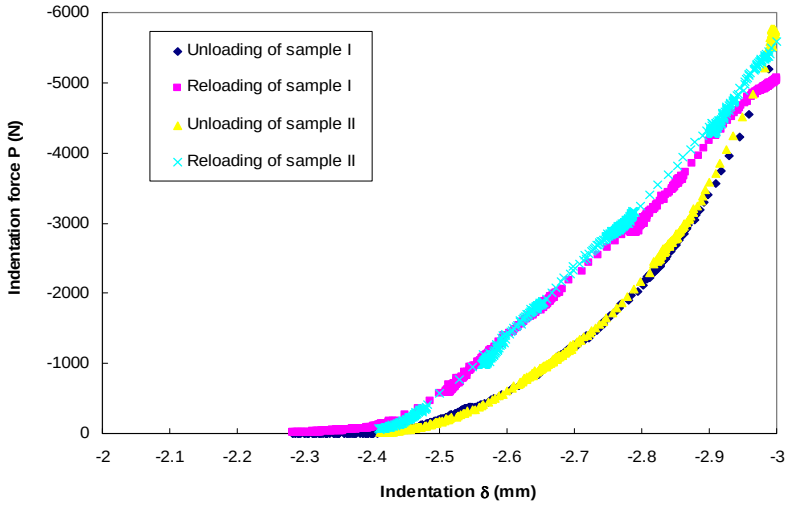

Figure C9 Elastic-plastic loading and unloading indentation curves of the honeycomb sandwich with two layers and indented on the higher density side using the 1.5'' flat square indenter

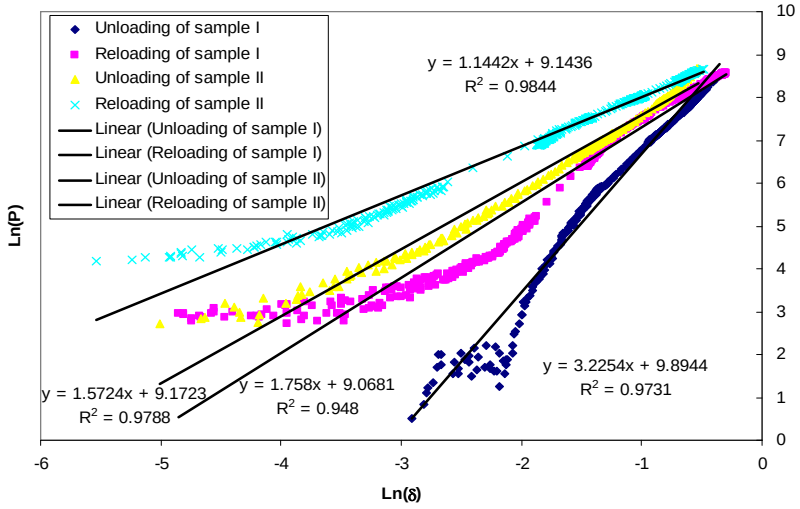

Figure C10 Fitting of elastic-plastic loading and unloading indentation curves of the honeycomb sandwich with two layers and indented on the higher density side using the 1.5'' flat square indenter

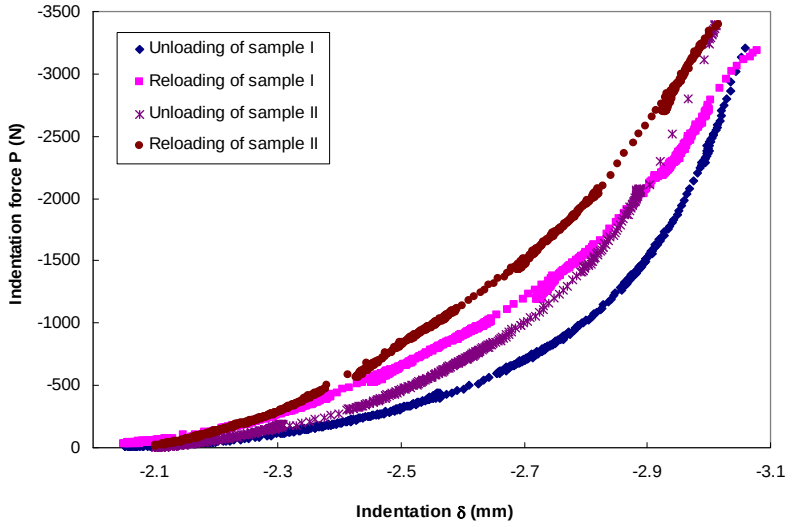

Figure C11 Elastic-plastic loading and unloading indentation curves of the honeycomb sandwich with two layers and indented on the lower density side using the 1.5'' flat square indenter

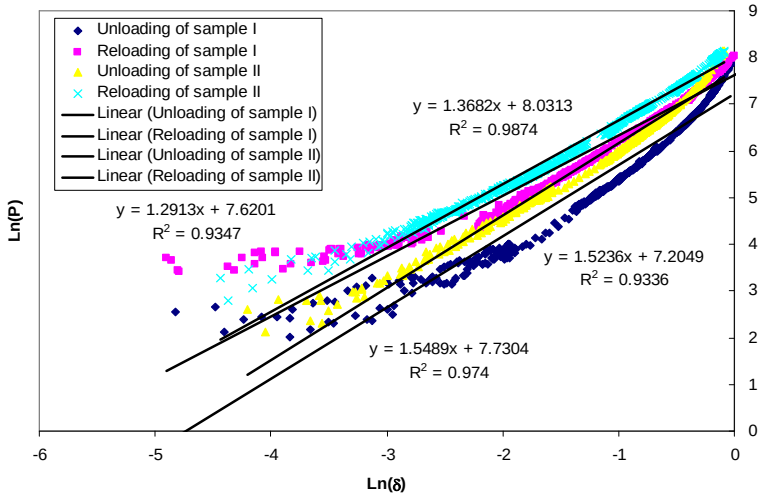

Figure C12 Fitting of elastic-plastic loading and unloading indentation curves of the honeycomb sandwich with two layers and indented on the lower density side using the 1.5'' flat square indenter

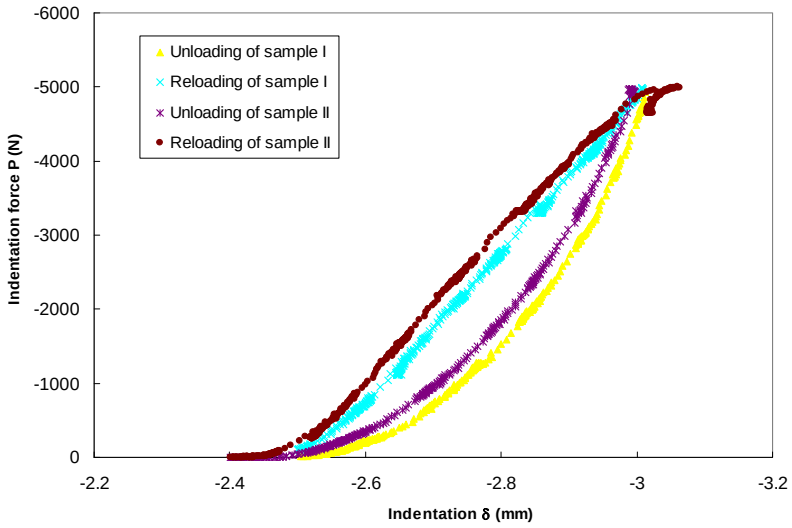

Figure C13 Elastic-plastic loading and unloading indentation curves of the honeycomb sandwich with a relative density of 83.64 kg/m^3 using the 1.5'' flat square indenter

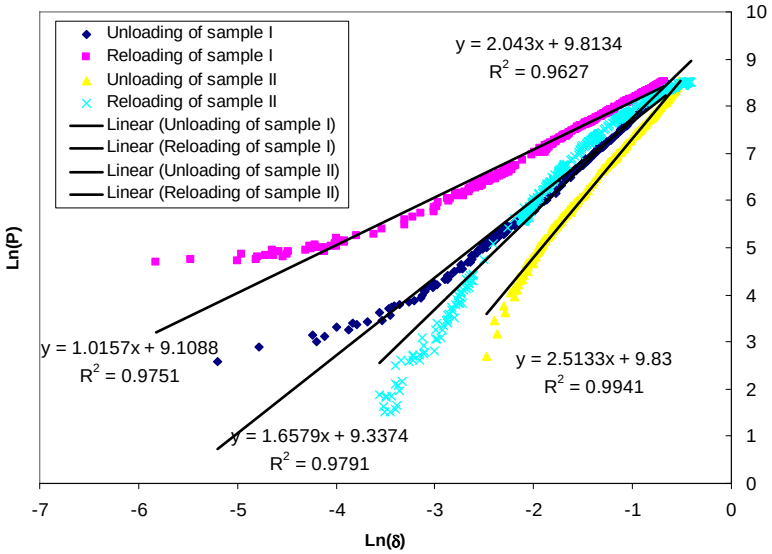

Figure C14 Fitting of elastic-plastic loading and unloading indentation curves of the honeycomb sandwich with a relative density of 83.64 kg/m^3 using the 1.5'' flat square indenter

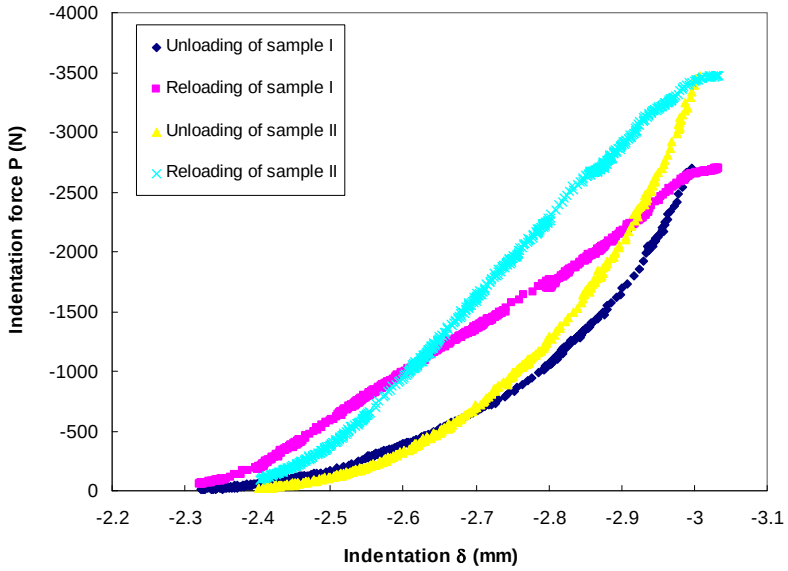

Figure C15 Elastic-plastic loading and unloading indentation curves of the honeycomb sandwich with a relative density of 54.69 kg/m^3 using the 1.5'' flat square indenter

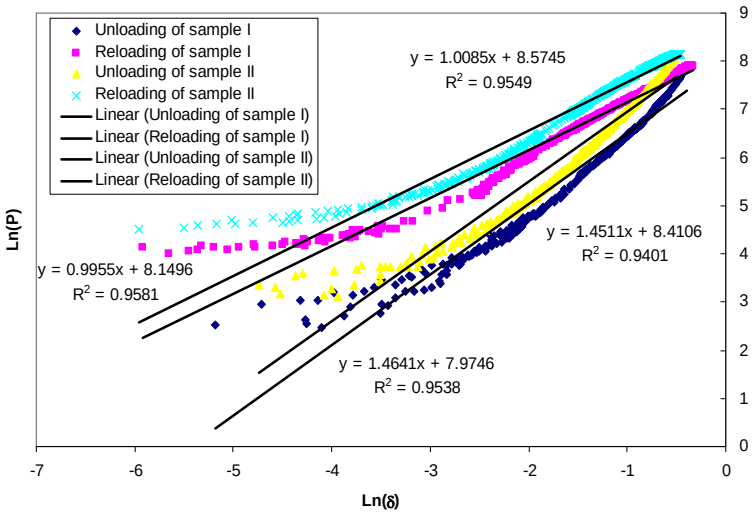

Figure C16 Fitting of elastic-plastic loading and unloading indentation curves of the honeycomb sandwich with a relative density of 54.69 kg/m^3 using the 1.5'' flat square indenter

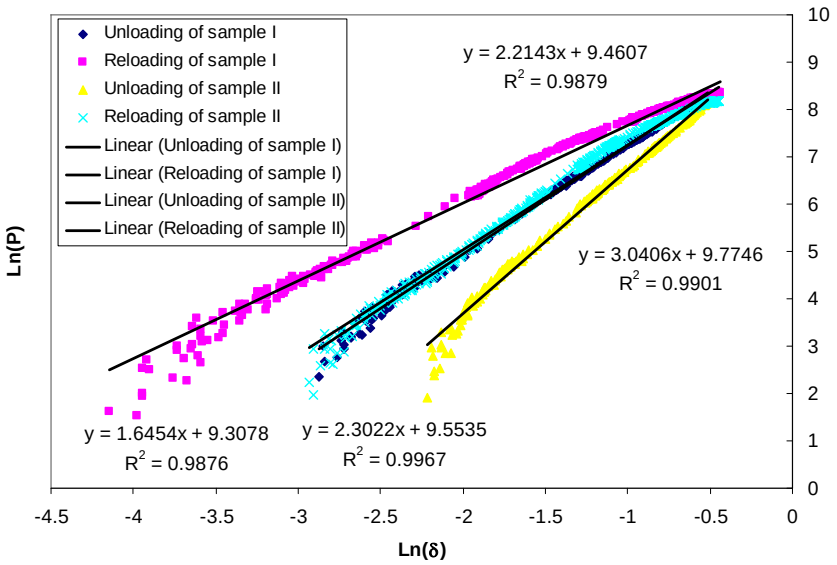

Figure C17 Fitting of elastic-plastic loading and unloading indentation curves of the honeycomb sandwich with a relative density of 83.64 kg/m^3 using the 1.0'' flat square indenter

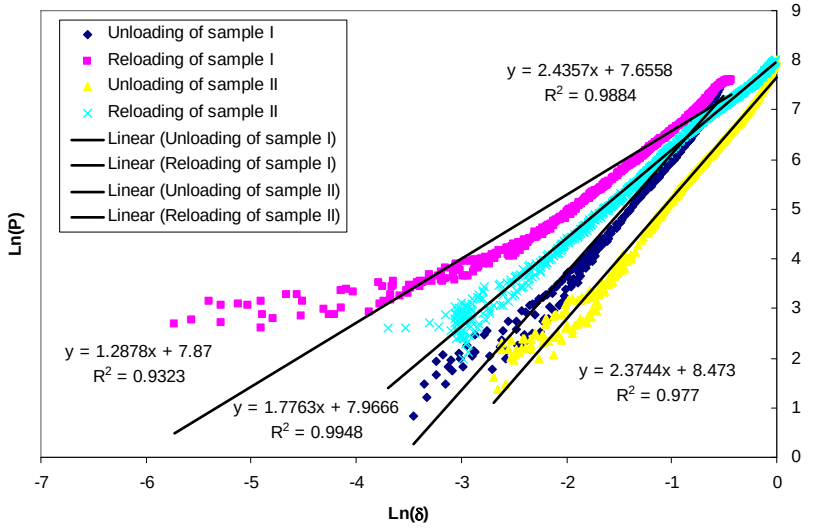

Figure C18 Fitting of elastic-plastic loading and unloading indentation curves of the honeycomb sandwich with a relative density of 54.69 kg/m^{3}using the 1.0'' flat square indenter

Appendix D: PZT Triggering Circuit Box – User Manual

The circuit box (Figure D1) requires a voltage between 9 and 20 Volts. In the back of the triggering box there are 2 banana plugs; red for the positive and black for the negative terminal. Input protection against reverse polarity is present on the circuit board.

Turn on from the power switch located next to the power plugs. When the system is on, the front green LED will turn on and the trigger output will output a fake detection signal.

Connect the PZT signal to the BNC plug and triggering circuit output to network camera alarm input.

To make adjustment to the triggering level, the box needs to be removed. Inside, there is a potentiometer that needs to be changed with a small screwdriver. **Triggering level is set to 2 Volts.** When you change the settings, you can use a multi-meter to check for the voltage between point A and B. See Figure D1 for locating the points.

The PZT ground reference is very sensitive to ground loops. When touching the PZT ground reference with bare hands, the triggering circuit may output a false trigger signal. It is advisable to use sealed BNC connectors.

Figure D2 shows a typical output trigger, and Figure D3 shows the PZT trigger and cable.

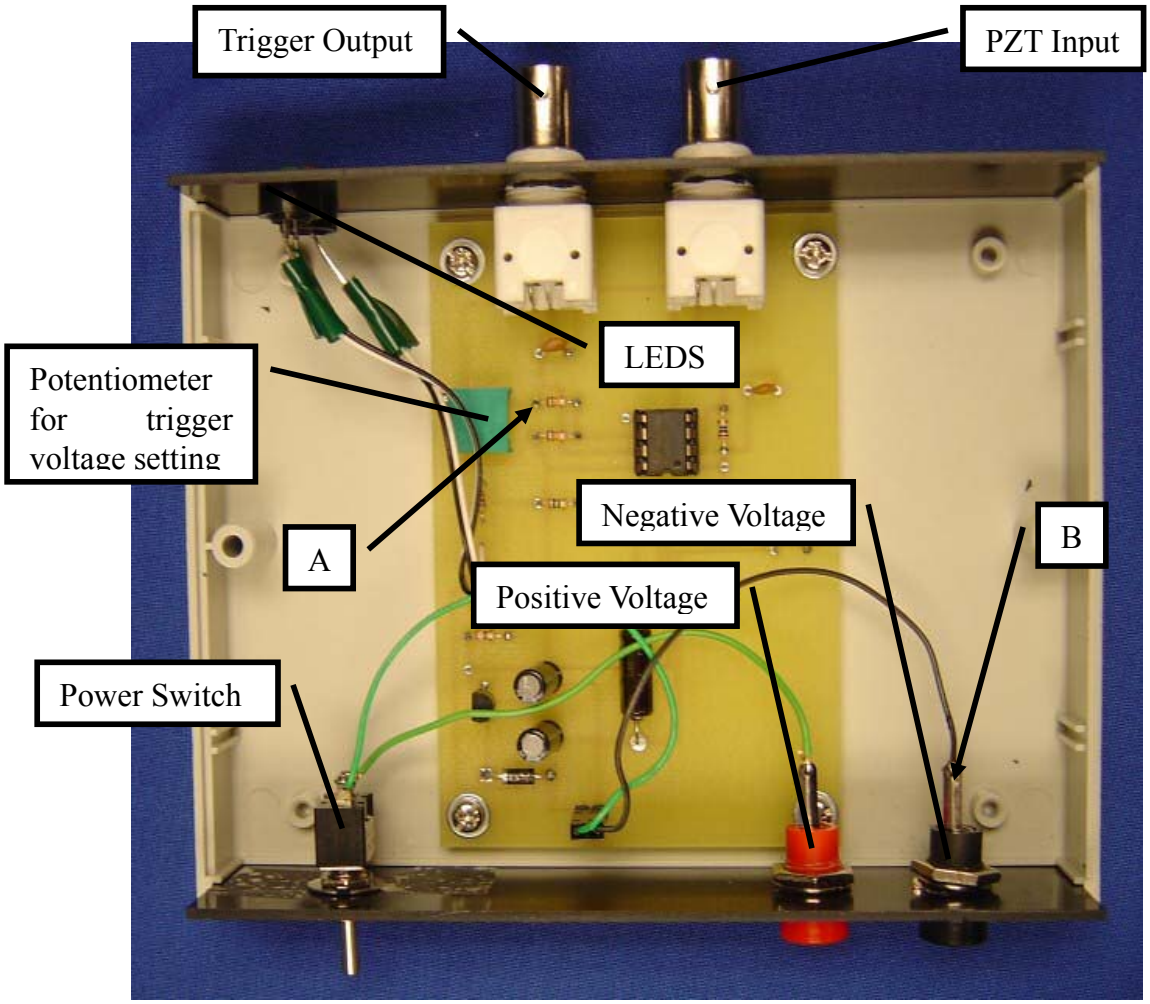

Figure D1 Triggering Circuit

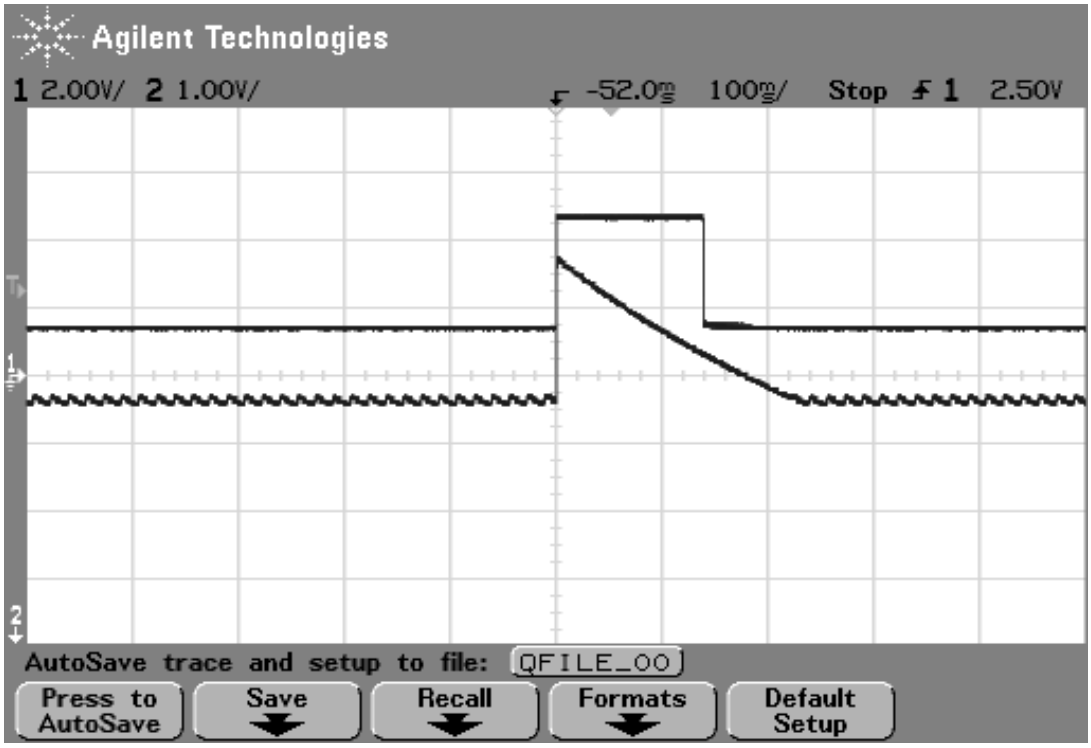

Figure D2 Typical output from triggering circuit (Upper plot) vs. Energy of the input signal (Lower Plot)

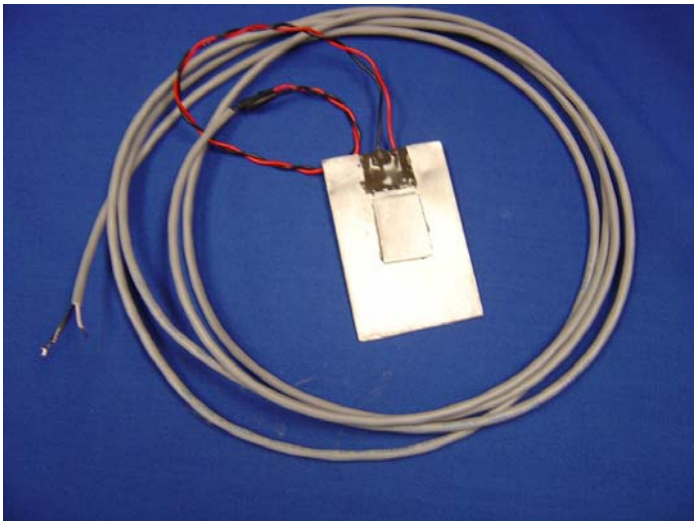

Figure D3 PZT sensor: Signal (White) Ground (Black)